OPTICAL TRANSMISSION SCANNING AND HYBRID ACOUSTO-OPTICAL TECHNIQUES FOR NDE AND SHM OF STRUCTURAL COMPOSITES

By

Oleksii Karpenko

A DISSERTATION

Submitted to
Michigan State University
in partial fulfillment of the requirements
for the degree of

Electrical Engineering – Doctor of Philosophy

2018

ABSTRACT

OPTICAL TRANSMISSION SCANNING AND HYBRID ACOUSTO-OPTICAL TECHNIQUES FOR NDE AND SHM OF STRUCTURAL COMPOSITES

By

Oleksii Karpenko

Fiber reinforced polymer (FRP) composites have been extensively used in aerospace, marine and defense industries due to the many advantages they offer including light-weight, corrosion resistance and excellent thermo-mechanical properties. Increasing fuel-efficiency demands and reducing green-house emissions has also propelled the use of FRP composites in the automotive industry. However, despite excellent mechanical properties of FRPs, their anisotropy, brittle nature and the vulnerability to flaws during fabrication and service has propelled the need of non-destructive evaluation (NDE) and structural health monitoring (SHM) techniques. This dissertation presents three major contributions to the fields of NDE and SHM of structural composites:

- optical transmission scanning (OTS) for rapid, non-contact and quantitative NDE of glass and aramid FRPs;
- optical frequency-domain reflectometry (OFDR) for distributed monitoring of strains in FRPs using single-mode (SM) optical fibers and Rayleigh back-scattering;
- hybrid acousto-optic health monitoring of FRPs using guided waves (GW) and Fabry-Perot interferometric sensors based on chirped fiber Bragg-gratings (CFBG-FPI).

Chapter I presents an OTS system for quantitative NDE of GFRP samples. The technique provides high-resolution, rapid, and non-contact optical transmittance scans. Experimental implementation of the technique and advanced data analysis protocol developed for impact damage evaluation are presented. Obtained experimental results show that other defects and certain microstructural variations in GFRP composites can be easily identified by OTS, because the technique is sensitive to localized changes of optical properties such as radiation absorption and scattering.

The applications of OTS are extended to GFRP plates with improperly mixed resin, inclusions, and delaminations. Finally, the capabilities of the technique to evaluate the distribution of adhesive and detect fatigue damage in adhesively bonded GFRP joints are demonstrated.

Chapter II describes the development of advanced signal processing algorithms for strain sensing in optical fibers using Rayleigh back-scattering and the OFDR technique. Distributed displacement and strain sensing along the fiber length is implemented using the OFDR-1000 system from General Photonics Corporation (Chino, CA). Performance of the system is validated by measuring strains introduced in the optical fiber by the piezoelectric fiber stretcher.

Chapter III lays out the approach for diagnostic imaging of plate-like structures using hybrid acousto-optic technique. Guided waves are excited with surface-bonded piezoelectric wafers and are sensed with pairs of chirped fiber Bragg-gratings that form Fabry-Perot interferometers inside the surface-bonded optical fiber. Initial experimental results obtained on aluminum plates demonstrate that CFBG-FPIs are sensitive to both symmetric and antisymmetric fundamental GW modes. Structural damage is successfully located using Delay-and-Sum (DAS) imaging.

ACKNOWLEDGEMENTS

I would like to express all my gratitude and respect to my research advisors Dr. Lalita Udpa and Dr. Mahmood Haq. I am thankful that Dr. Udpa and Dr. Haq introduced me to a fascinating world of advanced materials and nondestructive evaluation. Their vast knowledge and skill in many areas inspired me to grow as a graduate student and a researcher. Apart from their professional guidance and supervision, Dr. Udpa and Dr. Haq have been my excellent teachers and mentors in all issues that I ever had during the time I worked on this dissertation. I am really glad that fortune has given me the chance to work with these outstanding people. I would like to give special thanks to other members of my committee, Dr. Satish Udpa and Dr. Selin Aviyente, for their fruitful discussions and valuable comments on my dissertation.

I would like to express my gratitude to Dr. Anton Khomenko, Dr. Ermias Koricho and Dr. Gary Cloud, whose expertise and support added considerably to my graduate experience at Composite Vehicle Research Center. I would also like to thank my colleagues from my internship at General Photonics Corporation, Dr. Steve Yao and Dr. James Chen, for giving me the opportunity to work with advanced optical measurement systems. I am also grateful to Dr. Ming Han and his research group for helping me with experiments required for this dissertation.

Furthermore, I thank my fellow lab-mates for providing a friendly atmosphere in the lab that has made me feel welcome and comfortable. I must thank my friends Pavel Polunin and Roshan Angoshtari for their support that made my life and work more enjoyable. Finally, I owe a debt of gratitude to my parents. Thank you for encouraging me in all of my pursuits and inspiring me to follow my dreams!

TABLE OF CONTENTS

LIST OF TABLES

LIST OF FIGURES

CHAPTER 1

OPTICAL TRANSMISSION SCANNING

1.1 Theory and validation of OTS for quantitative NDE of impact damage in GFRP composites

1.1.1 Introduction

Glass fiber reinforced polymer (GFRP) composites are a superior design choice for many applications due to the multitude of benefits they offer, such as light weight, high specific stiffness, high specific strength, and good resistance to chemical agents. Combined with design flexibility and strategic tailoring of mechanical properties, these key advantages have propelled the wide acceptance of GFRP composites in marine, automotive, aerospace, sporting, and construction industries [1]. GFRPs are commonly used in wind turbine blades, boat hulls, tanks, pipes, structural panels, and adhesively bonded joints. However, the increasing demand for such advanced multi-component materials brings along major challenges.

The elastic behavior and fracture of GFRP composites largely depend on the mechanical properties of the fibers and the matrix, the strategic stacking sequence of layers, and the selection of weave patterns. Anisotropy and mismatch of material properties at the interlaminar interfaces are roots for many flaws. These include fiber breakage, matrix cracking, inclusions of foreign objects, and air voids as summarized in Fig. 1.1. Fiber waviness, misoriented plies, and fiber/volume fraction are other important properties of GFRPs to be monitored. A laminated structure subjected to a low velocity impact, such as a tool drop, may develop delaminations between the inner layers that are not visible on the surface. The major concerns for bonded joints are fatigue degradation of the adhesive layer and disbond between adherends, which reduce the load carrying capacity of the joint leading to its premature failure. Hence, non-destructive evaluation (NDE) techniques that can measure both surface and subsurface defects are of critical importance in evaluating the integrity of GFRP composite structures both at manufacturing stage and during their service lives.

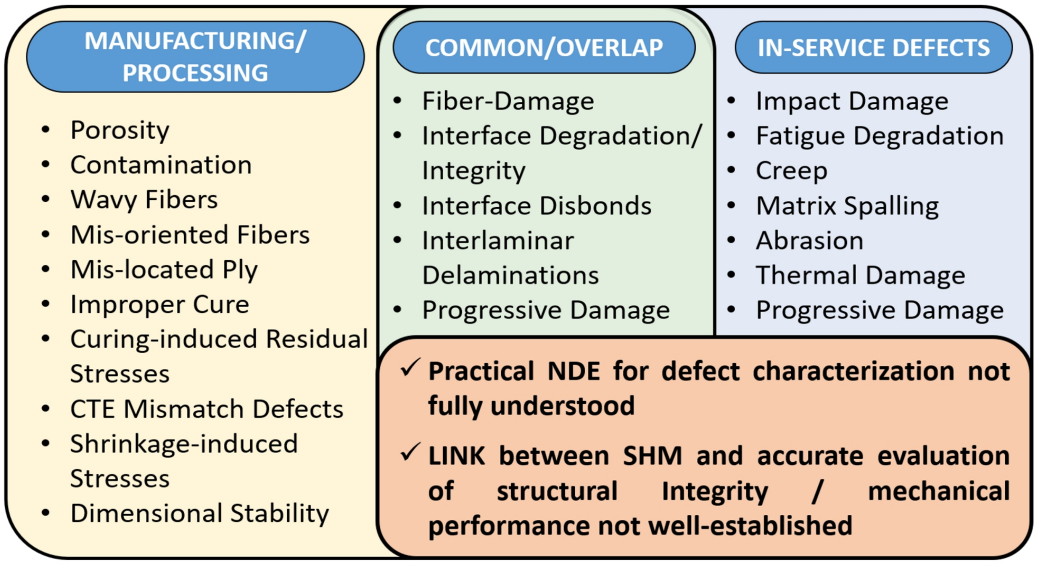

Figure 1.1: Schematic overview of common defects in composites.

Current industrial practice involves the implementation of well-established NDE techniques including ultrasonic testing (UT), X-ray, infrared (IR) or visible range radiation to inspect GFRP structures. Depending on the particular application, each of these methods has its own advantages and limitations. For instance, phased array UT may furnish precise information about the location of damage and its spatial distribution inside the GFRP laminate [2,3]. However, phased arrays require coupling with the test specimen, and they can be rather complex and costly because sophisticated electronics are needed to adjust the time delays between the piezoelectric transducers for proper focusing of the wave energy at the defect site. Hence, relatively simpler systems for immersed and air coupled UT with a single transducer have been routinely used for NDE of composite structures [4–8].

X-ray computed tomography (CT) can provide detailed images of delaminations and other defects in composites [8–12]. However, X-ray CT uses relatively high levels of ionizing radiation, which can be dangerous for inspectors. Moreover, chamber volume for X-ray CT severely limits the size of the sample which can be evaluated. IR thermography is suitable for rapid screening of large components, but it provides little information about the volumetric distribution of damage [10, 13–15].

Optical methods are generally non-invasive, safe, non-contacting, sensitive, whole-field, and inexpensive. Hence, they are often used in biomedical applications to evaluate the properties of biological tissues [16, 17]. Some optical techniques initially designed for medical imaging can be adapted for NDE of GFRP composites. Conventional techniques for optical NDE of GFRP laminates include electronic shearography, digital speckle pattern interferometry (DSPI), digital image correlation (DIC) [10, 18], digital holography (DH), and optical coherence tomography (OCT) [12, 19–22]. These approaches can be used for locating defects and studying the mechanical behavior of GFRP composites. However, a limitation of shearography, DSPI, DH, and DIC techniques is that thermal or mechanical loading of the test specimen is required to create a displacement field and locate structural damage. Both time domain (TD) and Fourier domain (FD) OCT are based upon registering back-scattered and back-reflected radiation; and have been used to study internal structure, defects, and stress in GFRP structures [12, 19–22]. Although TD OCT and FD OCT have their own advantages, they suffer from common major limitation [23, 24]. The penetration depth inside the GFRP specimens is limited to only a few millimeters due to very strong scattering inside GFRP composite. In contrast to OCT, ballistic scanners rely on detecting ballistic photons transmitted through the tissue [25]. Since glass fibers and many epoxy resins have good transmission properties in the visible range, a similar principle was employed in this dissertation for NDE of GFRP composites.

Chapter I presents an optical transmission scanning (OTS) system for quantitative NDE of GFRP samples. The technique provides high-resolution, rapid, and non-contact OT (optical transmittance) scans. Section 1 describes experimental implementation of the technique and advanced data analysis protocol developed for impact damage evaluation. In Section 1, the OTS system is used for inspection of pristine GFRP samples and those damaged by low velocity impact. The number of delaminations across the thickness of the impacted samples as provided by the OTS with advanced data analysis is validated by observing the damage in a cross-section of the impacted GFRP samples after cutting them with a diamond saw. Section 2 provides quantitative comparisons of obtained OT-scans with well-established NDE techniques, such as pulse-echo ultrasound and ultraviolet

dye penetrant testing. Potential applications of OTS for quality control (QC) and NDE of various composite structures are summarized in Section 3. Finally, Section 4 presents the rugged OTS system that provides high-resolution OT-scans (up to 100 μm) of GFRP samples with micro-structural defects and variations. Section 4 also provides some insight into further refinement of OTS by adding 3D imaging capability.

1.1.2 Materials and methods

1.1.2.1 OTS set-up

The experimental setup for acquiring non-contact OT-scans consists of a translation stage that moves the sample, a laser source that illuminates the sample, and a downstream photodetector, as shown in Fig. 1.2a. Fig. 1.2b shows the test setup for a cantilever beam with a mid-plane crack that was used as the "standard" specimen as described below. Fig. 1.2c illustrates how the healthy and impacted plates were examined.

In the present setup, the light source is an iBeam-smart-640s laser diode with 640 nm fundamental wavelength, 1.5 mm beam diameter, and up to 150 mW output power. The transmitted radiation is registered using a DET36A Si detector with 350-1100 nm wavelength range, 14 ns rise time and 13 mm^2 active area. The voltage at the output of the photodetector is directly proportional to registered radiation power. The XY-coordinate stage with stepper motors allows for rapid raster scanning of the GFRP samples with a lateral resolution of 0.25 mm. The lateral resolution of OTS system was mainly determined by the beam diameter and was kept at 0.5 mm in all the experiments described in Section 1.

1.1.2.2 Manufacturing of GFRP samples

GFRP composite samples were manufactured using a vacuum-assisted liquid molding process. The reinforcement was S2-glass plain weave fabric with areal weight of 818 g/m^2, namely ShieldStrand S®, provided by Owens Corning. The GFRP samples comprised eight layers of such

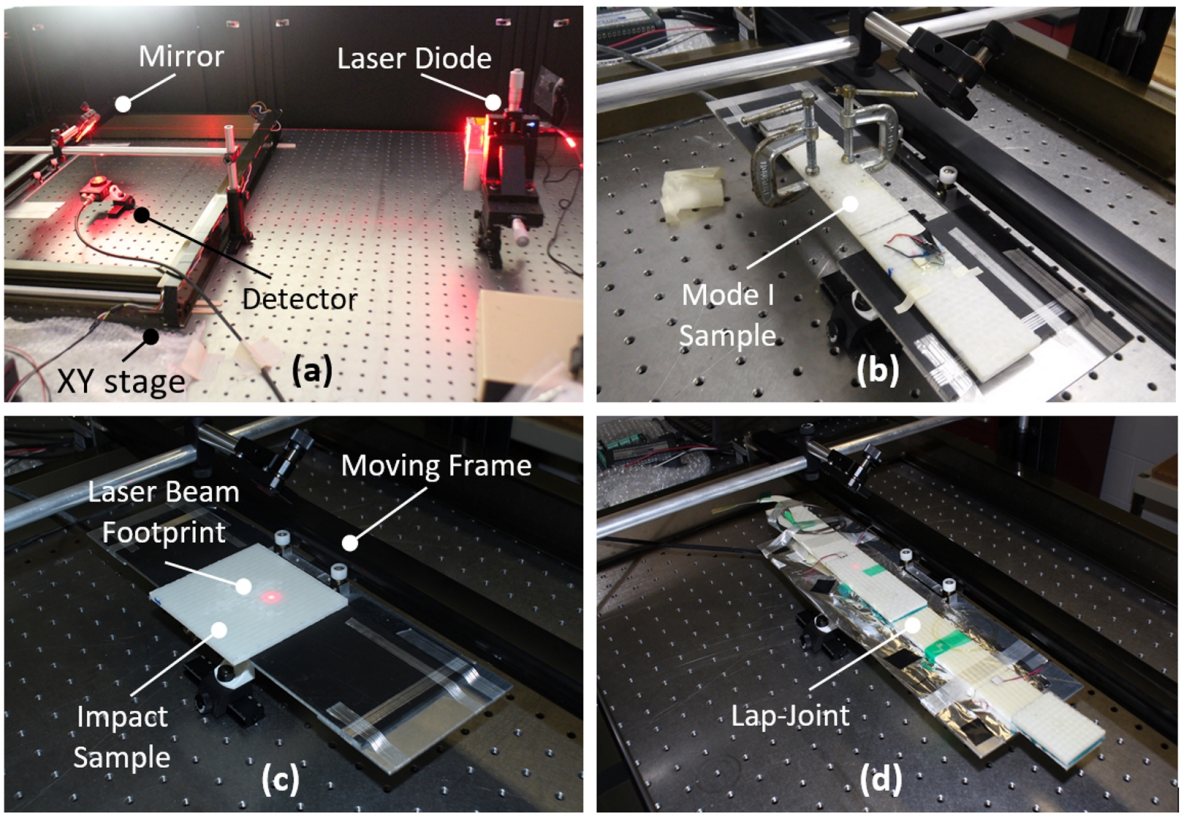

Figure 1.2: Optical transmission scanning: a) experimental setup; (b) test of the "standard" specimen which has a delamination crack (mode I) created by loading it as a double cantilever beam according to ASTM D5528; (c) impacted specimen under test; (d) adhesively bonded lap-joint under test. For interpretation of the references to color in this and all other figures, the reader is referred to the electronic version of this dissertation.

fabric stacked at the same angle. The distribution medium was Resinflow 60 LDPE/HDPE blend fabric from Airtech Advanced Materials Group. The resin was SC-15, a two part toughened epoxy obtained from Applied Poleramic. The GFRP plate (508.0×609.6 *mm*) was manufactured in a 609.6×914.4 *mm* aluminum mold with point injection and point venting. After the materials were placed, the mold was sealed using a vacuum bag and sealant tape, and it was then infused under vacuum at 29 $in\ Hg$. The resin-infused panel was cured in a convection oven at $60^{\circ}C$ for two hours and post-cured at $94^{\circ}C$ for four hours. Finally, impact samples with dimensions of $100 \times 100 \times 4.7$ *mm* were cut from the manufactured GFRP plate using a diamond saw.

1.1.2.3 Material properties of GFRP samples

Elastic properties of the orthotropic GFRP samples used in experimental study were determined from tensile tests, and are presented in Table 1.1 [26].

E_{11}	E_{22}	E_{33}	G_{12}	G_{13}	G_{23}	ν_{12}	ν_{13}	ν_{23}	$\rho, kg/m^3$
23.1	23.1	6.9	3.2	2.54	2.54	0.36	0.28	0.28	1907

Table 1.1: Elastic properties of GFRP material. Young's and shear moduli are measured in GPa.

The refractive index of manufactured GFRP sample can be calculated using the rule of mixtures for the resin and the fiber volumes [19] as:

$$n_c = n_r \cdot V_r + n_f \cdot V_f, \tag{1.1}$$

where n_r and n_f are the refractive indices of resin and fiber, respectively; and V_r and V_f are the volume fractions of resin and fiber, respectively. SC-15 is a combination of bisphenol A diglycidyl ether resin and cycloaliphatic amine curing agent with weight fractions of ≈ 0.77 (100/130) and ≈ 0.23 (30/130), respectively [27]. Weight fractions can be converted to volume fractions using the following relation:

$$\frac{V_e}{V_h} = \frac{\left(\frac{m_e \cdot \rho_h}{m_e \cdot \rho_h + m_h \cdot \rho_e}\right)}{\left(\frac{m_h \cdot \rho_e}{m_e \cdot \rho_h + m_h \cdot \rho_e}\right)}, \tag{1.2}$$

where m_e and m_h are the weight fractions of epoxy and hardener, and ρ_e and ρ_h are the densities of epoxy and hardener, respectively. Using Eq. (1.2), the V_e and V_h for SC-15 can be calculated as ≈ 0.75 (105/141) and ≈ 0.25 (36/141), respectively. Also, density of SC-15 can be calculated as

$$\rho_r = \rho_h \cdot \frac{V_h}{m_h} = \rho_e \cdot \frac{V_e}{m_e} = 1160\, kg/m^3 \tag{1.3}$$

The refractive index of bisphenol A diglycidyl ether resin is $n_e \approx 1.574$ [28], and average refractive index of cycloaliphatic amine hardener is $n_h \approx 1.5$ [29]. Hence, according to Eq. (1.1), refractive index of uncured SC-15 can be estimated as $n_r \approx 1.556$. Density and refractive index of S-glass fiber is 2480-2490 kg/m^3 and 1.523, respectively [30]. The weight fraction of resin in manufactured

GFRP composite is 0.365 [31]. Using Eq. (1.2), volume fractions of resin and glass fibers can be found as $V_r \approx 0.55$ and $V_f \approx 0.45$, respectively. According to Eq. (1.1), the refractive index of resulting GFRP composite can be estimated as $n_c \approx 1.541$. However, it has to be noted that the refractive index of resulting composite depends on many factors, such as the inspection wavelength, curing conditions, working environment, to name a few.

The linear attenuation of GFRP composite material was measured with 1.7 mW incident radiation power for 4-, 8-, and 16-layer laminates with the average thickness of 2.6, 4.6, and 9.2 mm, respectively. In general, for collimated monochromatic radiation in homogeneous media, the power of the transmitted radiation can be calculated using the Beer-Lambert law [32]:

$$P_{as} = P_0 \cdot T_{as} = P_0 \cdot e^{-\sum_{i=1}^{M}\left(\mu_a^i+\mu_s^i\right)\cdot l_i} = P_0 \cdot e^{-\sum_{i=1}^{M}\mu^i\cdot l_i}, \tag{1.4}$$

where P_{as} is the transmitted radiation power that is attenuated by the local material in its pristine state; P_0 is incident radiation power; T_{as} is the transmission coefficient, which accounts only for absorption and scattering in the test specimen in the absence of reflections from its interlaminar interfaces; M is the number of attenuating species of the material sample; μ_a^i, μ_s^i, and μ^i are the absorption coefficient, scattering coefficient, and attenuation coefficient, respectively; and l_i is the thickness of i^{th} specie.

The transmitted radiation power for 4-, 8-, and 16-layer GFRP laminates corresponded to 8.99, 5.22, and 1.52 V output from the receiving photodetector. Thus, from the ratios of the photodetector outputs corresponding to GFRP samples with different thickness, a linear attenuation coefficient μ was found to be approximately 2.7 cm^{-1}. Generally, at a given power and signal to noise ratio (SNR), this value determines the maximum thickness of GFRP composite which can be evaluated using the OTS system.

1.1.2.4 Drop-weight impact tests

The drop-weight tests were performed according to the ASTM D7136 standard using an Instron 9250 HV Dynatup machine that was equipped with an 88.96 kN load cell impactor, a velocity

detector, and a pneumatic brake to prevent multiple impacts (see Fig. 1.3). The edges of the GFRP specimen were clamped by pneumatically assisted grips. The exposed diameter of the composite plate for impact loading was 76.2 *mm*, as per ASTM D7136. A 12.7-*mm* diameter hemispherical head impactor was used for the impact testing. Three GFRP specimens were impacted with 20 *J* energy for subsequent NDE by the developed OTS system.

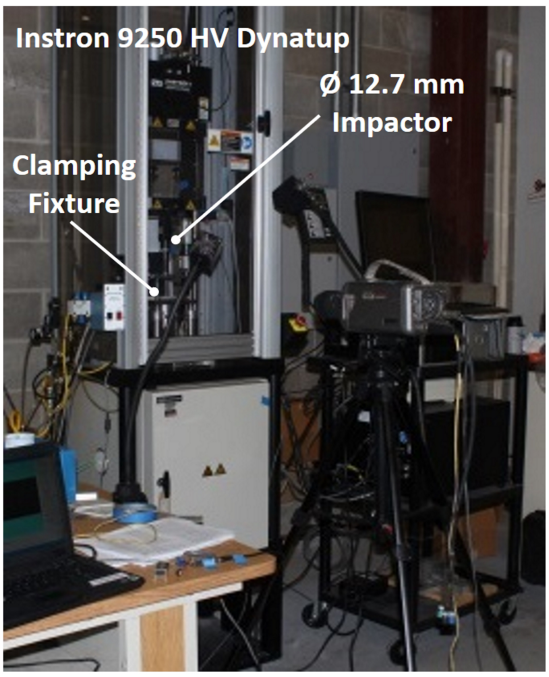

Figure 1.3: Experimental setup for drop-weight impact testing.

1.1.3 Theory of OTS

Since the operating principle of OTS is based upon measuring the optical transmittance of GFRP samples, it is necessary to establish a relationship between the severity of damage and the level of transmitted radiation power measured with the photodetector. When the radiation interacts with the material, such effects as transmission, absorption, chromatic dispersion, diffraction, scattering, reflection, refraction, and conversion can mainly take place [33]. Conversion of radiation occurs when the dielectric polarization of the medium responds nonlinearly to the applied electric field, and can be neglected if the medium is fairly linear. Refraction affects the direction of radiation

propagation, and can be neglected if the incident radiation is normal to the interface. Diffraction is mostly prominent at the edges and is hardly manifested in the bulk of a material. Dispersion effects will be insignificant if the radiation is quasi-monochromatic. Note that these latter three effects influence the direction of radiation propagation rather than the energy or the power of radiation. Power losses partially occur due to reflection, which happens whenever there is a mismatch between the refractive indexes of two materials (e.g., an interface such as a delamination). In order to calculate the reflection coefficients for s-polarized (R_s) and p-polarized (R_p) light at the interface between dielectric materials, the Fresnel equations are used [33]:

$$R_s = \left| \frac{n_1 \cdot \cos\Theta_i - n_2 \cdot \sqrt{1 - \left(\frac{n_1}{n_2} \cdot \sin\Theta_i\right)^2}}{n_1 \cdot \cos\Theta_i + n_2 \cdot \sqrt{1 - \left(\frac{n_1}{n_2} \cdot \sin\Theta_i\right)^2}} \right|^2 , \tag{1.5}$$

$$R_p = \left| \frac{n_1 \cdot \sqrt{1 - \left(\frac{n_1}{n_2} \cdot \sin\Theta_i\right)^2} - n_2 \cdot \cos\Theta_i}{n_1 \cdot \sqrt{1 - \left(\frac{n_1}{n_2} \cdot \sin\Theta_i\right)^2} + n_2 \cdot \cos\Theta_i} \right|^2 , \tag{1.6}$$

where Θ_i is the angle of incidence, n_1 is the refractive index of the material through which the light is reflected; n_2 is the refractive index of the material through which light is further transmitted.

Eq. (1.5) and Eq. (1.6) hold for specular reflection from ideal mirror-like surfaces, and in the case of normal incidence ($\Theta_i = 0$) they reduce to the following formula:

$$R_{sp} = R_s = R_p = \left| \frac{n_1 - n_2}{n_1 + n_2} \right|^2 \tag{1.7}$$

For instance, at normal incidence angle, the specular reflection coefficient R_{sp} for an air ($n_1 = 1$) / glass ($n_2 \approx 1.5$ [30, 34]) interface is around 0.04, meaning that approximately 4% of incident radiation is reflected. However, if the surface is optically rough, such as an interface of interlaminar delamination, diffuse reflection can take place. For example, an analytical model for reflection by roughened plastic surfaces has been proposed and experimentally validated by Torrance et al [35]. The model pictured a studied surface as consisting of small randomly disposed mirror-like facets.

The reflection coefficient R_d predicted by the model depended on specular reflection from these facets plus a diffuse component caused by multiple reflections and internal scattering:

$$R_d(\psi;\Theta,\phi) = \frac{\delta N_{r,s}(\psi;\Theta,\phi) + \delta N_{r,d}(\psi)}{N_i \cdot \cos\psi \cdot \delta\omega}$$
$$= \frac{b \cdot f \cdot N_i(\psi) \cdot \frac{\delta\omega}{4} \cdot F(\psi\prime,\hat{n}) \frac{G(\psi_p,\Theta_p)}{\cos\Theta} \cdot e^{-c^2\alpha^2} + a \cdot N_i(\psi) \cdot \cos\psi}{N_i(\psi) \cdot \cos\psi \cdot \delta\omega}, \quad (1.8)$$

where ψ is the zenith angle of incident radiation; Θ and ϕ are the zenith and the azimuthal angles of reflected flux, respectively; $\delta N_{r,s}$ is the specular component of reflected flux; $\delta N_{r,d}$ is the diffuse component of reflected flux; N_i is the radiance of the small source; $\delta\omega$ is the solid angle of the source; F is the Fresnel reflectance; $\psi\prime$ is the angle of flux reflected from an elementary facet with a surface normal $n\prime$; G is a masking and shadowing factor; ψ_p and Θ_p are the projections of ψ and Θ onto the plane determined by the facet normal and the surface normal; α is the angle at which facet normals are inclined with respect to the normal of the mean surface; f is the area of an elementary facet; a, b and c are scalar constants that depend on surface preparation.

Eq. (1.8) shows that the interaction of the radiation with the material is complex; and the reflection coefficient can change drastically depending on incident angle of radiation, observation angle, surface roughness, and refractive index [35,36]. Since GFRP composite refractive index itself depends on many factors, modeling of light propagation in composite material is quite challenging and cumbersome task.

The analysis provided below offers guidance to the development of a simple and straightforward way to quantify the interior impact damage in materials, particularly laminated composites that have been subjected to impacts. If normally incident monochromatic and collimated laser radiation is passed along a local transect of a fairly linear and homogeneous medium without considering interfaces such as delaminations, it seems reasonable to use modified Eq. (1.4) and approximate the radiation transmitted to a downstream detector as follows:

$$P_{as} = P_0 \cdot (1 - R_{ac}) \cdot T_{as} \cdot (1 - R_{ca}), \quad (1.9)$$

where R_{ac} and R_{ca} are the reflection coefficients of air-to-composite and composite-to-air interfaces, respectively.

Any possible changes in registered power P_{as} defined by Eq. (1.9) can be explained by local variations of fiber/matrix content and thickness over the extent of a composite test specimen in its pristine condition. This conclusion follows from Eq. (1.4), assuming that the reflection coefficients at the top and bottom surfaces, R_{ac} and R_{ca} remain constant.

Logic suggests an extension of Eq. (1.9) to determine the power of the transmitted radiation P_t in the presence of defects such as delaminations by including reflections at interlaminar interfaces:

$$P_t = P_{as} \cdot \left(1 - R_1\right) \cdot \left(1 - R_2\right) \cdot \ldots \cdot \left(1 - R_N\right) = P_{as} \cdot T_1 \cdot T_2 \cdot \ldots \cdot T_N, \tag{1.10}$$

where R_1, R_2,. . . ,R_N and T_{R1}, T_{R2},. . . ,T_{RN} are the local reflection and transmission coefficients for each of the N interfaces in the transect of the sample, respectively.

Actual calculation of P_t using Eq. (1.10) is problematical because a map of delaminations with their respective transmission coefficients, T_{R1}, T_{R2},. . . ,T_{RN}, is not known a priori, and the determining of it would be forbiddingly counterproductive. Offered here is a practical solution that replaces the set of unknown transmission coefficients by a single "standard" value T:

$$P_t \approx P_{as} \cdot T^N \tag{1.11}$$

The transmission coefficient T is determined by scanning a representative sample containing a single interior delamination. Hence, if delamination is considered to be the main damage mechanism, then Eq. (1.11) can be used to relate the registered transmitted power and the number of delaminations.

1.1.3.1 Determination of a "standard" transmission coefficient T

The value of T was obtained from the OT-scan of a double cantilever beam (DCB) sample after the mode I interlaminar fracture toughness test (as per the ASTM D5528 standard) as shown in Fig. 1.2b. The DCB sample was comprised of eight layers of plain-weave S2 glass with a single fracture-induced delamination between the four upper and four lower laminates. The OT-scan was

acquired with a laser output power of 5.2 mW and a lateral resolution of 0.5 mm. The transmission coefficient was calculated as the ratio of the transmitted radiation powers P_t and P_{as} averaged over two separate 2 cm^2 regions of the sample, one region containing the crack and the other without a crack as shown in Fig. 1.6b. The sample was clamped with a few miniature C-clamps prior to OTS to ensure that the crack was closed as tightly as possible. The value of T was found to be 0.61, apparently owing to the diffuse surface of the crack interface.

1.1.3.2 Robustness of OTS

It should be noted that Eq. (1.4) and Eq. (1.10) strictly hold for only ballistic photons, which travel from the point-like radiation source down to the photo-detector in a straight line. However, if a collimated beam with a large diameter propagates through a scattering medium such as a GFRP, the transmitted radiation can be scattered, taking on some sort of angular distribution. In such a case, the size of the delamination/air gap inside the sample, variation of sample thickness, and the distance between the detector and the output interface might affect the measurement of the transmitted radiation. In addition, propagation of a wide laser beam through the edges of delaminations will introduce partial attenuation and, possibly, edge diffraction effects. These issues can be addressed by using a laser with a small beam diameter, or by installing a diaphragm with a pin hole in front of the detector. In the first version of OTS setup, the effect of a relatively large beam footprint ($d \approx 1.5$ mm) was compensated for in signal processing, which allowed for more accurate detection of delamination boundaries. It was also noticed that the uncertainties in the determinations of the delamination contours were mainly governed by the size of the footprint of the laser beam and the associated transition region rather than by uncertainties in the estimation of T, as will be seen in the next section. Another important consideration is that Eq. (1.11) provides a self-referencing capability for the developed system. That is to say, the thickness of the composite sample and the delamination depth do not affect the transmission coefficient for a single interface (delamination) T, because it is defined as the ratio of the radiation P_t transmitted through the region with the delamination to the radiation P_{as} transmitted through the healthy region of the sample.

1.1.4 Results and discussion

The previously described experimental setup for OTS was used for inspection of the GFRP samples shown in Fig. 1.4. The first sample was healthy (no impact), and the second one was subjected to low velocity impact of 20 J. OT-scans were acquired with a laser output power of 5.2 mW and a spatial resolution of 0.5 mm. The distance between the bottom side of the sample and the receiver was 5 mm. The raw results before post-processing are demonstrated in Fig. 1.5. As seen from Fig. 1.5a, some areas of the plain weave GFRP plate with no damage had higher transmittance than other areas, which was apparently caused by thickness variations of the sample and glass fiber irregularities as follows from Eq. (1.9). The transmitted power P_{as} was minimal when radiation propagated via clusters of fibers. In contrast, the highest P_{as} corresponded to propagation of radiation via resin-rich areas. Hence, in the case of the pristine GFRP composite, the amplitude values in the output of the photodetector fell in a region $\Gamma_0 = \left[A_{max}, A_{min}\right]$ which was directly proportional to the range of transmitted powers $\left[P_{as}^{max}, P_{as}^{min}\right]$.

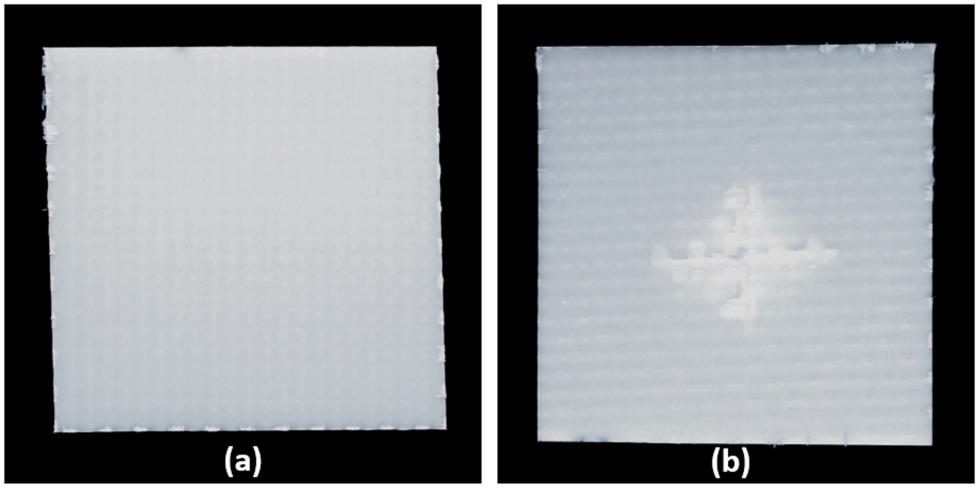

Figure 1.4: (a) Healthy GFRP sample (no impact); (b) GFRP sample after $E = 20\ J$ impact.

The incident power from the laser source, P_0 was adjusted before each scan such that the maximum amplitude registered by the photodetector A_{max} was as close as possible to its saturation limit of 10 V in order to provide the widest measurement range and the highest SNR.

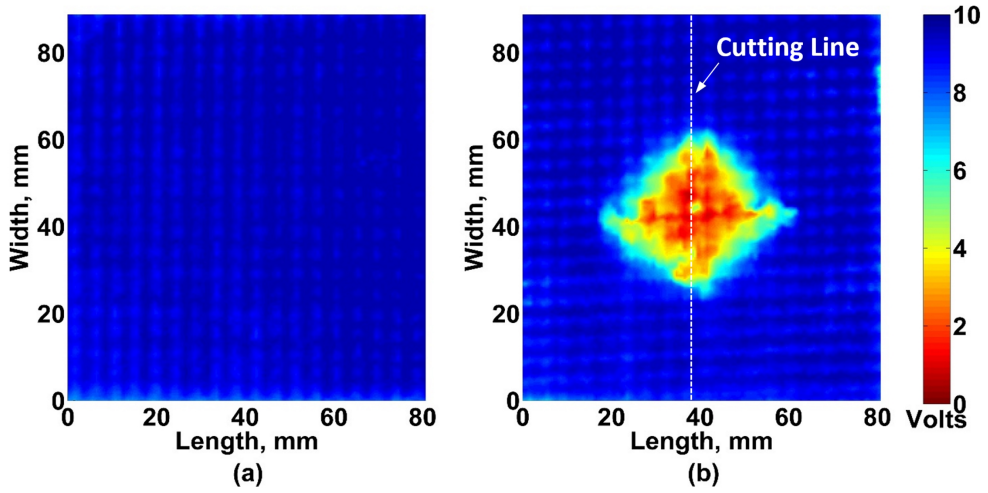

Figure 1.5: (a) OT-scan of healthy GFRP sample; (b) OT-scan of the GFRP sample after $E = 20\ J$ impact.

1.1.4.1 Advanced signal processing for quantitative evaluation of impact damage

Owing to the mismatch of material properties at the interfaces within the GFRP composite plate, the low velocity impact with $E = 20\ J$ resulted in multiple interlaminar delaminations whose areas increased with depth. In order to quantify the extent and severity of impact damage from the OT-scans, an advanced signal processing procedure was developed to determine the delamination contours as a function of depth. The concept is illustrated in Fig. 1.6. Assuming that delamination is the main damage mechanism, the registered power of radiation transmitted through the sample P_t can be divided into discrete amplitude levels depending on the number of interfaces below the scan point that affect the beam power. If the transmission coefficient T of a similar GFRP sample with one delamination in its mid-plane is known and only diffuse reflection is assumed, meaning no increase in scattering or absorption is taken into account, the range $\left[A_{max}, A_{min}\right]$ associated with the pristine composite can be simply scaled down to plot damage contours representing N delaminations. The scaling factor can be established through the use of Eq. (1.12) as [37]:

$$\Gamma_N = \Gamma_0 \cdot T^N = \left[A_{max}, A_{min}\right]^N \tag{1.12}$$

As suggested above, the governing assumption here is that each delamination encountered has a transmission coefficient T that is reasonably near the value found for the single delamination in

the "standard" specimen. However, one might encounter intensity values that may not fall in any of these discrete intervals. This happens because the incident laser beam is not focused and has a footprint of $d \approx 1.5\ mm$. It was observed that at the boundaries between each delamination and the sample there were smooth transition regions that were caused by partial attenuation of the incident beam. Fig. 1.6a through Fig. 1.6c illustrate this behavior conceptually for regions near the delamination in the "standard" specimen (Fig. 1.6b) and near the specimen supporting structure (Fig. 1.6c). The widths of the transition regions were estimated to be $2 \cdot d \approx 3\ mm$. So, the intermediate values were arbitrarily split equally between the adjacent levels, and the new contour margins were computed as illustrated in Fig. 1.6d to be [37]:

$$C_N^{max} = \frac{\left(A_{max} \cdot T + A_{min}\right) \cdot T^{N-1}}{2}, \tag{1.13}$$

$$C_N^{min} = \frac{\left(A_{max} \cdot T + A_{min}\right) \cdot T^{N}}{2}, \tag{1.14}$$

where C_N^{max} and C_N^{min} are the upper and lower levels of contours corresponding to the N^{th} delamination, A_{max} and A_{min} are the maximal and minimal amplitudes of registered radiation transmitted through a healthy composite, taken as the amplitudes of the corresponding detector output voltages, and T is the transmission coefficient of the "standard" sample with a single delamination in its mid-plane.

The values of A_{max} and A_{min} were computed for healthy and impacted GFRP samples by considering the histograms of their healthy regions only (see Fig. 1.6a). The voltage outputs of the photodetector were split into 512 bins, whose mean values were sorted in ascending order. The A_{min} was selected as the average of the first bin containing more than 25 elements. Similarly, the A_{max} was assigned the average of the last bin, whose number of elements exceeded the same threshold. This procedure was applied to remove measurement variations potentially caused by the circuit noise, tilt of the sample, surface roughness or contamination, and vibration of the fixture during the acquisition of the OT-scans.

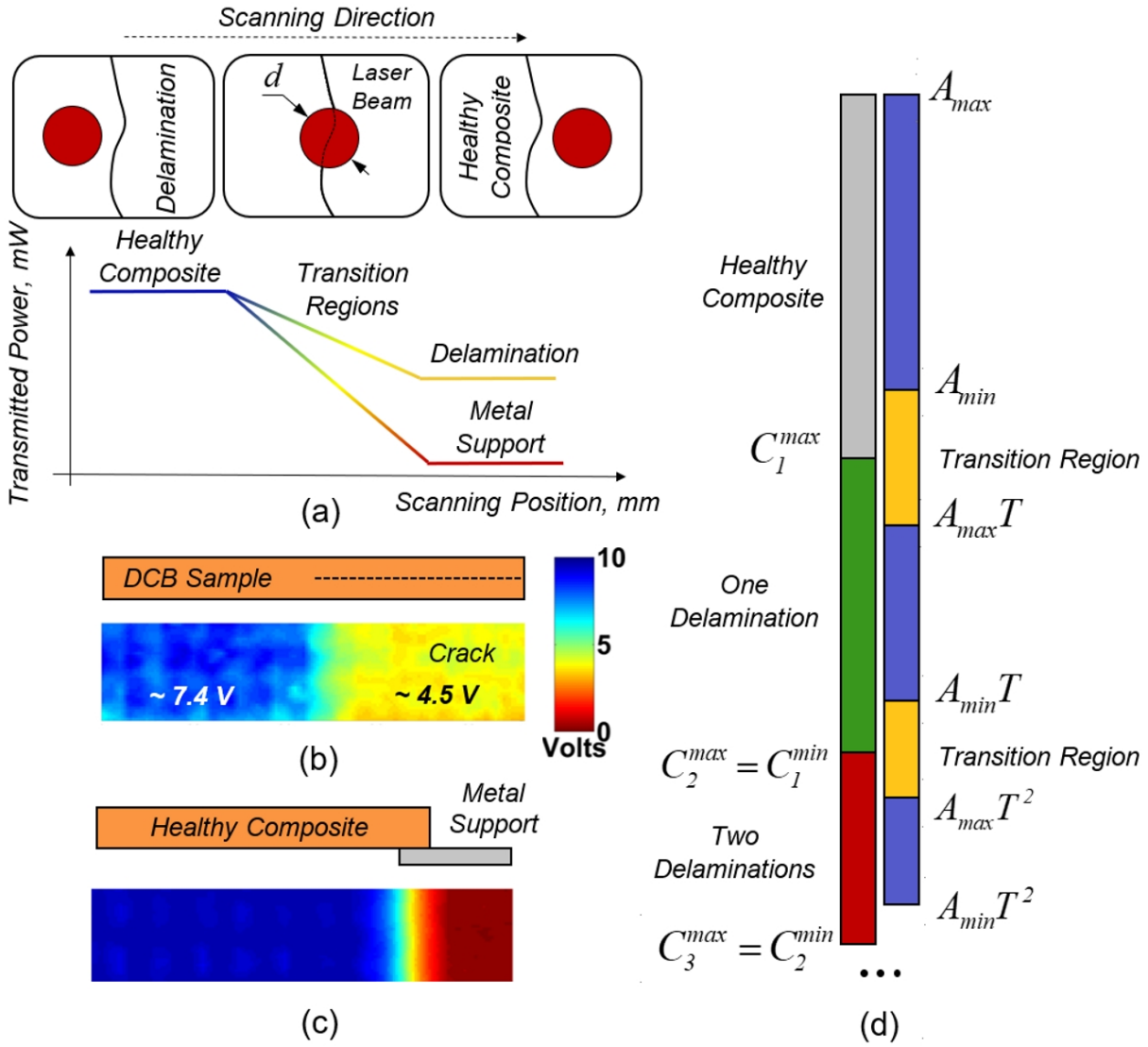

Figure 1.6: (a) Gradual change of transmitted radiation power across delamination boundary due to partial beam scattering through the transition regions; (b) OT-scan of the double cantilever beam (DCB) sample with a crack that served as the "standard"; (c) OT-scan of the metal-to-composite interface in the support region; (d) determination of contour levels corresponding to different numbers of delaminations.

1.1.4.2 Post-processed OT-scans of GFRP samples

Post-processed OT-scans of healthy and impacted GFRP samples are shown in Fig. 1.7a and Fig. 1.7b. The color bar of contour plots was partitioned as per Eq. (1.13) and Eq. (1.14) to highlight the healthy regions of each composite plate and the regions with given numbers of delaminations. As seen from Fig. 1.7b, the total delamination count was the largest in the middle region of the

impacted sample, and it decreased radially from the point of impact. In addition, the extents of delaminations were slightly larger along the principle directions of the glass fibers, $[0/90]_4$. The results demonstrated that it was difficult to determine the differences between contours for

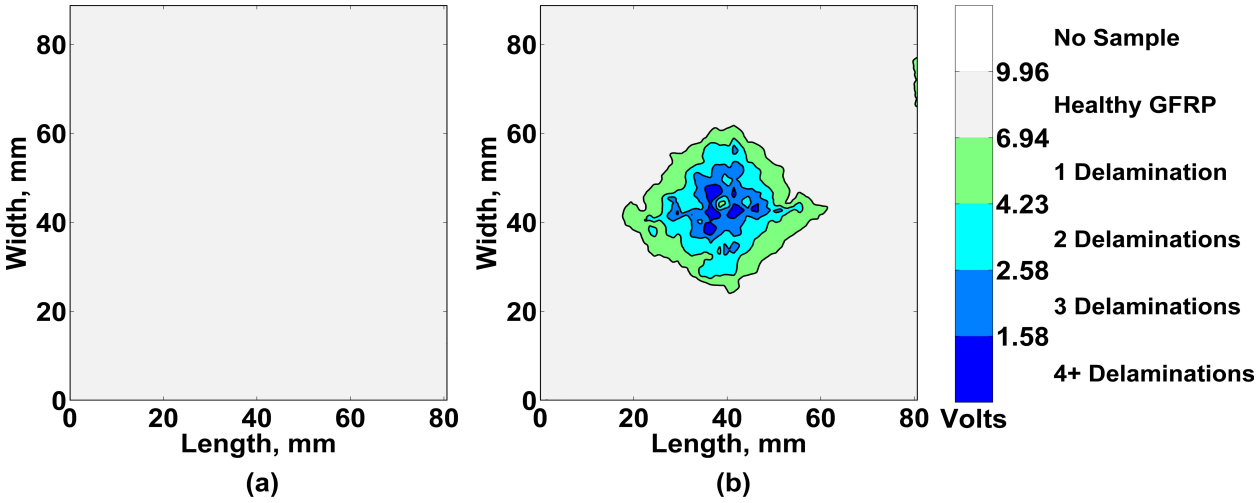

Figure 1.7: (a) Post-processed OT-scan of the healthy sample; (b) post-processed OT-scan of the sample after $E = 20\ J$ impact.

a large number of interlaminar defects, in particular, for $N > 4$, because the margins became too closely spaced and the overall level of radiation intensity at the photodetector approached the noise limit. Hence, whenever the voltage output of the photodetector fell below $C_4^{min} = 1.58\ V$, this indicated that N exceeded four, which is simply denoted as "4+" in the subsequent figures. Fig. 1.8 provides comparisons of the damage extent as a function of the number of delaminations. The results demonstrate that regions of the GFRP sample where the impact created only one or two delaminations were significantly larger than the regions where three and more delaminations appeared.

1.1.4.3 OTS validation

The impacted sample (E= 20 J) shown in Fig. 1.4b was cut with a diamond saw at location $x = 37.8\ mm$ along its y-axis (see the corresponding OT-scan in Fig. 1.5b). The left half of the sample was arbitrarily chosen for determining the delamination contours. Its new face created

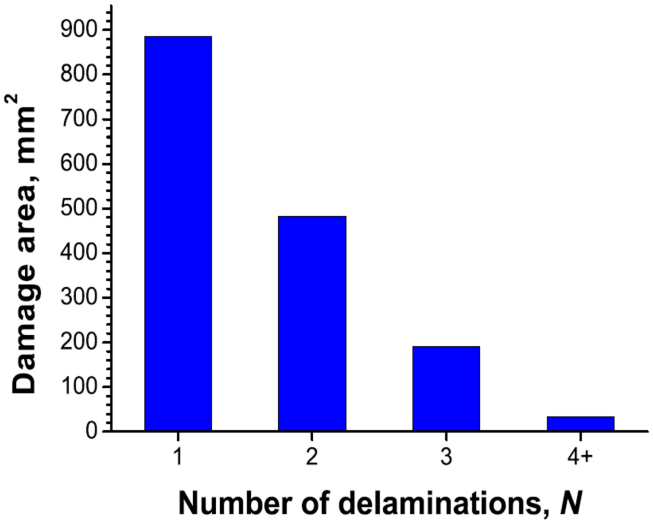

Figure 1.8: Estimated damage area corresponding to different numbers of delaminations N.

after cutting was saturated with a UV dye penetrant, and it was left to soak for 30 minutes. After absorption of the UV dye by the interlaminar defects, the sample was illuminated with a UV lamp in a dark ambience in order to enhance the contrast between the delaminations and the pristine GFRP material in the transect. The image of the cross-section was taken with a digital camera, and it was later converted into a gray-scale format for post-processing in MatLab with the result shown in Fig. 1.9a. Delaminations were identified using the two-stage Canny edge detection algorithm followed by Wiener filtering to smooth the image and remove the residual artifacts [38]. Applying a hard threshold to the resulting image effectively converted it into a binary representation, whose high-value pixels determined the delamination boundaries, and whose zero-value pixels corresponded to the pristine GFRP material. Fig. 1.9b shows the obtained binary image merged with the original digital picture of the cross-section area. The delaminations were highlighted as red curves, and the total number of delaminations at a given scanning position was easily determined by automatically counting the number of curves through the height of the image. Fig. 1.9c illustrates the OT-linescan of the corresponding cross section of the GFRP sample. In this figure, the curve is partitioned based on the voltage levels determined from Eq. (1.13) and Eq. (1.14). Thereby, if the total number of delaminations N in the cross-section changes, this is highlighted with a different color in accordance with the discrete color map on the right hand side.

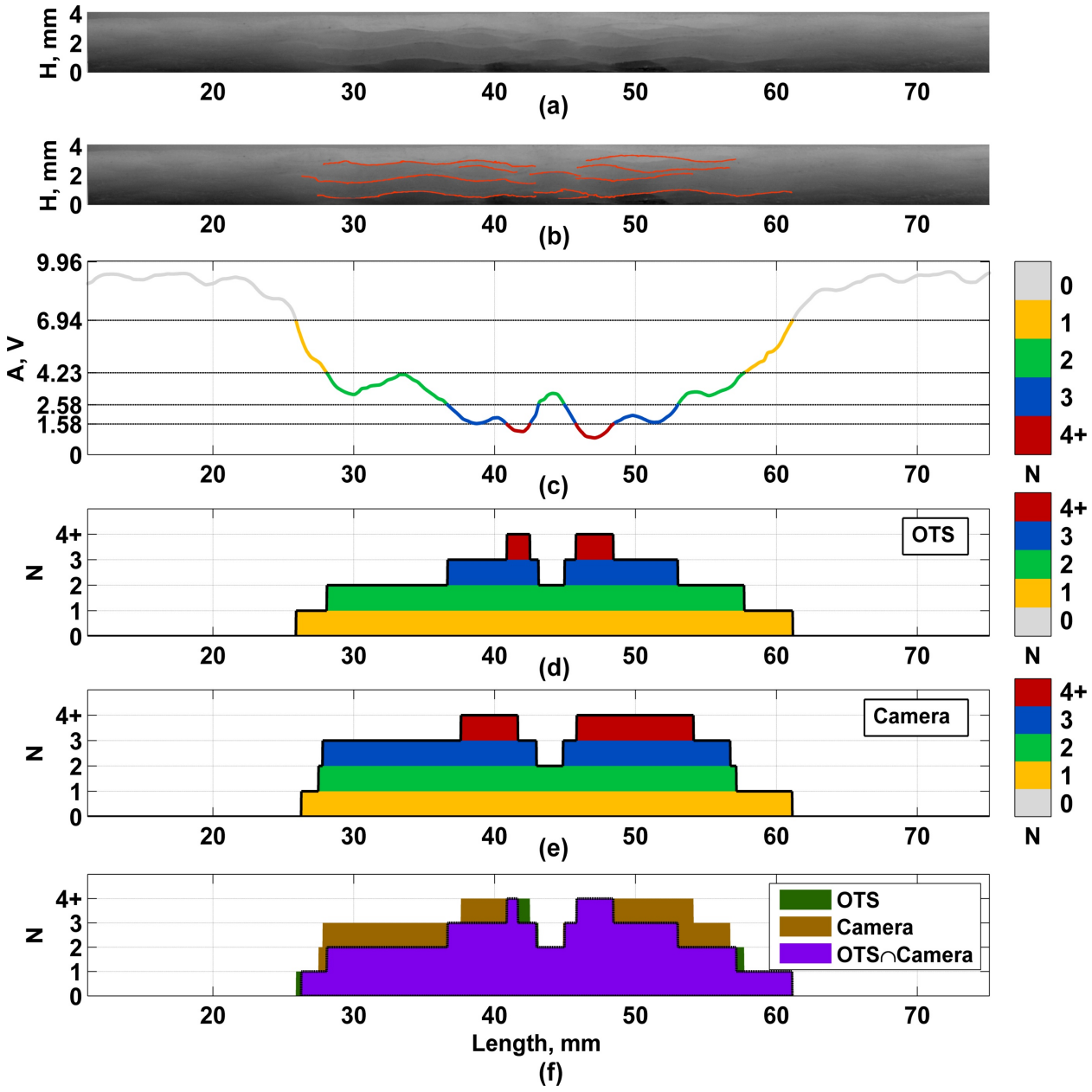

Figure 1.9: (a) Cross-section of the GFRP sample (thickness $H = 4.8\,mm$, impact energy $E = 20\,J$); (b) delaminations identified using edge detection and filtering of the image data; (c) corresponding OT-linescan; (d) the number of delaminations, N registered by the OTS; (e) the number of delaminations, N along the cross-section length obtained from post-processed digital camera images; (f) comparison of results obtained with OTS and digital camera imaging wherein the regions in which the numbers of detected delaminations match are highlighted in purple. For interpretation of the references to color in this figure legend, the reader is referred to the web version of this report.

The total number of delaminations along the cross-section of the GFRP sample, determined from the OT-linescan and the post-processed digital image, are shown in Fig. 1.9d and Fig. 1.9e, respectively. Both plots are well aligned along the x-axis, which indicates that the OTS technique accurately determines the outer margins of the impact damage. In addition, one of the characteristic features of the scanned sample is that only two delaminations appear in the middle of the cross-section, as seen from the Fig. 1.9b. This trend is very well captured by the OTS system. In Fig. 1.9f both results are plotted on top of each other, and the regions in which the numbers of delaminations detected by the two methods match are highlighted in purple. As seen, the results obtained with OTS and the digital camera match well, differing at most by one delamination. This difference can be explained by the fairly large transition region of the laser beam ($2 \cdot d \approx 3\ mm$) and light scattering previously discussed. At the same time, the digital image of the cross section shows the distribution of the impact damage only in two dimensions. However, the damage is three-dimensional, and if the number of delaminations in the plane parallel to the transect of the sample is not constant within the footprint of the laser beam, the amount of the received radiation at the downstream photodetector would be affected. A simple way to improve the agreement and to enhance the resolution would be to reduce the beam diameter.

1.1.5 Conclusions

Section 1 presented optical transmission scanning (OTS) as a valuable technique for quantitative NDE of GFRP composites. In OTS, structural damage is detected and evaluated by measuring the amount of radiation transmitted through the test samples. OT-scans are rapidly acquired without any couplants and do not require extensive processing. Moreover, OTS can be readily applied for inspection of thick GFRP structures. A special post-processing technique for raw OT-scans was developed for evaluation of the damage introduced in GFRP composite by low velocity impacts. A basic prototype of the OTS system was able to accurately identify the total number of delaminations, up to a maximum of four, in the cross-section of the GFRP sample at each scan point. If more than four delaminations were encountered along a transect, the exact number could

not be ascertained with basic OTS system. Additional useful information about the severity of impact damage was obtained by measuring the extent of each detected delamination. The OTS and advanced image processing algorithm were experimentally validated by comparing OT-linescans with the observed distribution of delaminations in the cross-section of GFRP samples after cutting them with a diamond saw. The presented OTS setup is a promising tool, which lays groundwork for cost-effective, non-contact, rapid, and quantitative NDE of GFRP composite structures.

1.2 Quantitative Comparison of OTS with Conventional NDE Techniques

In this Section, the extent of the damage obtained from OT-scans is compared with that identified by other NDE techniques such as UV DPT and conventional water-immersion pulse-echo UT C-scans. In addition, quantitative comparison of OT-scans with UT C-scans is provided by converting the images to a normalized damage scale.

1.2.1 Impact Testing and Standard NDE Techniques used for Comparison with OTS

1.2.1.1 Drop-weight impact tests

Drop-weight impact tests were performed similar to approach described in Section 1.1, but with addition of two extra impact energy levels: $E = 40\,J$, and $E = 80\,J$. After each impact the GFRP samples were evaluated using visual inspection, pulse-echo UT, UV DPT, and OTS.

1.2.1.2 Pulse-echo UT Testing

Water-immersion UT in the pulse-echo mode was utilized for evaluating damage extent in the impacted GFRP samples (see Fig. 1.10). An ULTRAPAC II system with a 1 MHz, 25.4 mm transducer was used for data acquisition, and UTwin software was used for imaging and analysis. ToF and amplitude of back-surface reflection was determined by setting the electronic gate on each A-scan.

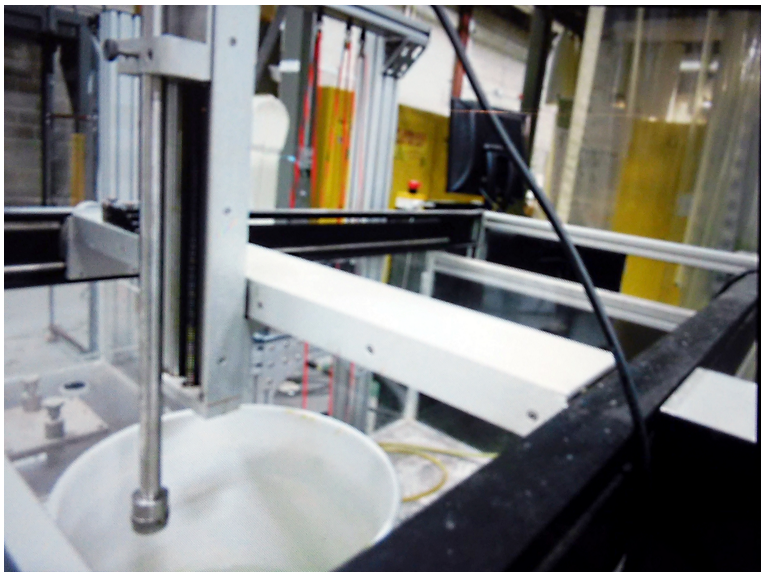

Figure 1.10: Pulse-echo UT inspection with ULTRAPAC II system.

1.2.1.3 Ultraviolet Dye Penetrant Testing

UV DPT was performed to evaluate the extent of surface and interlaminar damage in the GFRP specimens after the low-velocity impacts at different energies. Fluorescent dye penetrant Zyglo ZL-27A was sprayed onto the front and rear sides of each specimen. After 30 minutes of soaking, excess penetrant was removed using acetone. Each side of the sample was illuminated with a UV lamp, and the fluorescence was captured using a digital camera.

1.2.2 Experimental Results and Discussion

1.2.2.1 Mechanical response of the GFRP composite laminates to low velocity impacts

Impact energies of 20, 40, and 80 J were selected for the drop weight experiments, and a minimum of three tests were performed for each material configuration and impact energy value. The reaction force due to the interaction between the laminate and the impactor was measured by a strain gauge transducer located on the shank of the impactor. Fig. 1.11a demonstrates the representative force-time curves for each impact energy level. The first load drop observed at $t \approx 1\ ms$ primarily corresponds to the occurrence of initial damage in the form of localized matrix

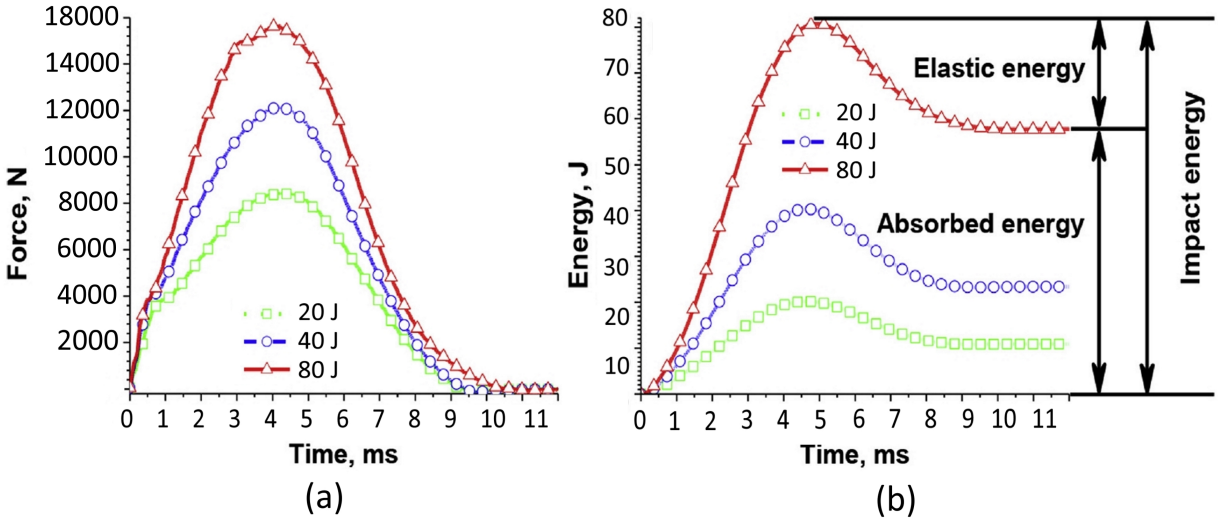

Figure 1.11: (a) Force-time curves; (b) energy-time curves.

cracking and delamination at the contact point of the impactor, whereas the second load drop that follows the peak of the curve is associated with extensive matrix cracking, fiber breakage and delamination in the wider area surrounding the impactor [22, 39]. The point of the first damage onset was nearly insensitive to strain rate, since the initial damage occurred around 3.75 kN in all test configurations. On the other hand, the influence of strain rate on the peak reaction force of GFRP was more evident as the energy level was increased from 20 to 80 J. In the absence of penetration and perforation by the impactor, the damage extent can be estimated using the damage degree parameter, μ, as introduced in Eq. (1.15):

$$\mu = \frac{L_{wi}}{E_e^{(S)}\left(t_{mp}\right) + L_{wi}} \tag{1.15}$$

where L_{wi} is the dissipated energy due to internal mechanisms, $E_e^{(S)}$ is the elastic energy in the specimen, and t_{mp} is the time of the maximal penetration at which the impactor reaches null velocity.

Generally, the damage degree is defined as the ratio between the dissipated energy and the impact energy. Because the impact energy applied on the laminate was not high enough to develop either penetration or perforation, the difference between the impact, rebound (elastic), and absorbed energies for each impact level could be easily observed, as illustrated in Fig. 1.11b. As shown in

Fig. 1.12, the damage degree demonstrated a monotonically growing trend as the impact energy increased. These results imply that the internal dissipated energy (L_{wi}) due to delamination, matrix cracking, and fiber breakage was more significant at the higher impact energy level of 80 J than at 20 J.

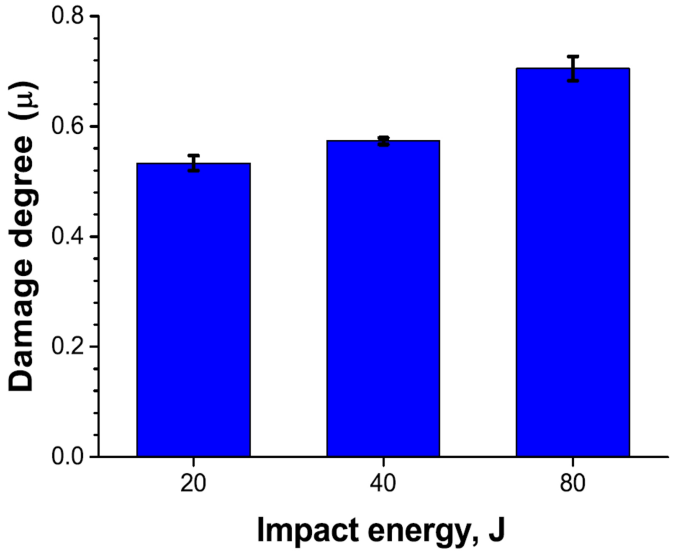

Figure 1.12: Damage degree corresponding to different impact energies.

1.2.2.2 OT-scans of impacted GFRP samples

Top surface images of four of the GFRP samples used in experimental studies are shown in Figure Fig. 1.13. OT-scans were acquired using the previously described setup with a laser output power of 5.2 mW. The results are demonstrated in Fig. 1.14. Post-processed OT-scans of the GFRP samples are shown in Fig. 1.15. The color bar of the image was partitioned using the procedure described in Section 1. As seen from Fig. 1.15, the total number of delaminations was the largest in the middle of the tested samples, and decreased radially from the point of impact. In addition, the extent of the delaminations was slightly larger along the principle directions of the glass fibers, $[0/90]_4$. For the 80 J impact, the introduced damage reached the boundaries of the clamping fixture. Fig. 1.16 provides comparisons of damage extents for different impact energies and calculated numbers of delaminations. According to the results, the area covered by one and

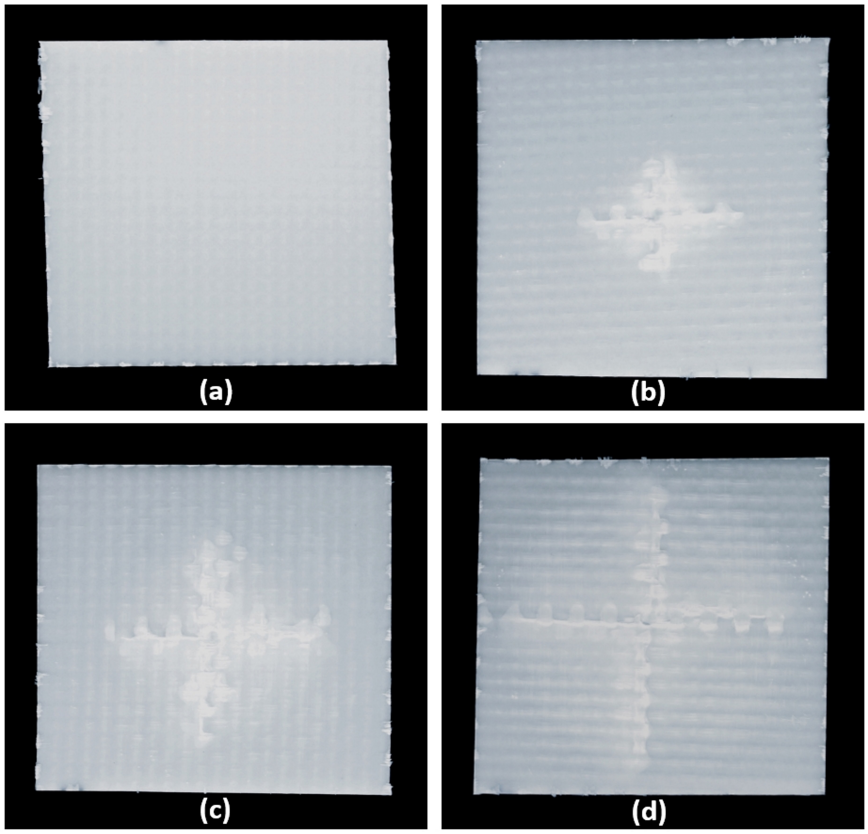

Figure 1.13: Top surface images of tested GFRP samples: (a) healthy GFRP sample; (b) GFRP sample subjected to 20 J impact; (c) GFRP sample subjected to 40 J impact; (d) GFRP sample subjected to 80 J impact.

two delamination layers was significantly higher for the 80 J impact energy than that for the 40 J impact, while the damage areas corresponding to three and four delaminated layers were relatively similar. That is, the areal extent of damage reduced with increasing number of delaminations.

1.2.2.3 UT C-scans of GFRP samples

GFRP samples were placed in a water tank for the UT inspection. C-scans were obtained in the pulse-echo mode using the ULTRAPAC II system. A piston source transducer was kept 15 cm above the surface of the test samples to produce a more uniform ultrasonic beam and avoid operation in the near field. The transducer was driven at 900 V, which is the peak voltage of the pulser-receiver module. The actuation frequency of 1 MHz provided an acceptable amplitude of a back-wall reflection. Longitudinal waves excited at higher frequencies (e.g., up to 20 MHz)

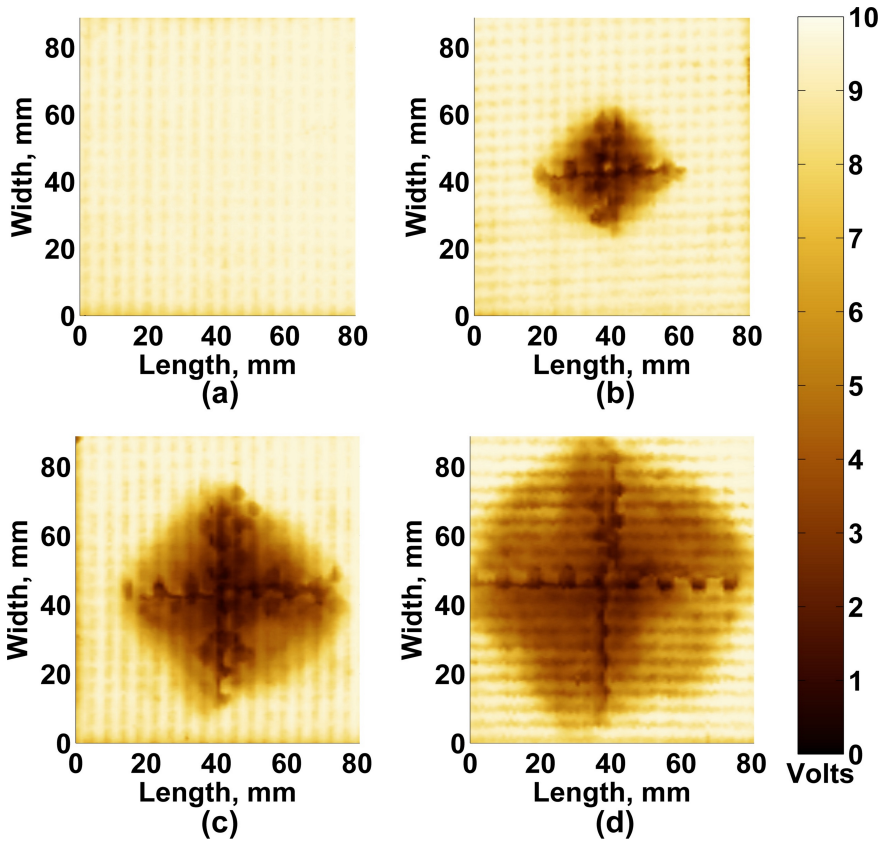

Figure 1.14: OT-scans: (a) healthy GFRP sample; (b) GFRP sample subjected to 20 J impact; (c) GFRP sample subjected to 40 J impact; (d) GFRP sample subjected to 80 J impact.

would have shorter wavelengths and better sensitivity to defects. However, the manufactured GFRP samples had 5-6 volume fraction of air voids with average size of 0.3 mm, which increased wave scattering dramatically above 1 MHz. Figure 7 shows typical A-scans acquired on the pristine and damaged regions of the GFRP sample after the 20 J impact.

In Fig. 1.17, A_1^{UT} is the reflection from the top surface, and $\left(A_2^{UT}\right)_H$ is the reflection from the rear surface of the test sample. $\left(A_2^{UT}\right)_D$ denotes the amplitude of the wave packet, which is received when a delamination is present in the layer above the bottom side of the test sample. As seen from the image, the interlaminar defect affects both amplitude and ToF of the second wave packet, while the shape of the first wave packet remains nearly the same. The results of the UT inspections also demonstrated that it was quite difficult to resolve reflections from multiple interfaces in the A-scans. If two delaminations occur in subsequent layers, the UT system used in the experiments cannot resolve them accurately, because the time support of the wave packets

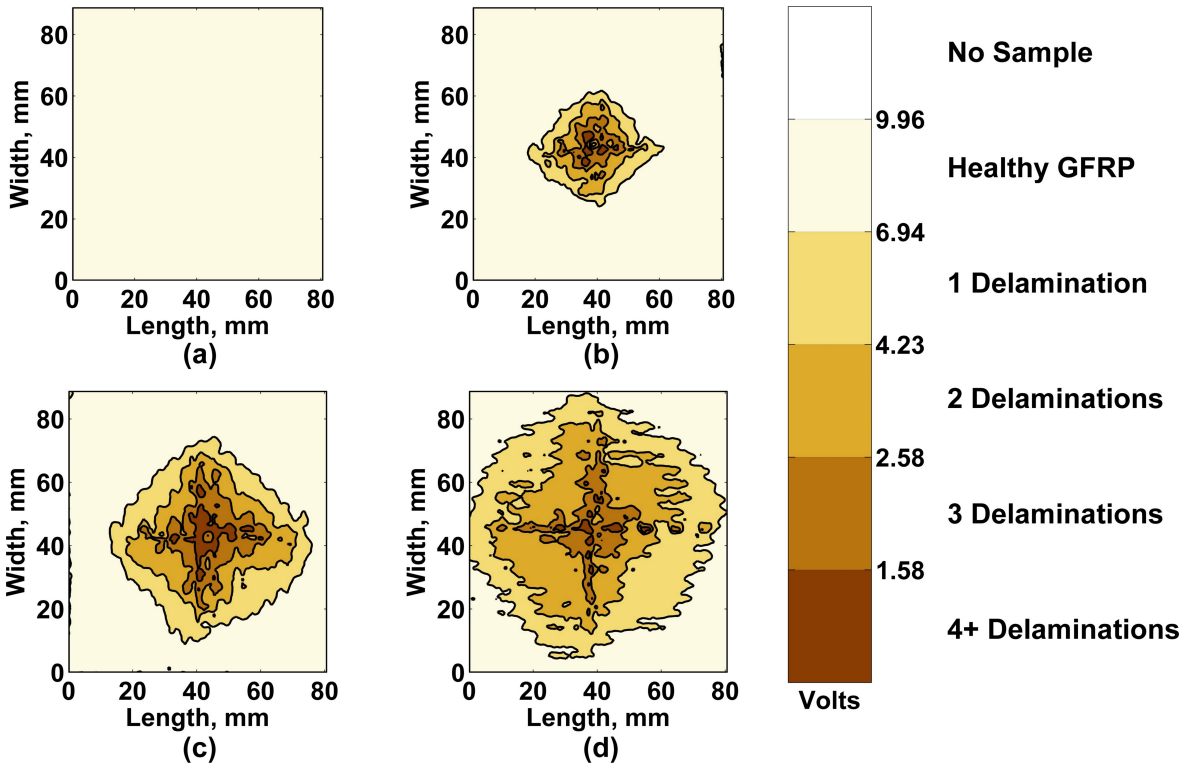

Figure 1.15: Delamination profiles identified using enhanced signal processing of OT scans: (a) healthy GFRP sample; (b) GFRP sample subjected to 20 *J* impact; (c) GFRP sample subjected to 40 *J* impact; (d) GFRP sample subjected to 80 *J* impact.

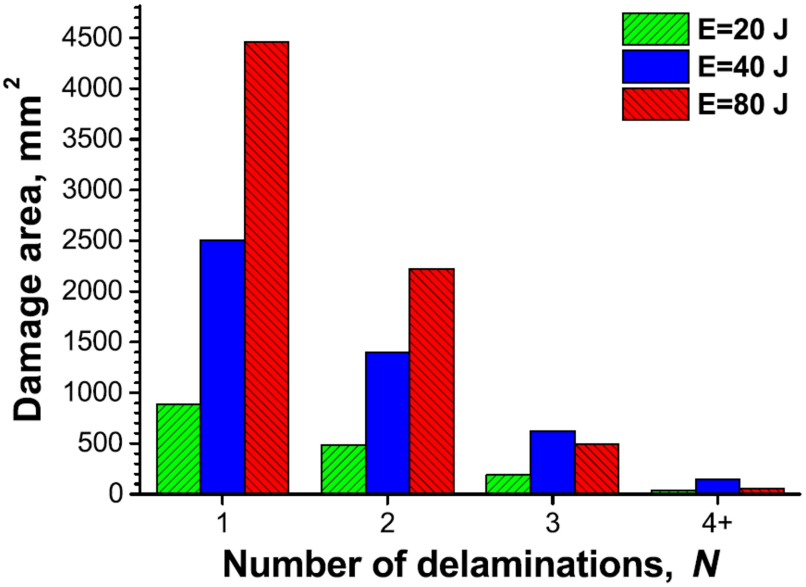

Figure 1.16: Estimated damage area corresponding to different numbers of delaminations as obtained from OT scans.

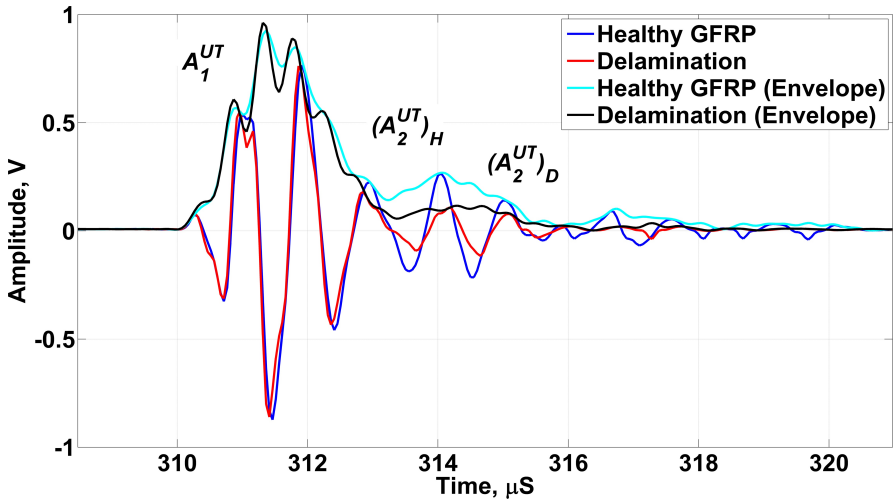

Figure 1.17: UT A-scans of the GFRP sample subjected to $E = 20\ J$ impact ($f = 1\ MHz$).

would be comparable to the time delay between their arrivals. That is, the wave packets would merge together. This issue could not be eliminated by reducing the count or the duration of the excitation pulses owing to high scattering in the bulk GFRP material. The composite samples soaked in the tank for some period of time, so the subsurface defects apparently became filled with water.

Fig. 1.18 demonstrates the amplitude ratio A_1^{UT}/A_2^{UT} that approximately characterizes wave scattering across the delaminations in the test specimen. As seen from the UT C-scans, the ratio increases in the vicinity of the impact location, indicating more severe damage. The overall damage extent is measured by setting a hard threshold on the obtained image data. The thresholding level is determined for each sample individually by considering the maximal amplitude ratio outside the damage area. The overall procedure is similar to post-processing of the OT-scans in Section 1. If the amplitude ratio is lower than the smallest value in the healthy region after histogram filtering, the pixel of the image is treated as a damage. Damage contours identified from the previously described UT C-scans are shown in Fig. 1.19. The results demonstrated that the overall damage extent grows with increasing impact energy. The ToFs of the reflections from the outer surfaces of the GFRP samples and the delaminations were automatically extracted from the A-scans by setting gates in the ULTRAPAC II software and detecting the positions of the peaks. The relative difference between the respective times of arrival are plotted in the UT C-scans that are shown in Fig. 1.20.

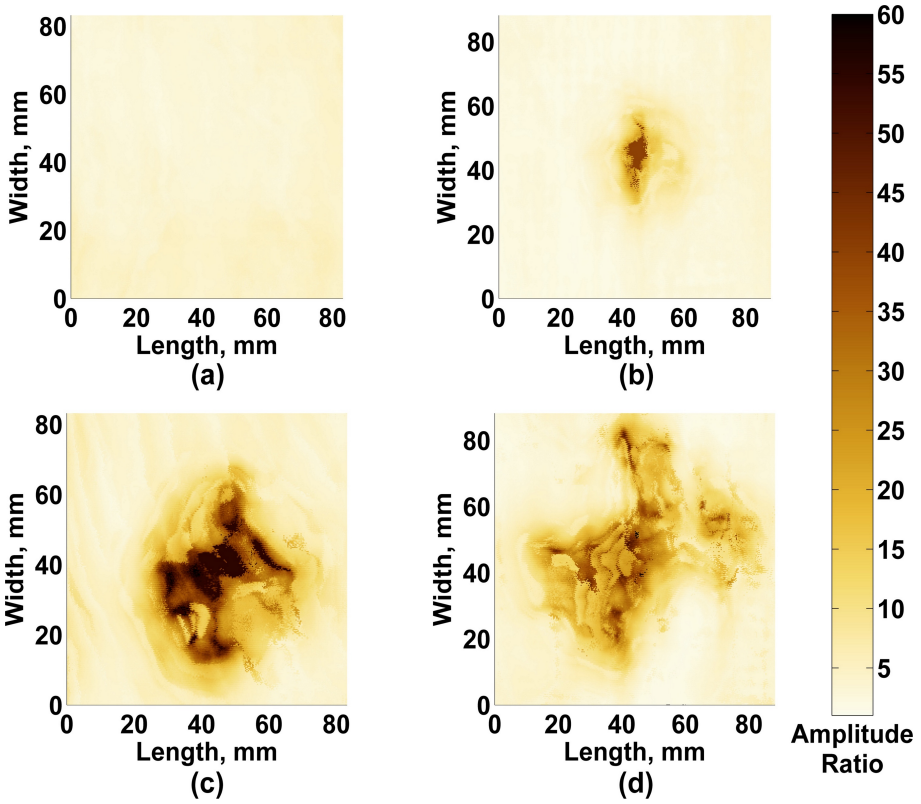

Figure 1.18: UT C-scans of GFRP samples showing the A_1^{UT}/A_2^{UT} ratio: (a) healthy GFRP sample; (b) damage from 20 J impact; (c) damage from 40 J impact; (d) damage from 80 J impact.

The best qualitative result was obtained for the GFRP sample with the largest damage introduced by the 80 J impact. As seen from the Fig. 1.20d, the ToF difference lies in the range of 3.2-3.6 μs for the pristine regions of the sample. The respective ToFs in the regions with delaminations reduced to approximately 2.5 and 2.0 μs depending on the depth at which the interlaminar defects were located in the cross-section. Clearly, the delaminations that occurred closer to the top surface resulted in a smaller ToF difference. In the case of 20 or 40 J impacts the damage was more concentrated in the center of the samples. In some of these regions, only the reflections from the top surface were present in the A-scans, and the amplitude of reflections from defects diminished to the noise level. As a result, the ToF difference could not be automatically identified, and the respective pixels of the UT C-scans were highlighted with a white color (see Fig. 1.20b and Fig. 1.20c). Nevertheless, these image segments were treated as structural damage in the contour plots after thresholding as shown in Fig. 1.21.

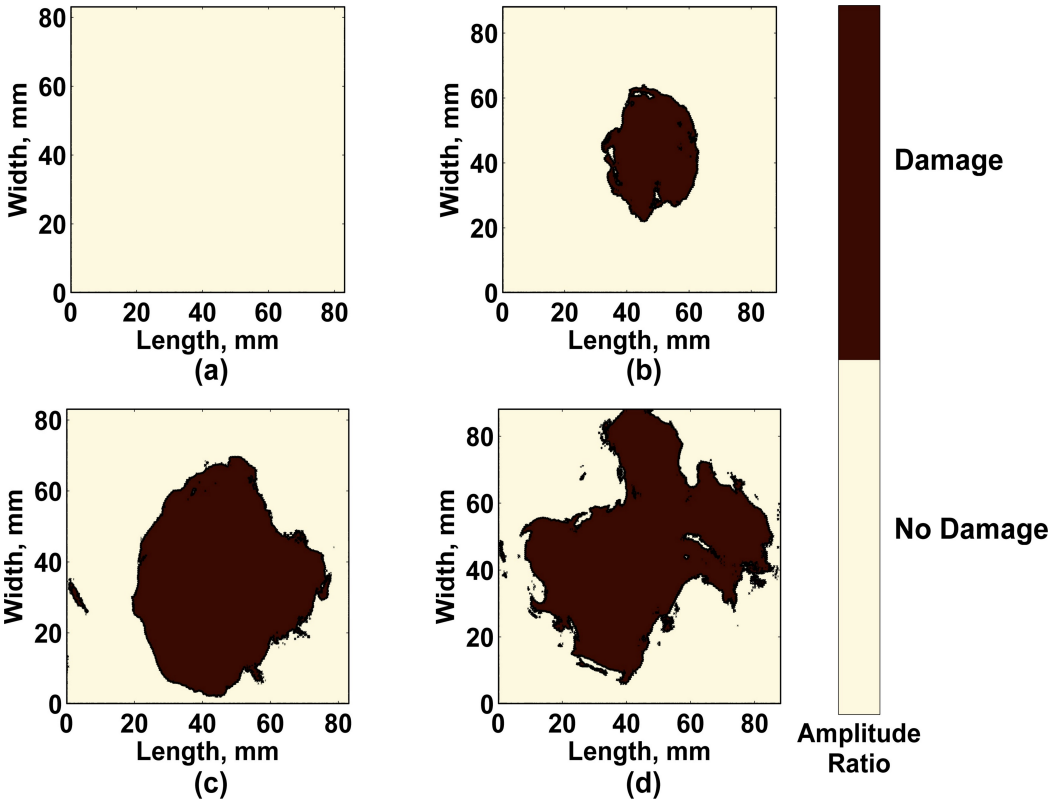

Figure 1.19: Damage contours identified from UT scans using A_1^{UT}/A_2^{UT} UT ratio: (a) healthy GFRP sample; (b) damage from 20 J impact; (c) damage from 40 J impact; (d) damage from 80 J impact.

The amplitude and ToF measurements were combined together in order to provide the most accurate estimation of the total extent of the impact damage. Since the UT C-scans in Fig. 1.18 and Fig. 1.20 shared the same coordinate grid, the binary union of damage contours could be easily computed. The final results are demonstrated in Fig. 1.22, and were used as a reference for comparison with other NDE techniques. As seen from the same figure, most of the information about the damage was obtained from the amplitude data for $E = 20$ J and $E = 40$ J impacts, while the ToF revealed a larger damage extent for $E = 80$ J impact.

1.2.3 Comparative analysis of pulse-echo UT and OTS measurements

Even though the natures of ultrasonic and optical NDE techniques seem quite different at the first glance, they share many similarities, and it is of a great interest to compare the obtained

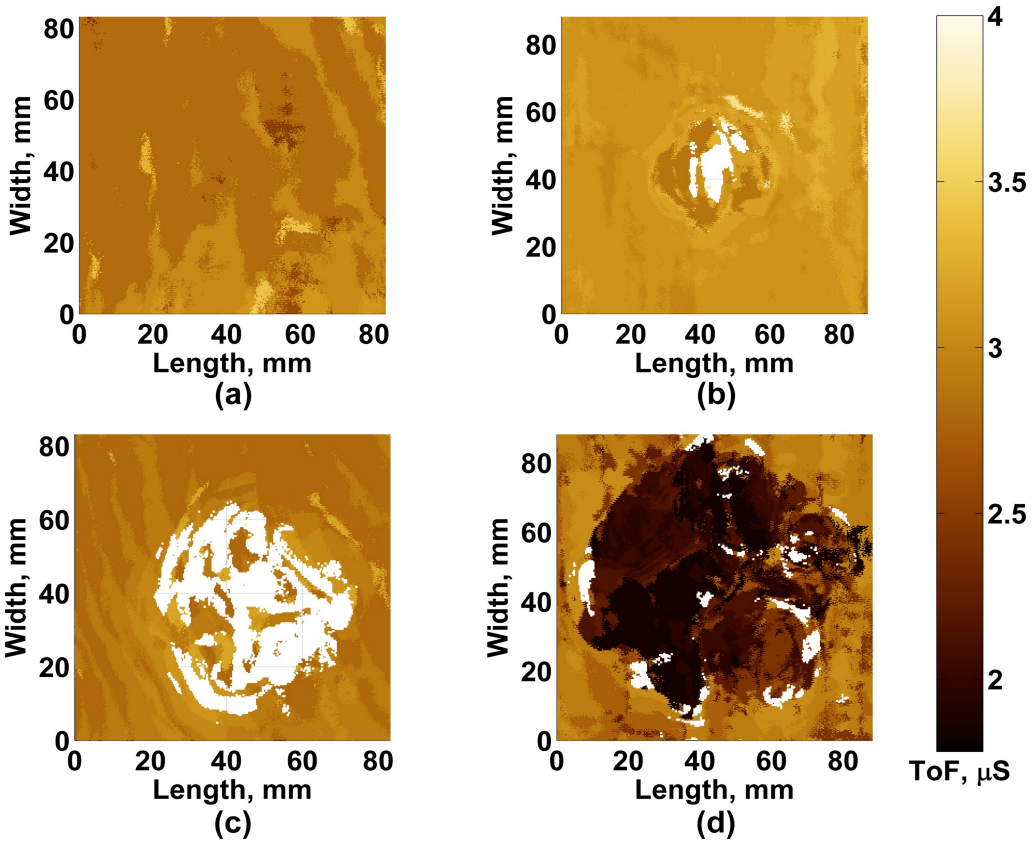

Figure 1.20: UT C-scans of GFRP samples showing the ToF difference between A_1^{UT} and A_2^{UT}: (a) healthy GFRP sample; (b) damage from 20 J impact; (c) damage from 40 J impact; (d) damage from 80 J impact.

results qualitatively for further experimental validation of the OTS system. The self-referencing capabilities of pulse-echo UT and OTS can be exploited to normalize the scans of impact damage and compare the results using a common metric. The process of acquiring UT and OT measurements is schematically shown in Fig. 1.23. The amplitude of a plane longitudinal UT wave reflected from the top surface of the GFRP specimen can be expressed using Beer-Lambert law [40]:

$$A_1^{UT} = A_0^{UT} \cdot R_{WC} \cdot e^{-2 \cdot \kappa_W \cdot 2 \cdot \chi_W}, \tag{1.16}$$

where A_0^{UT} is the acoustic wave intensity generated by the piezoelectric transducer; R_{WC} is the reflection coefficient of water-composite interface; κ_W is the attenuation constant for ultrasound in water; and $2 \cdot \chi_W$ is the total wave path in the water that includes forward and backward wave propagation equaling double the distance from the transducer to the sample. Note that Eq. (1.16) does not account for losses associated with the spread of the ultrasonic beam.

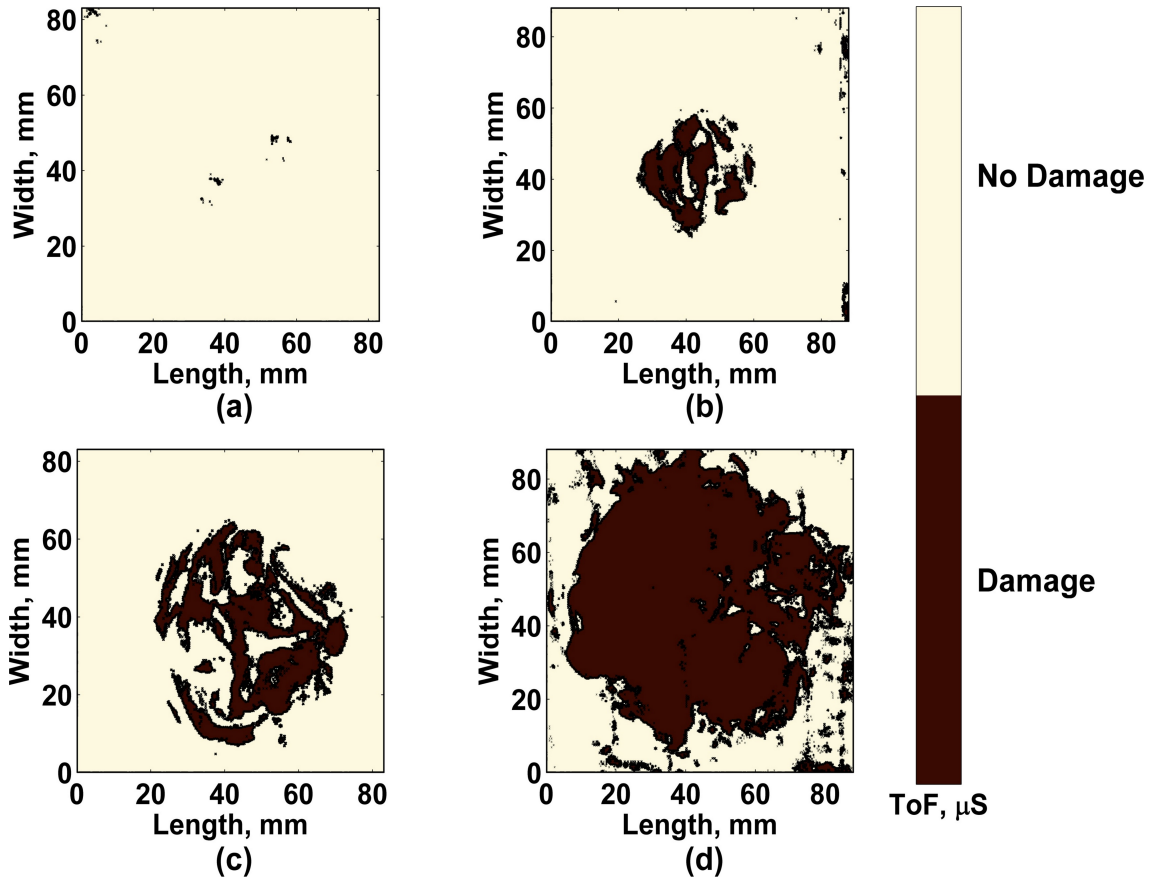

Figure 1.21: Damage contours identified using the UT ToF difference: (a) healthy GFRP sample; (b) damage from 20 J impact; (c) damage from 40 J impact; (d) damage from 80 J impact.

A portion of the ultrasonic wave energy propagates through the GFRP specimen, reflects from its bottom surface and leaks back into water. Assuming some energy losses occur in the bulk GFRP material, the amplitude of back wall reflection from a healthy sample sensed by the piezoelectric transducer is defined as:

$$\left(A_2^{UT}\right)_H = A_0^{UT} \cdot T_{WC} \cdot R_{WC} \cdot T_{CW} \cdot e^{-2\cdot\kappa_W\cdot 2\cdot\chi_W} \cdot e^{-2\cdot\kappa_C\cdot 2\cdot\chi_C}, \tag{1.17}$$

where T_{WC} is the transmission coefficient of the water-composite interface; $R_{CW} = 1 - T_{CW}$ and $T_{CW} = 1 - R_{CW}$ are the reflection and transmission coefficients of the composite-water interface, respectively; κ_C is the attenuation constant for ultrasound in the GFRP material; and $2 \cdot \chi_C$ is the total path travelled by the UT wave in the GFRP specimen that equals the doubled thickness of the specimen.

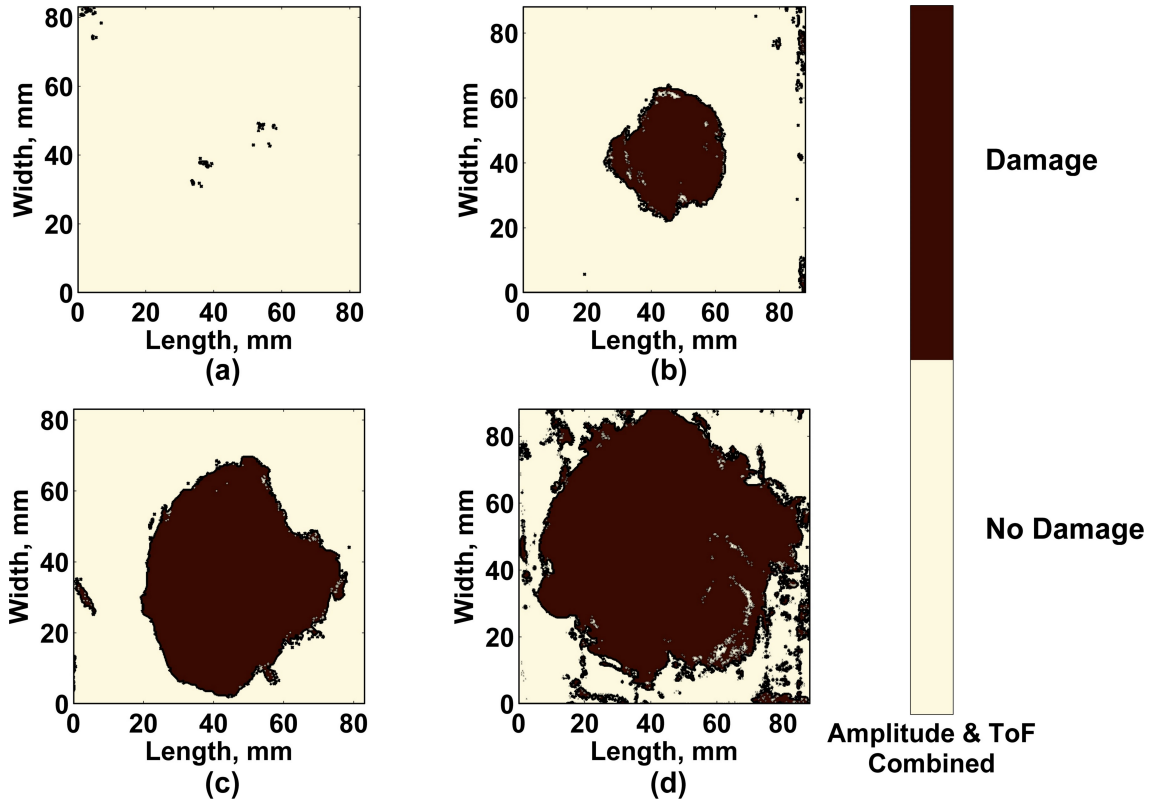

Figure 1.22: Binary union of damage contours estimated from the amplitude and ToF UT measurements: (a) healthy GFRP sample; (b) damage from 20 J impact; (c) damage from 40 J impact; (d) damage from 80 J impact.

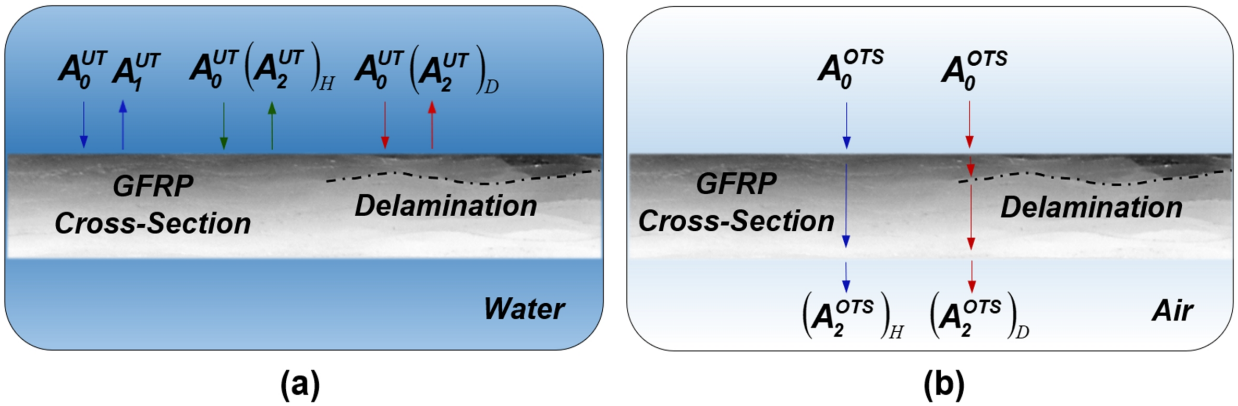

Figure 1.23: (a) Ultrasonic reflections from the top surface of the sample and from interlaminar delaminations in case of immersion UT inspection in pulse-echo mode; (b) transmission of electromagnetic radiation through healthy and delaminated regions of the test sample in case of OTS inspection.

Similarly, whenever the UT wave is incident onto a region of the sample with delaminations, the amplitude of the received back wall reflection can be expressed as:

$$\left(A_2^{UT}\right)_D = A_0^{UT} \cdot T_{WC} \cdot R_{WC} \cdot T_{CW} \cdot \left(1 - R_D^{UT}\right)^{2N} \cdot e^{-2\cdot\kappa_W\cdot 2\cdot\chi_W} \cdot e^{-2\cdot\kappa_C\cdot 2\cdot\chi_C}, \tag{1.18}$$

where R_D^{UT} is the reflection coefficient of a single delamination that accounts for both its top and bottom interfaces, and N is the number of delaminations at a scanning point. It is worth mentioning that it can be sometimes difficult to extract the amplitude of the back wall reflection by the time gating, since the observed wave packet has small amplitude and also contains contributions from reflections at the upper delaminations. The reflection coefficient of each delamination also depends on whether the interlaminar interface is filled with water or air. For instance, for a composite-water interface, the ratio between the incident and reflected UT intensities is defined by the Fresnel law [40]:

$$R_{CW} = \frac{I_{REF}}{I_{INC}} = \left(\frac{Z_W - Z_C}{Z_W + Z_C}\right)^2 \approx 0.36, \tag{1.19}$$

where I_{INC} and I_{REF} are the intensities of incident and reflected UT waves; Z_W and Z_C are the acoustic impedances of air and GFRP composite. The acoustic impedance of the GFRP material used in the impact tests was estimated experimentally by measuring its density ρ_C and velocity of longitudinal wave propagation ϑ_C and using the well-known approximation:

$$Z_C = \rho_C \cdot \vartheta_C = 1900 \cdot 3100 = 5.89 \times 10^6 \left[kg/\left(m \cdot s^2\right)\right]. \tag{1.20}$$

Similarly, for water and air we have:

$$Z_W = \rho_W \cdot \vartheta_W = 1000 \cdot 1480 = 1.49 \times 10^6 \left[kg/\left(m \cdot s^2\right)\right], \tag{1.21}$$

$$Z_A = \rho_A \cdot \vartheta_A = 1.225 \cdot 343 = 420.18 \left[kg/\left(m \cdot s^2\right)\right]. \tag{1.22}$$

Consequently, the reflection coefficient of a composite-air interface is:

$$R_{CA} = \left(\frac{Z_A - Z_C}{Z_A + Z_C}\right)^2 \approx 1. \tag{1.23}$$

Hence, if a delamination is filled with air, very little UT wave intensity propagates through the interface owing to the large acoustic impedance mismatch, and the bottom layer delaminations or back wall reflection may not be detected. However, this is not the case with optical transmission scanning, as the experimental results demonstrate. Considering the top and back wall UT reflections, the optical amplitude attenuation coefficient for a healthy composite sample can be defined as:

$$\alpha_H^{UT} = \left(\frac{A_2^{UT}}{A_1^{UT}}\right)_H = \frac{A_0^{UT} \cdot T_{WC} \cdot R_{CW} \cdot T_{CW} \cdot e^{-2\cdot\kappa_W\cdot 2\cdot\chi_W} \cdot e^{-2\cdot\kappa_C\cdot 2\cdot\chi_C}}{A_0^{UT} \cdot R_{WC} \cdot e^{-2\cdot\kappa_W\cdot 2\cdot\chi_W}}$$
$$= \frac{T_{WC} \cdot (1 - T_{CW}) \cdot T_{CW} \cdot e^{-2\cdot\kappa_C\cdot 2\cdot\chi_C}}{1 - T_{WC}} \quad (1.24)$$

Similarly, for the case with delaminations, we have:

$$\alpha_D^{UT} = \left(\frac{A_2^{UT}}{A_1^{UT}}\right)_D = \frac{T_{WC} \cdot (1 - T_{CW}) \cdot T_{CW} \cdot \left(1 - R_D^{UT}\right)^{2N} \cdot e^{-2\cdot\kappa_C\cdot 2\cdot\chi_C}}{1 - T_{WC}}, \quad (1.25)$$

where R_D^{UT} is the reflection coefficient for a single delamination taking into account losses at both interfaces. The procedure for comparing the UT and OTS measurements adopted in this paper included normalization of all UT amplitude ratios with respect to those obtained on the healthy region of the test sample, such that the attenuation inside the healthy composite is compensated and only the attenuation introduced by the impact damage is obtained:

$$\tilde{\alpha}^{UT} = \frac{\alpha_D^{UT}}{\alpha_H^{UT}} = \left(1 - R_D^{UT}\right)^{2N} \quad (1.26)$$

In the case of OTS, the amplitude of radiation power transmitted through a healthy GFRP can be calculated as:

$$\left(A_2^{OTS}\right)_H = A_0^{OTS} \cdot T_{AC} \cdot T_{CA} \cdot e^{-\eta_C\cdot\chi_C}, \quad (1.27)$$

where A_0^{OTS} is the output power of the radiation source, T_{AC} is the transmission coefficient of an air-composite interface, T_{CA} is the transmission coefficient of a composite-air interface, η_C is the attenuation constant for electromagnetic radiation in the GFRP material, and χ_C is the thickness of the GFRP specimen.

The corresponding expression for the case of the GFRP with delaminations takes the following form:

$$\left(A_2^{OTS}\right)_D = A_0^{OTS} \cdot T_{AC} \cdot T_{CA} \cdot \left(1 - R_D^{OTS}\right)^N \cdot e^{-\eta_c \cdot \chi_c}, \tag{1.28}$$

where $R_D^{OTS} = R_1 = R_2 = \cdots = R_N$ is the reflection coefficient of a single delamination taking into account losses at both interfaces, and N is the total number of delaminations. Hence, the OTS attenuation constants of healthy GFRP and GFRP with delaminations are defined as:

$$\alpha_H^{OTS} = \left(\frac{A_2^{OTS}}{A_0^{OTS}}\right)_H = \frac{A_0^{OTS} \cdot T_{AC} \cdot T_{CA} \cdot e^{-\eta_c \cdot \chi_c}}{A_0^{OTS}}, \tag{1.29}$$

$$\begin{aligned} \alpha_D^{OTS} = \left(\frac{A_2^{OTS}}{A_0^{OTS}}\right)_D &= \frac{A_0^{OTS} \cdot T_{AC} \cdot T_{CA} \cdot \left(1 - R_D^{OTS}\right)^N \cdot e^{-\eta_c \cdot \chi_c}}{A_0^{OTS}} \\ &= T_{AC} \cdot T_{CA} \cdot \left(1 - R_D^{OTS}\right)^N \cdot e^{-\eta_c \cdot \chi_c} \end{aligned} \tag{1.30}$$

If the OTS self-referencing capability is used, all power measurements at the photodetector should be normalized by the corresponding values obtained on the healthy regions of the composite sample, as follows:

$$\tilde{\alpha}^{OTS} = \frac{\alpha_D^{OTS}}{\alpha_H^{OTS}} = \frac{\left(A_2^{OTS}\right)_D}{\left(A_2^{OTS}\right)_H} = \left(1 - R_D^{OTS}\right)^N \tag{1.31}$$

As mentioned above, post-processing of OT-scans relies on the key assumption that the reflection coefficients of all delaminations are reasonably close to identical. The transmission coefficient of a single delamination, was obtained experimentally from OT-scans of a mode I sample:

$$T_D^{OTS} = 1 - R_D^{OTS} \approx 0.61 \tag{1.32}$$

In the case of UT, on the other hand, the transmission coefficient of a single delamination filled with water can be estimated as

$$T_D^{UT} = 1 - R_D^{UT} = \left(1 - R_{CW}\right) \cdot \left(1 - R_{WC}\right) \approx \left(1 - R_{CW}\right)^2 \approx 0.41 \tag{1.33}$$

Consideration of the amplitude attenuations defined by Eq. (1.26) and Eq. (1.31) suggests that the UT and OT scans can be compared qualitatively through the following relationship:

$$\frac{ln\left(\tilde{\alpha}^{UT}\right)}{ln\left(\tilde{\alpha}^{OTS}\right)} = \frac{ln\left[\left(1-R_D^{UT}\right)^{2N}\right]}{ln\left[\left(1-R_D^{OTS}\right)^{N}\right]} = 2\cdot\frac{ln\left(1-R_D^{UT}\right)}{ln\left(1-R_D^{OTS}\right)} \tag{1.34}$$

$$\tilde{\alpha}^{UT} = \left(\tilde{\alpha}^{OTS}\right)^{2\cdot\frac{ln\left(1-R_D^{UT}\right)}{ln\left(1-R_D^{OTS}\right)}} \tag{1.35}$$

However, it should be noted that Eq. (1.35) is only an approximation. It does not account for such factors as different footprints and divergences of the ultrasonic and laser beams as well as some challenges in extracting correct amplitudes from the ultrasonic A scans. Fig. 1.24 and Fig. 1.25 show the post-processed images of structural damage obtained with the UT and OTS techniques.

These normalized versions of the scans demonstrate good agreement for all impact energies. In particular, the outer damage contours are quite similar; and the slight variations of damage severity can be attributed to the challenges in UT data processing described earlier. The obtained results additionally validate the OTS technique and prove its worthiness for NDE of GFRP composites. Compared to water immersion pulse-echo UT, the OTS is fully non-contact, and it offers rapid scanning capabilities, because the photodetector generates a DC voltage output that is directly proportional to transmitted radiation. UT, on the other hand, requires sampling and post-processing of the entire ultrasonic waveform (A-scan) record.

1.2.3.1 UV DPT of impacted GFRP samples

The results of the UV DPT are shown in Fig. 1.26. As seen from the images, the damage patterns on the top surface exhibited a cruciate form, which followed the directions of the glass fibers in the samples, $[0/90]_4$. On the other hand, damage on the bottom side of the samples was distributed quasi-uniformly in the circumferential direction. Because the position of the UV

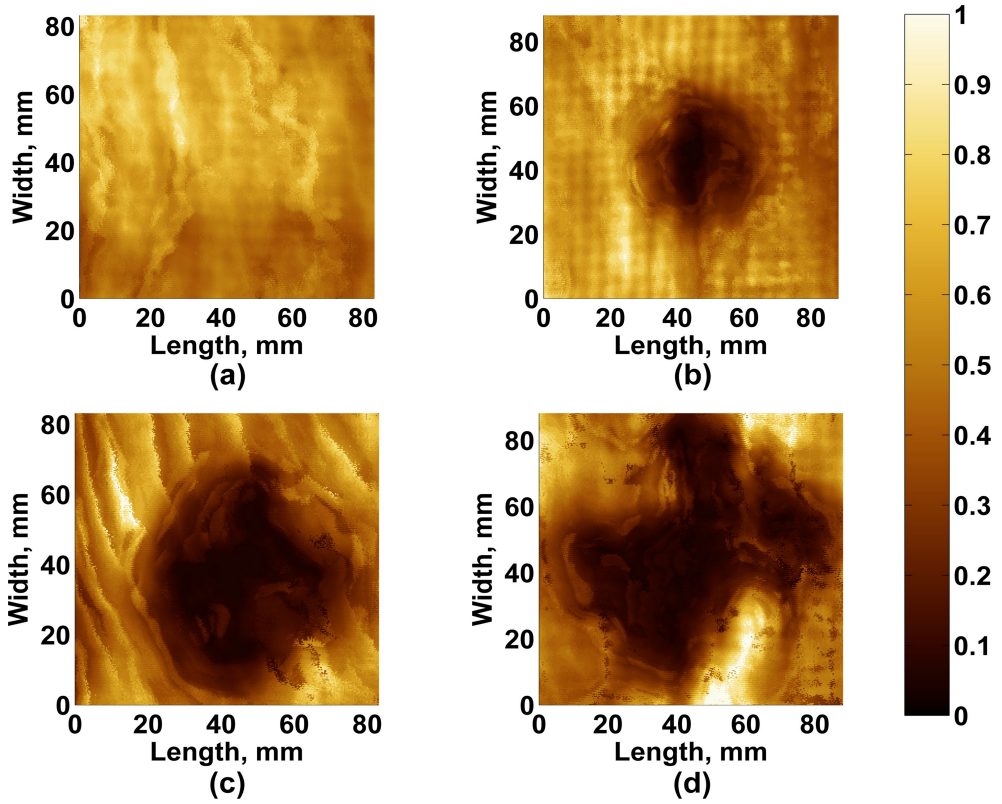

Figure 1.24: Normalized UT C-scans showing $\tilde{\alpha}^{UT}$ for: (a) healthy GFRP sample; (b) GFRP sample subjected to 20 J impact; (c) GFRP sample subjected to 40 J impact; (d) GFRP sample subjected to 80 J impact.

lamp varied during the tests, the digital images had slightly different brightness levels. Therefore, the post-processing of the results included their normalization by the maximal image intensity, as shown in Fig. 1.27. Damage contours were then obtained by image thresholding. The threshold level was estimated from the averaged intensity measured in the healthy regions of all samples, and was applied to all images. The damage distributions determined from the top and bottom surfaces of the test specimens are shown in Fig. 1.28.

The total damage extent was identified in each case by combining the damage contours for both the top and bottom surfaces for each sample. Note that in all the figures showing the UV DPT results, all bottom side images were mirrored along the vertical axis. Fig. 1.29 demonstrates that adding the rear side images mostly increased the damage area between the principle fiber directions. The total damage extent can be estimated from each combined figure by considering the union of yellow and dark brown contours.

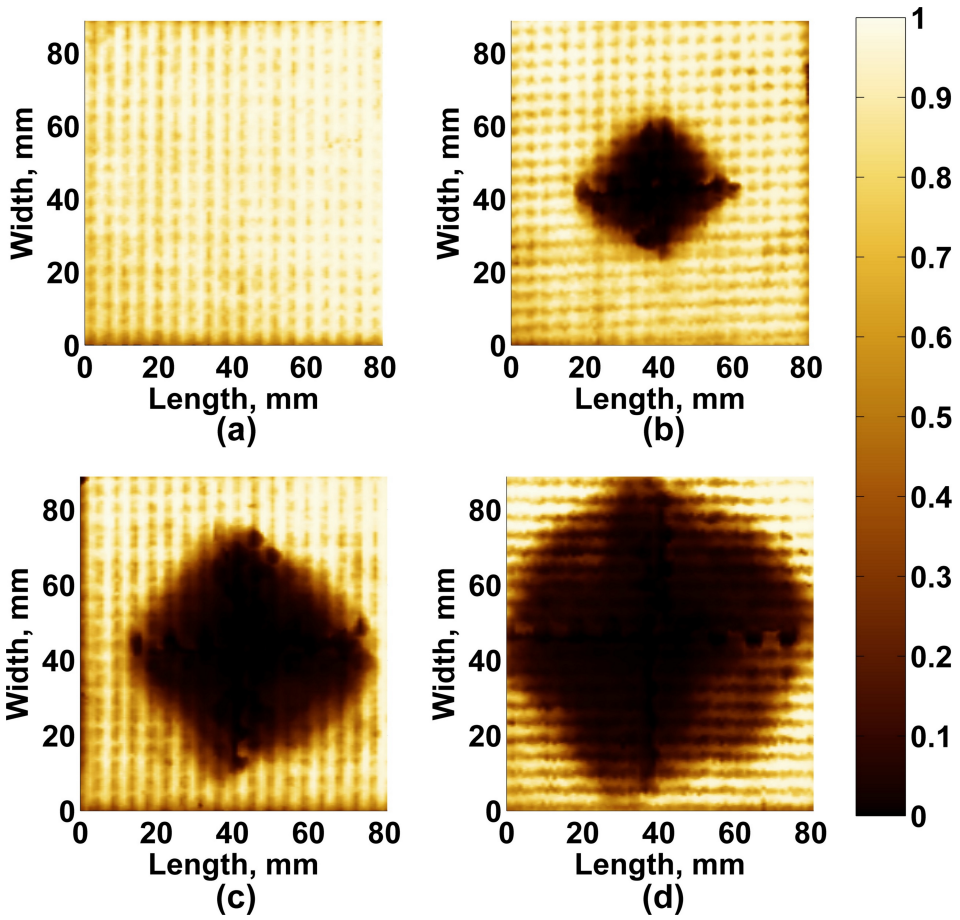

Figure 1.25: Normalized OT-scans adjusted according to Eq. (1.35) that show $\left(\tilde{\alpha}^{OTS}\right)^{2\cdot\frac{ln\left(1-R_D^{UT}\right)}{ln\left(1-R_D^{OTS}\right)}}$ for: (a) healthy GFRP sample; (b) GFRP sample subjected to 20 J impact; (c) GFRP sample subjected to 40 J impact; (d) GFRP sample subjected to 80 J impact.

1.2.3.2 Quantitative comparison of OTS and other NDE methods in estimation of the total damage area

The extent of the impact damage was independently estimated for all GFRP specimens by the OTS, UT and UV DPT, as described in the previous sections. The summary of results shown in Fig. 1.30 demonstrates good overall agreement for all three of these NDE techniques. In particular, the percent difference in estimation of the total damage area between the OTS and other techniques was generally small, as shown in Table 1.2. The largest relative difference was observed for all techniques in the case of the impact with the smallest energy of 20 J. In the case of OTS and UT,

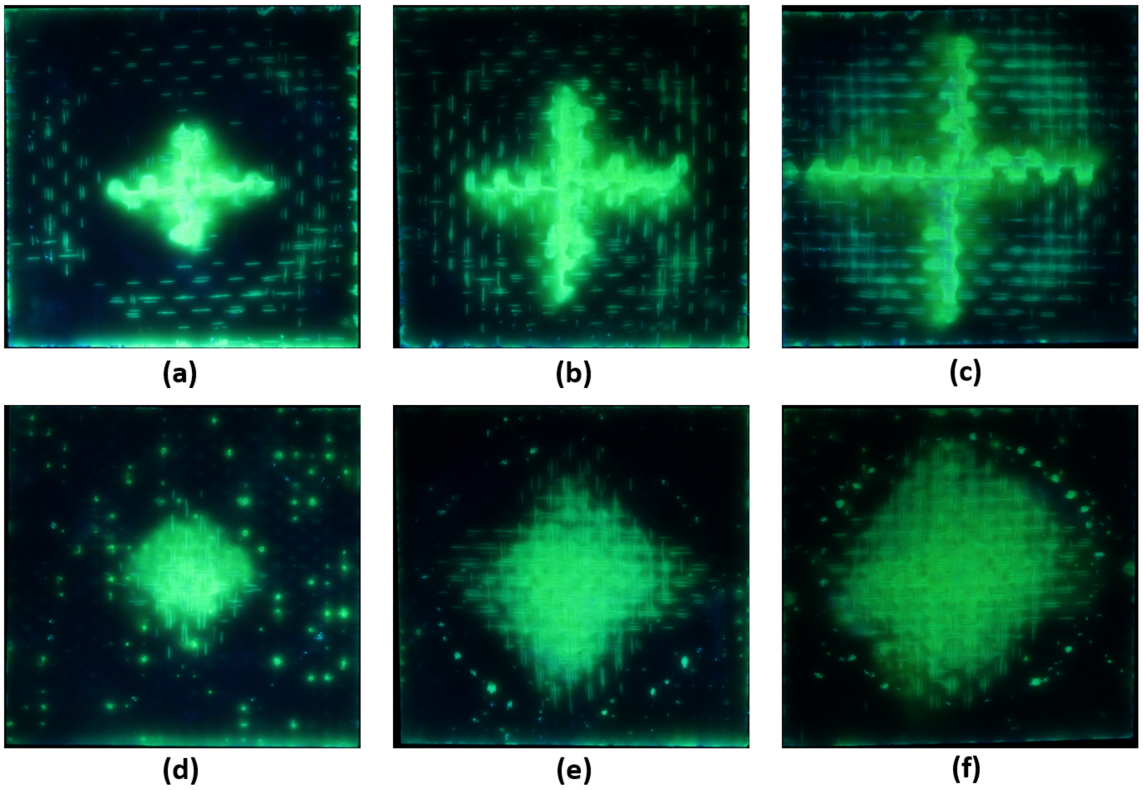

Figure 1.26: Images of damaged GFRP samples soaked in UV dye and illuminated with UV light: (a) top surface, $E = 20\ J$; (b) top surface, $E = 40\ J$; (c) top surface, $E = 80\ J$; (d) bottom surface, $E = 20\ J$; (e) bottom surface, $E = 40\ J$; (f) bottom surface, $E = 80\ J$.

Technique	$E = 20\ J$	$E = 40\ J$	$E = 80\ J$
UT	14.89%	1.51%	8.76%
UV DPT	19.70%	2.43%	2.13%

Table 1.2: Absolute percent difference in estimation of the total damage area between the OTS and other NDE techniques.

this can be attributed to the differing footprints of the ultrasonic and laser beams, which resulted in different averaging areas and transition regions. Hence, the edge smoothing introduced by the finite beam width had more effect on the smallest damage and was less pronounced for bigger damage, as expected. Some discrepancies in estimation of the overall damage extent between the OTS and UV DPT were apparently caused by excessive dye penetrant, which was not completely removed by surface cleaning. At the same time, there is also a possibility that the UV dye did not penetrate into all internal defects.

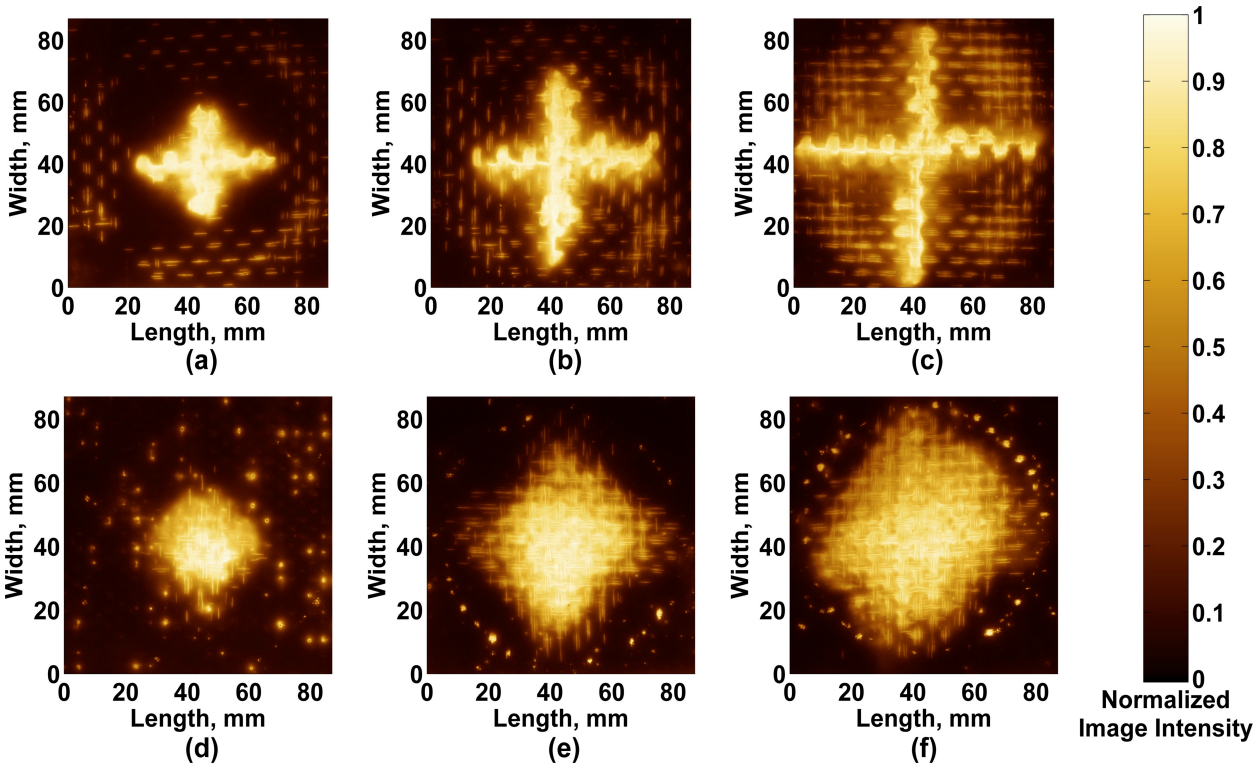

Figure 1.27: UV DPT images of damaged GFRP samples after normalization of image intensity: (a) top surface, $E = 20\ J$; (b) top surface, $E = 40\ J$; (c) top surface, $E = 80\ J$; (d) bottom surface, $E = 20\ J$; (e) bottom surface, $E = 40\ J$; (f) bottom surface, $E = 80\ J$.

1.2.4 Conclusions

In this Section, OTS was successfully validated by comparing inspection results with two conventional NDE techniques, including pulse-echo UT and UV DPT. The damage extent was determined for GFRP samples after low velocity impacts at three different energies of 20, 40 and 80 J. The experimental results demonstrated good agreement for OTS, UT, and UV DPT. OTS and conventional water immersion pulse-echo UT provided similar evaluations of the severity of damage inside the GFRP samples. In addition, post-processing of OT-scans helped to better quantify impact damage by determining the total number of delaminations at each scan position. The damage areas corresponding to either one or two delaminations were found to increase dramatically for higher impact energy, but there was no significant difference in damage areas when delaminations were more numerous.

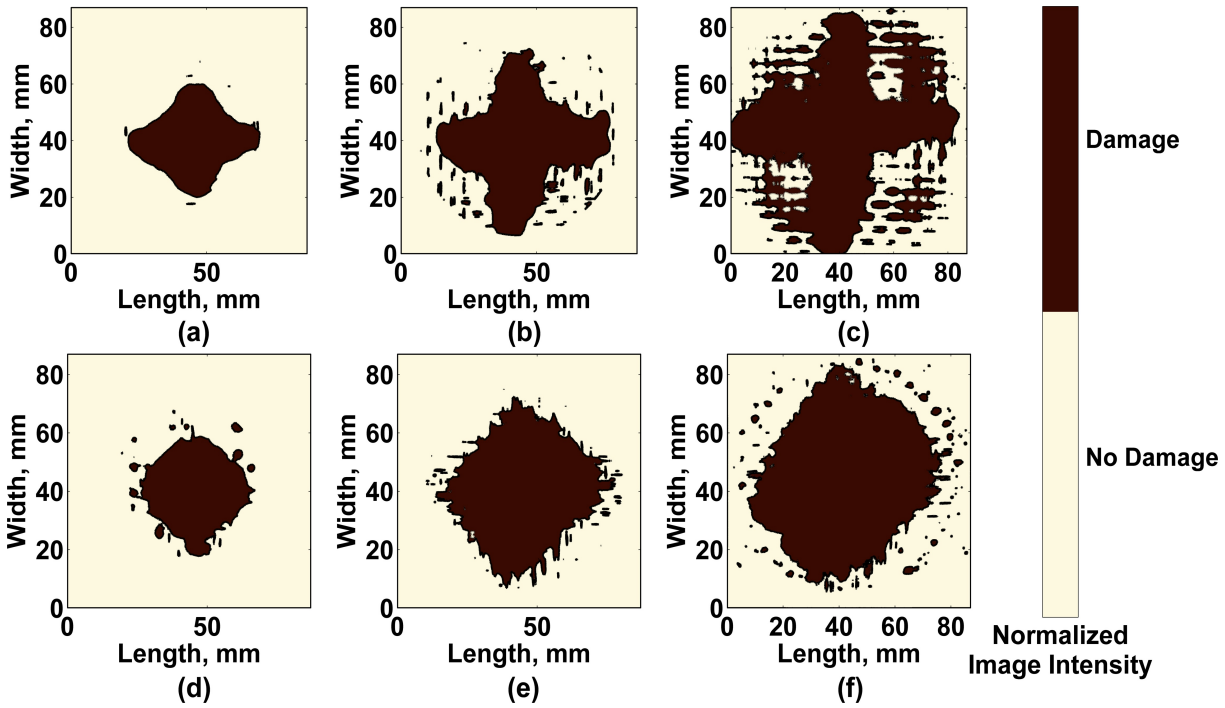

Figure 1.28: Damage contours identified from normalized UV DPT images of GFRP samples: (a) top surface, $E = 20\ J$; (b) top surface, $E = 40\ J$; (c) top surface, $E = 80\ J$; (d) bottom surface, $E = 20\ J$; (e) bottom surface, $E = 40\ J$; (f) bottom surface, $E = 80\ J$.

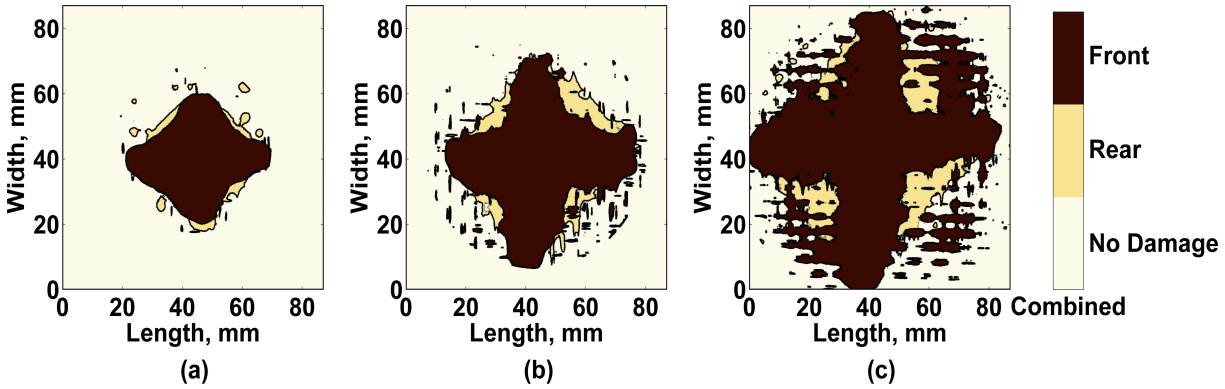

Figure 1.29: Total damage area evaluated as a union of UV DPT images taken from top and bottom sides of GFRP samples: (a) $E = 20\ J$; (b) $E = 40\ J$; (c) $E = 80\ J$.

It was demonstrated that OTS combines cost-effectiveness and the fast NDE capabilities of qualitative techniques (e.g., UV DPT) with the more robust and comprehensive data analysis provided by quantitative methods (e.g., UT). Overall, the results obtained with the developed OTS system are promising and encouraging.

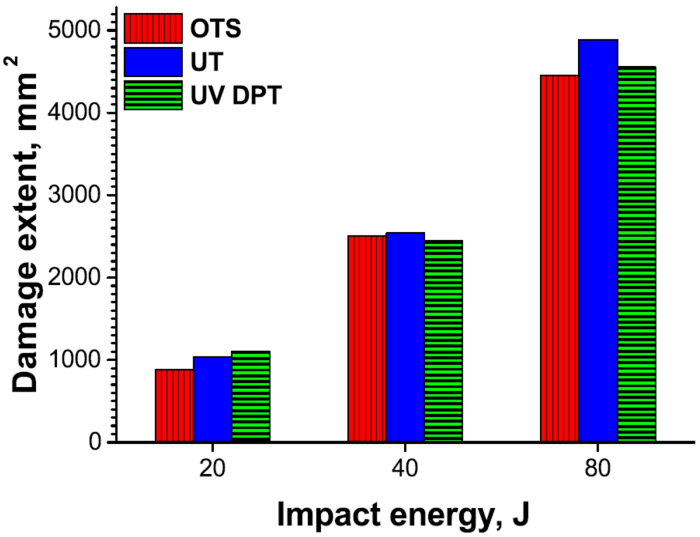

Figure 1.30: Comparison of damage areas obtained by the OTS, UT, and UV DPT for different impact energy levels.

1.3 Feasibility of OTS for Quality Control and NDE of GFRP Composite Structures

Results presented in this Section demonstrate that defects and certain microstructural variations in GFRP composites can be easily identified by OTS, because the technique is sensitive to localized changes of optical properties such as radiation absorption and scattering. The applications of OTS are extended to GFRP plates with improperly mixed resin, inclusions, and delaminations. We also demonstrate the capability of the technique to evaluate the distribution of adhesive and detect fatigue damage in adhesively bonded GFRP joints.

1.3.1 Materials and methods

1.3.1.1 Manufacturing of GFRP samples with improper cured resin component proportions

An eight layer GFRP plate was manufactured using the previously described resin transfer molding (RTM) process. However, in this case some regions of the plate had improper ratios of part A and part B of the epoxy, which resulted in non-uniform matrix properties. On one edge of the specimen, the component ratio was nearly optimal, and on the opposite edge the epoxy lacked

the hardener. Hence, the epoxy component proportions in the middle of the plate fell somewhere between the values at the opposite edges, with an unknown gradiation over the extent of the plate that depended on the local degree of mixing. The standard cure cycle was implemented, which likely left only partially cured those areas where the hardener proportion was below optimal. Three rectangular samples (100×50×4.7 *mm*) were cut from the left, middle and the right areas of the plate, and then were labeled as "properly mixed", "semi-mixed" and "badly mixed", correspondingly (see Fig. 1.34).

1.3.1.2 Manufacturing of GFRP samples with inclusions

The plate manufacturing process was implemented twice to allow two different types of inclusions in the composite specimens. In the first sample (100×100×4.7 *mm*), small pieces of resin transfer medium were intentionally left between plies during the manufacturing. The average size of such objects was about a few millimeters. The inclusions were of a red color as shown in Fig. 1.32a. In the second GFRP plate (360×85×4.7 *mm*) foreign objects were simulated as glass fibers dyed black (Fig. 1.33a). The sample also had piezoelectric wafer elements bonded to its top surface for exciting ultrasonic guided waves, which was a part of another study for defect detection using guided waves [41, 42].

1.3.1.3 Manufacturing of double cantilever beam samples and mode I fracture tests

Mode I fracture tests were performed using double cantilever beam (DCB) samples in accordance with ASTM standard D5528. The samples were fabricated using the materials and procedures described in Section 1. A Teflon sheet was placed in the middle of the sample during layup to introduce the initial crack. The cured plates were cut to required dimensions and the piano hinges were attached using high-strength cyanoacrylate glue (see Fig. 1.35a).

1.3.1.4 Manufacturing of adhesively bonded GFRP joints and fatigue tests

Two 430×45 *mm* lap-joints with bond area lengths of 50 *mm* were manufactured from 4.7 *mm* thick quasi-isotropic GFRP composite plates bonded with FM-94K adhesive film as shown in Fig. 1.31. The thickness of the adhesive layer was intended to be 0.4 *mm* for both specimens. Prior to placing the lap-joints into the oven, the adherends of the first lap-joint were clamped together using stiff backing plates so as to establish quasi-uniform distribution of the adhesive. The adherends of the second lap-joint were clamped by a C-clamp in the center of the bond area, which allowed the plates to flex slightly so as to create a nonuniform adhesive thickness.

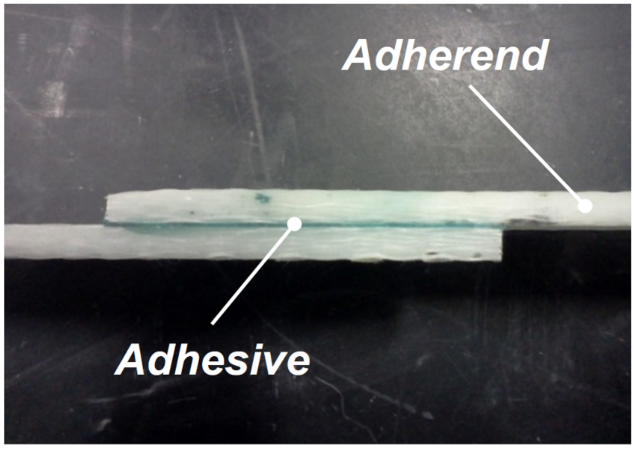

Figure 1.31: Side view of the manufactured GFRP lap-joint.

The sizes of the lap-joints did not meet the relevant ASTM standards, because the same lap-joints were used as waveguides for ultrasonic wave propagation in another study [26]. The second lap-joint was subjected to fatigue testing to introduce gradual failure of the adhesive at the edges of the bond area. Fatigue testing was performed at 30% of the ultimate tensile strength (UTS), and the rate of cyclic loading was set to 2 Hz. The UTS of the lap-joint was approximately 70 kN, this value being determined from prior tensile tests of similar specimens. The sinusoidal load was applied in tension to avoid buckling effects. The relative displacement between the two adherends was measured using appropriately placed laser reflectors and a laser extensometer. Fatigue testing was stopped at approximately 20000 cycles due to time considerations.

1.3.2 Experimental Results and Discussion

1.3.2.1 Detection of foreign object inclusions in GFRP plates

The GFRP plate with foreign object debris simulated as pieces of resin transfer media is shown in Fig. 1.32a, where the circles show the locations of the debris. The corresponding OT-scan demonstrated in Fig. 1.32b revealed that some areas of the plain weave GFRP plate with no inclusions had higher transmittance than other areas, which was caused by thickness variations of the sample and glass fiber irregularities. The transmitted power was minimal when radiation propagated via clusters of fibers. In contrast, the highest transmitted power corresponded to propagation of radiation via resin-rich areas.

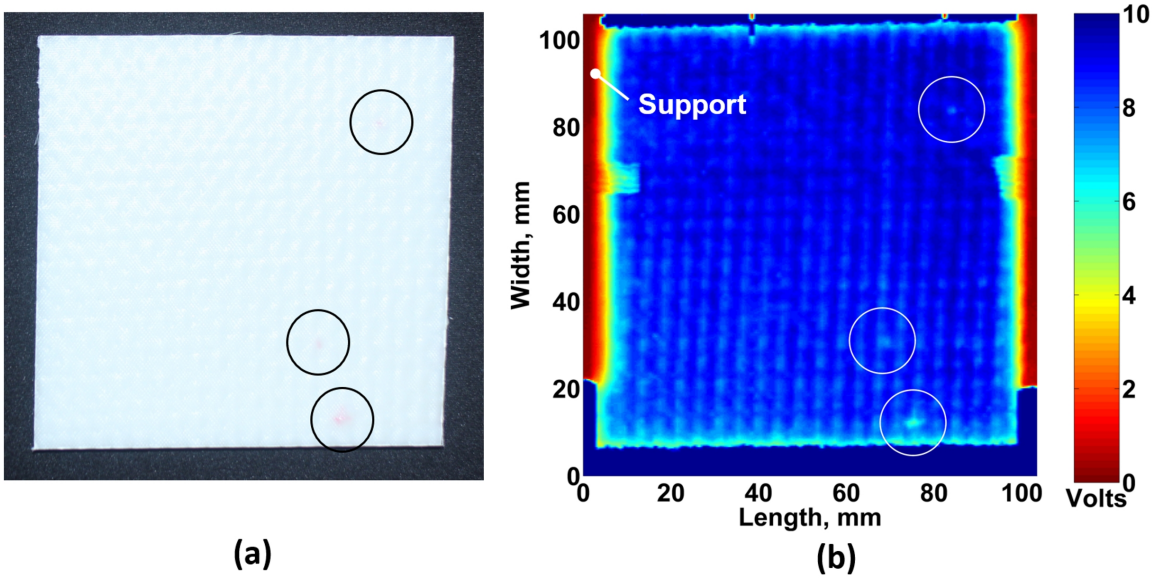

Figure 1.32: (a) GFRP sample with red inclusions (small pieces of resin transfer medium); (b) OT-scan of the same sample. Inclusions are highlighted by circles in both images.

The inclusions of resin transfer medium reduced the averaged transmitted power by 33%, which in some cases was comparable with the transmitted power reduction due to variations of the GFRP structure. As seen in Fig. 1.32a, the inclusions were of red color, which matched the wavelength of laser radiation. Hence, the sensitivity of OTS to red foreign objects was mainly determined by scattering at their interfaces rather than by radiation absorption of the material.

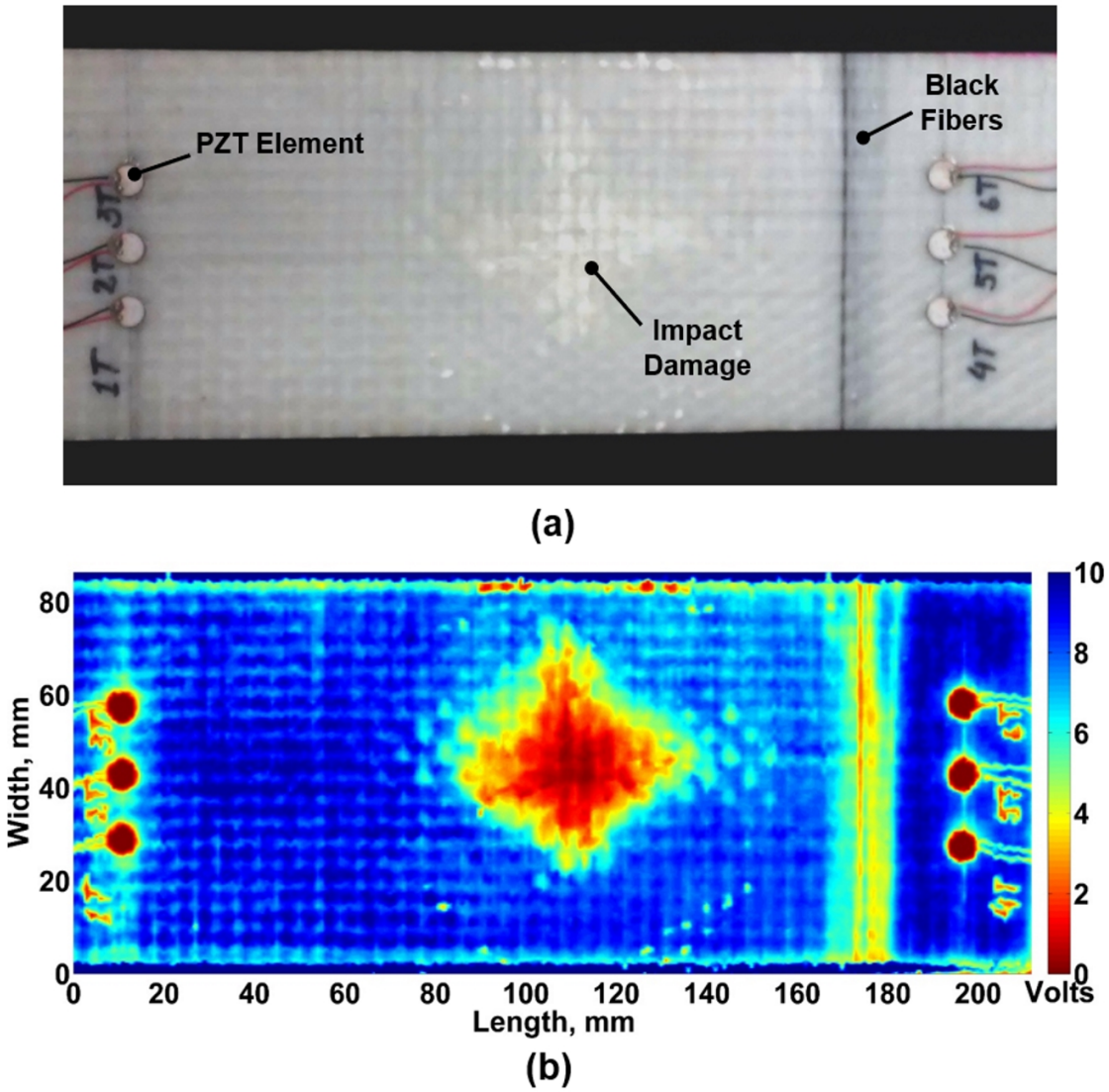

Figure 1.33: (a) 8-layer GFRP sample with black fiber inclusions and impact damage; (b) OT-scan of the same sample.

In contrast, OT-scans of the GFRP sample with black-dyed fibers showed that the transmitted radiation power at the receiver was reduced up to 80% compared to healthy GFRP structure (Fig. 1.33). In this case, inclusions of black fibers caused not only scattering, but significant absorption of laser radiation at 640 *nm* wavelength. These results demonstrate that an OTS system can be designed to characterize both the shapes and the materials of foreign objects if several scanning wavelengths are employed.

1.3.2.2 Evaluation of GFRP plates having improper proportions of matrix components

OTS was used to evaluate three GFRP specimens cut from a plate with local variations of part A to part B epoxy ratios, as explained in Section 1. Digital images of the top surfaces of the samples are presented in Fig. 1.34. The first sample, shown in Fig. 1.34a, was manufactured with a proper epoxy mixture, while the second and third samples lacked the hardener in smaller and larger amounts. To the eye, all three samples appear to be fabricated with the proper resin proportions. OT-scans of all

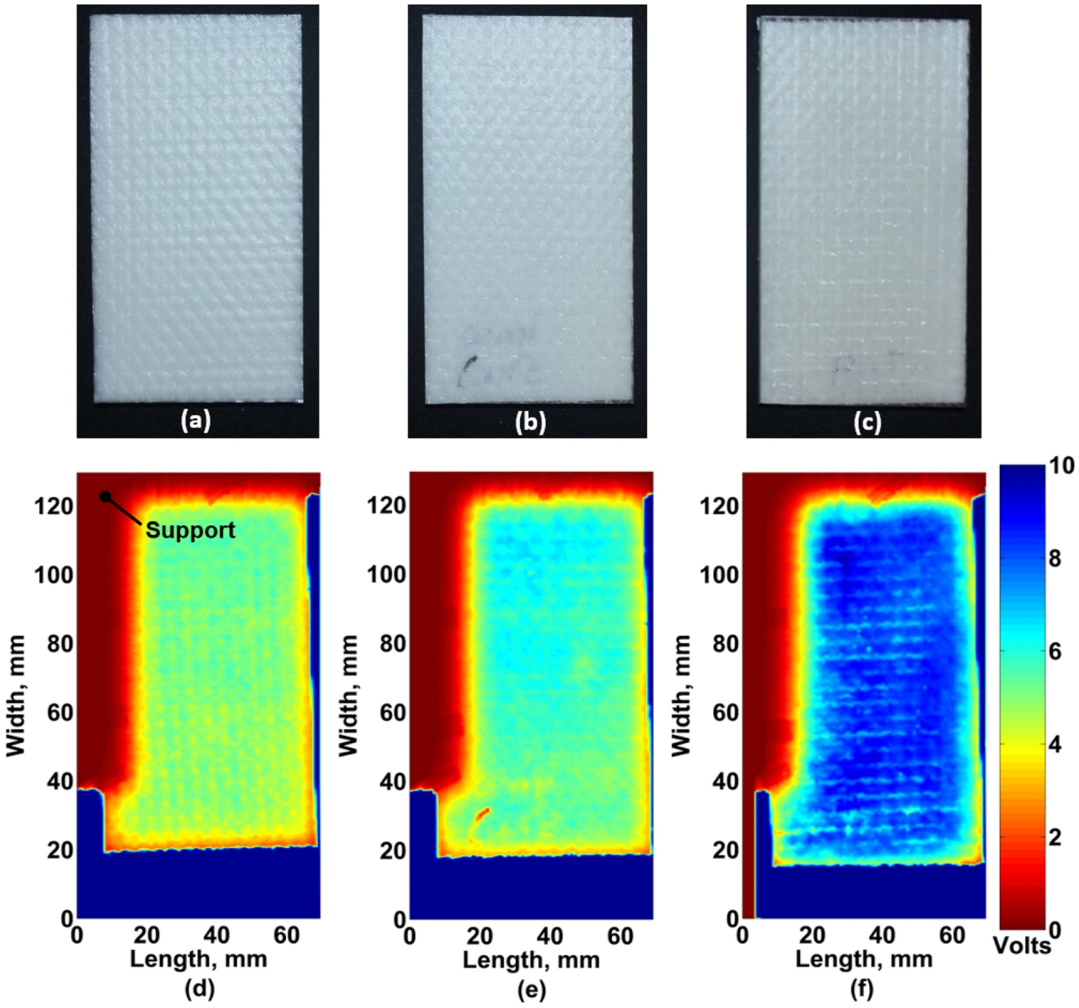

Figure 1.34: Evaluation of 8-layer GFRP samples and QC detection of faulty resin component ratios using OTS: (a) Photo of GFRP sample having proper resin proportions; (b) Photo of GFRP sample having moderate error in resin proportions; (c) Photo of GFRP sample having extreme error in resin proportions; (d) OT-scan GFRP sample having proper resin proportions; (e) OT-scan of GFRP sample having moderate error in resin proportion; (f) OT-scan of GFRP sample having extreme error in resin proportions.

three samples were acquired at the same laser power of 8 mW. The results obtained demonstrated that afaulty resin proportions affects the optical transmittance, although all three specimens looked quite similar visually. The voltage outputs from the photodetector averaged over sample areas with no supports were 5.02 V, 5.83 V and 8.13 V, respectively. Hence, the transmitted power increased by 16% for "semi-mixed" composite and by 62% for "improperly mixed" composite. In addition, the "semi-mixed" sample had non-uniform optical transmittance over the scan area (see Fig. 1.34e), apparently owing to the local variations of part A to part B component ratio. These results, while largely qualitative in nature, demonstrate that the OTS technique is promising for detection of improper proportioning or mixing of the matrix components in GFRP composites.

1.3.2.3 Monitoring of crack propagation in DCB samples

Accurate determination of crack length in DCB samples is critical for reliable estimation of fracture toughness of GFRP material. In this section, we demonstrate the suitability of OTS for crack imaging and characterization of interior interfaces in GFRP DCB samples. Typical OT-scans of DCB samples are presented in Fig. 1.35b and Fig. 1.35c.

Experimental results demonstrated that 15.4% of the radiation propagated through the Teflon insert embedded between the GFRP adherends. Subsequent to cyclic loading causing crack growth, the detailed crack profile was visible. The transmission coefficient of a tight crack,T, is around 0.6, apparently owing to the diffuse surface of the crack interface. The transmission coefficient is calculated as the ratio of the radiation intensities averaged over the healthy region of the sample to the intensities measured in the area of a crack (blue and orange regions in Fig. 1.35c, respectively). As demonstrated in Section 1, knowledge of T allows for successful characterization of impact damage and determination of the total number of delaminations in GFRP plates after low velocity impacts.

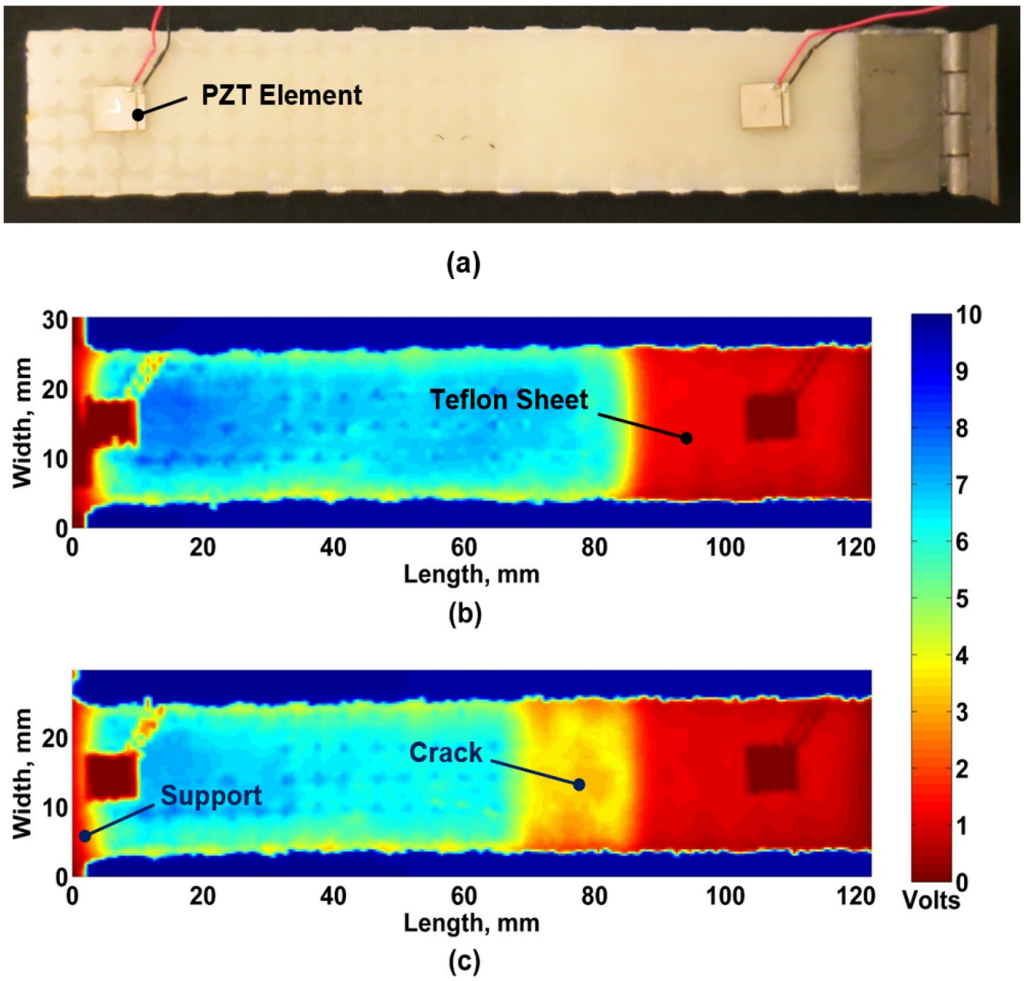

Figure 1.35: (a) GFRP DCB mode I test sample); (b) OT-scan of the DCB sample before cyclic load test; (c) OT-scan of the DCB sample after crack growth caused by cyclic load.

1.3.2.4 Detection of non-uniform adhesive distribution and fatigue damage in adhesively bonded lap-shear joints

Fig. 1.36 demonstrates OT-scans of composite lap-joints and adhesive bonds obtained at different laser radiation powers. As seen from Fig. 1.36a, the properly proportioned, cured, and distributed adhesive transmits incident radiation quite uniformly across most of the bond area. In this case, the lap-joint was cured using measures to assure consistent adhesive thickness, as mentioned above. Poor bonding is evident close the edges. In contrast, Fig. 1.36b presents the OT-scan of a similar lap-joint, where the adherends were fixed using a single C-clamp in the center of the bond area. The non-uniform pressure resulted in a apparent low-quality bonding everywhere

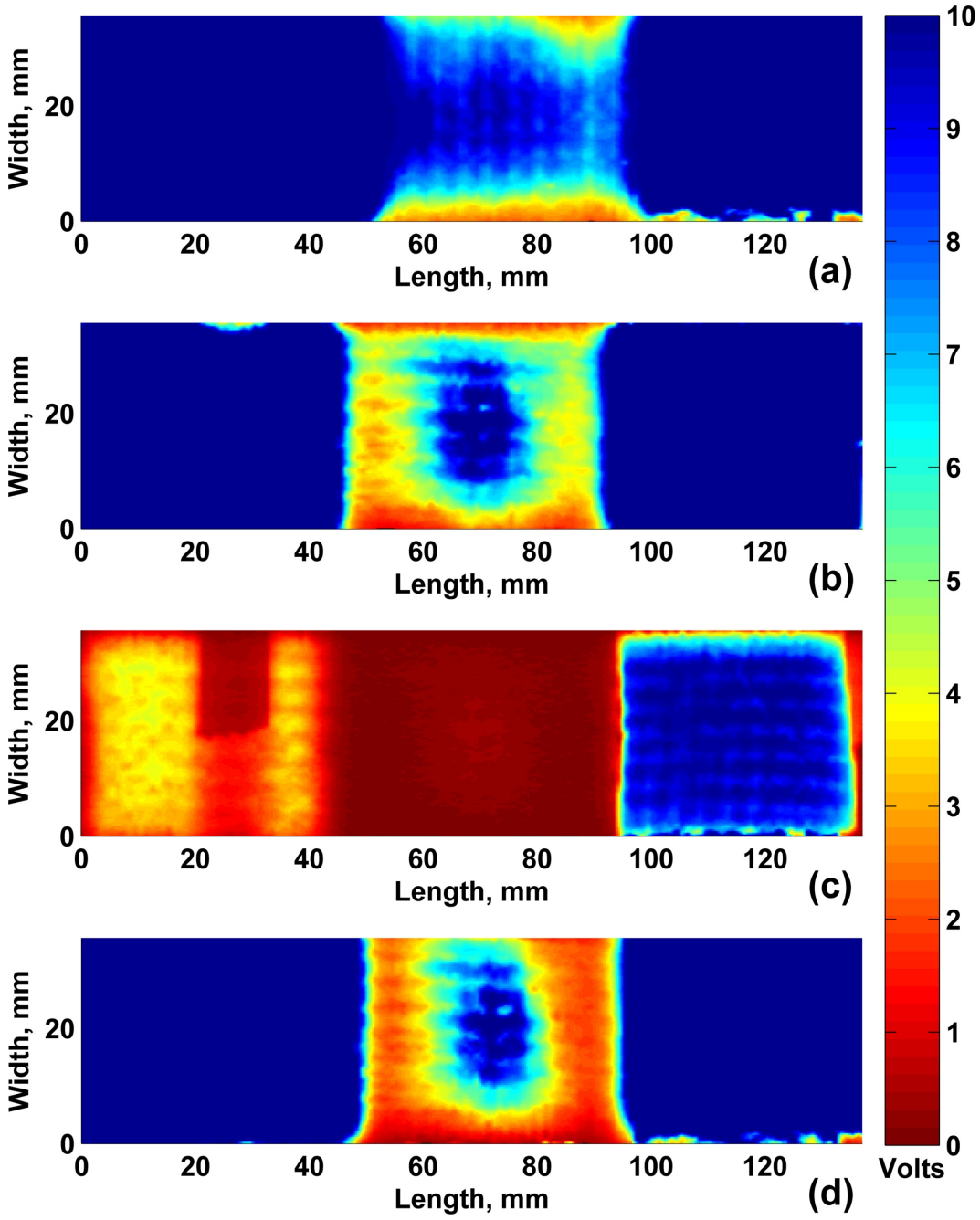

Figure 1.36: OT-scans of composite lap-joints: (a) properly cured adhesive bond, quasi-uniform pressure applied to adherends, P = 150 mW; (b) lap-joint before fatigue tests, manufactured using a single C-clamp, non-uniform pressure applied to the adherends when curing, P = 150 mW; (c) adherends of a lap-joint (output radiation power, P = 3 mW); (d) lap-joint pictured in (b) after 20000 fatigue cycles, manufactured using a single C-clamp, non-uniform pressure applied to the adherends during curing, P = 150 mW.

but directly under the clamp. The effect of fatigue degradation is illustrated in Fig. 1.36d. The adhesive started to fail at the edges and damage progressed towards the center of the bond area. This created microcracks that increased optical scattering and reduced the radiation power registered at the downstream photodetector.

1.3.3 Conclusions

These experiments highlighted the broad capabilities of the OTS system for QC and NDE of GFRP composite structures. OTS successfully detected foreign object inclusions between the plies. As expected, the technique was more sensitive to black inclusions rather than to red inclusions because the red ones have a lower transmission coefficient at the inspection wavelength of 640 *nm*. The results have also demonstrated that the OTS could easily identify GFRP samples with improperly proportioned epoxy resin, because mixing the epoxy with different ratios of part A and part B components affected the optical transmittance of the manufactured composite material as well as leading to incomplete curing. OT-scans of DCB GFRP samples revealed the true profiles of cracks introduced after mode I fracture toughness tests. Finally, the OTS showed excellent results in determining the uniformity of adhesive distribution in adhesively bonded GFRP lap-joints. Variation of the optical transmittance in the bonded area of a lap-joint was minimal when quasi-uniform pressure was applied to GFRP adherends in the bonding process. Conversely, a wide variation of clamping pressure was created when the GFRP adherends were tightened with a single C-clamp in the center of the bond area likely causing the adhesion to be weak near the edges. This uneven distribution of adhesive was clearly reflected in the OT-scans. Applying cyclic loading to the same lap-joint introduced gradual failure of the adhesive bond, which progressed from the edges towards the center. This fatigue damage was successfully captured by the OTS as optical transmittance was reduced in the damaged regions. Overall, the results obtained in Section 3, while largely qualitative in nature, demonstrated the considerable potential of the OTS technique to reliable QC and NDE problems.

1.4 Robust Implementation of OTS and Advanced NDE Features

1.4.1 OTS system with advanced scanning capabilities

A new version of a system for OTS was assembled at General Photonics Corporation (Chino, CA) for developing advanced scanning features. Functional block diagram of a new system OTS-1000 is shown in Fig. 1.37. OTS-1000 uses collimated or focused radiation from an optical source for NDE of composite samples. In terms of optical bandwidth, the source can operate at a fixed wavelength, or can be tunable. For inspection of different materials and localization of various defects, optical source can also operate in UV, visible, near-IR, and/or IR ranges. In terms of geometry of generated beam, a radiation source in the system can be point-like, line, or a plane source. Hence, the list of compatible light sources includes, but is not limited to lamps (UV, visible, and IR); broad spectrum sources such as superluminescent diodes, or ultrafast lasers (fiber, solid state, or gas lasers); diode lasers, IR emitters and many more. The attenuator in Fig. 1.37

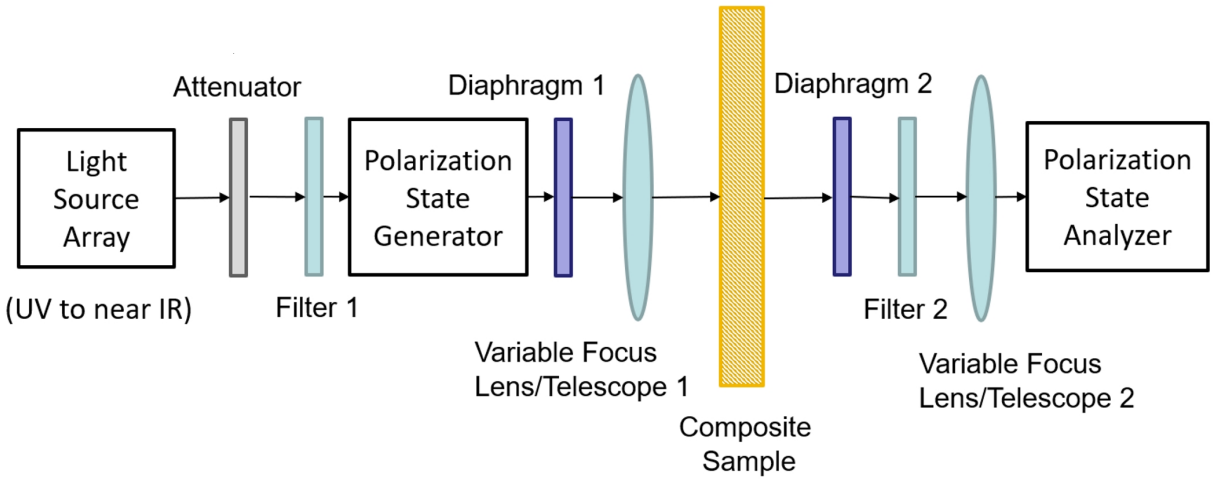

Figure 1.37: Block-diagram of OTS-1000 system for NDE of GFRP composites.

provides necessary reduction of radiation power in case the system is equipped with a high-power source, but the inspected samples are thin or highly transmissive. In general, an attenuator can be assembled based on a manually tuned, motorized, step-wise variable, or continuously variable optical element that uses absorption, reflection, diffusion, scattering, deflection, diffraction, or

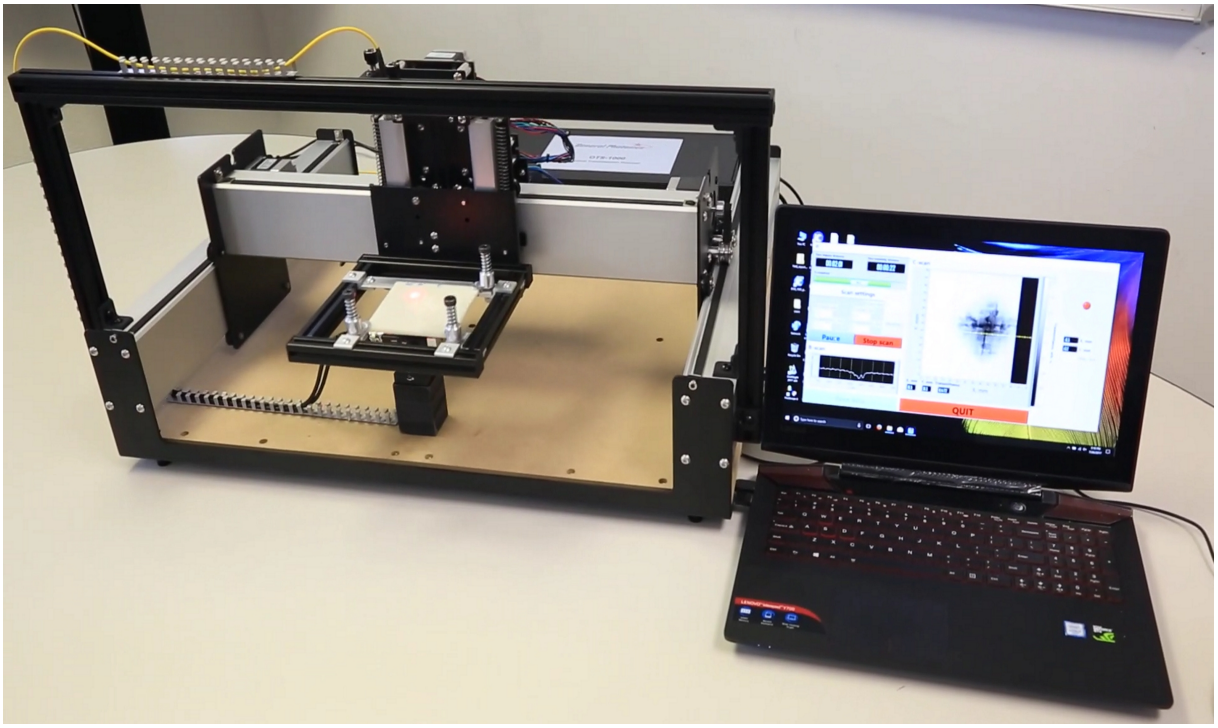

Figure 1.38: OTS-1000 system for NDE of GFRP composites.

dispersion mechanisms to adjust the level of output power. Optical filter 1 controls the bandwidth of radiation incident onto the test sample. Similarly, filter 2 is used to control the bandwidth of radiation registered on the opposite side of the sample by the photodetector. Both filters can be absorptive, interference or dichroic. In Fig. 1.37 polarization state generator (PSG) controls the state of polarization (SOP) of radiation emitted by source, and polarization state analyzer (PSA) determines the SOP of radiation tramsnitted through the sample to identify possible defects. Both PSG and PSA can be implemented as a rotating wave plate and polarizer, or can be made with binary magneto-optic (MO) polarization rotators, as described in [43–45]. The diaphragms 1 and 2 adjust the sizes of optical beams on both sides of the test sample. These can be pinholes, or iris diaphragms controlled mechanically or electrically. Variable focus lens/telescopes 1 and 2 control the focal spot and beam divergence. Lenses can be made of glass, crystals or liquid polymers, and may have fixed or variable focal lengths. Transmitted radiation is registered with suitable single point, 1D, or 2D detector, which can be optical, light, imaging, or photon sensor. Two detectors, P-detector and S-detector are used to register $\hat{p}$ and $\hat{s}$ polarizations, respectively. In OTS-1000, the

sample is moved in plane perpendicular to the direction of incident radiation using motorized 2D stage. The photo of the new OTS system is shown in Fig. 1.38. The updated experimental setup has the following features:

- Rugged hardware and stable software for rapid scanning of relatively large samples.
- Optical resolution of 100 μm.
- Positioning accuracy up to 50 μm.
- Scan speed up to 285 mm/s.
- Variable laser beam focusing.
- Ability to acquire OT-scans in regular lab environment outside of a dark room.
- Modular structure for easy switching between different light sources and photodetectors.

1.4.2 Multi-wavelength evaluation of GFRP structures

OTS setup can be operated at different inspection wavelengths providing complete characterization of complex structures with two or more components. Since optical attenuation depends on the inspection wavelength, the use of multiple wavelengths (e.g. light source array or tunable light source), allows for more detailed evaluation of materials under test. For instance, different types of defects may have different optical transmittances at a particular wavelength. Moreover, multi-wavelength approach allows for NDE of complex structures with two or more materials, such as adhesively bonded joints.

A technique for evaluation of bond-line thickness in lap-shear joints is provided here as an example. The adherends and the adhesive are considered homogeneous, hence Eq. (1.9) can be used to evaluate the optical transmittance of the bond-line section. Fig. 1.39 illustrates the geometry of a lap-joint. The thickness of adhesive layer is h_a, and combined thickness of the adherends is $h_p = h_{p_1} + h_{p_2}$.

According to Eq. (1.4), radiation power transmitted through the bond-line for i-th inspection wavelength is

$$P_i = P_0 \cdot e^{-\left(\alpha_{p_i} h_{p_1} + \alpha_{a_i} h_a + \alpha_{p_i} h_{p_2}\right)} = P_0 \cdot e^{-\left(\alpha_{p_i} h_p + \alpha_{a_i} h_a\right)}, \tag{1.36}$$

where P_0 is the power of incident radiation, and α_{p_i} and α_{a_i} are known attenuation coefficients for i-th inspection wavelength of homogeneous adherend (plate) and adhesive, respectively. OT-scans at two inspection wavelengths are needed to solve for h_a and h_p.

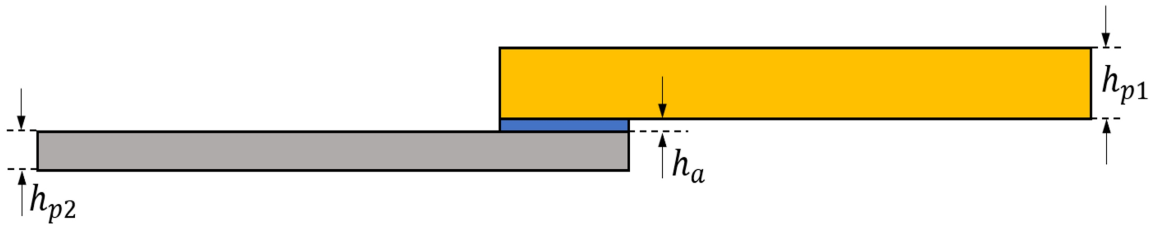

Figure 1.39: Geometry of adhesively bonded lap-joint.

Hence, we have:

$$\begin{cases} P_1 = P_0 \cdot e^{-(\alpha_{p_1} h_p + \alpha_{a_1} h_a)} \\ P_2 = P_0 \cdot e^{-(\alpha_{p_2} h_p + \alpha_{a_2} h_a)}, \end{cases} \tag{1.37}$$

where P_1 and P_2 are optical powers transmitted through adhesive bond-line at wavelength λ_1 and λ_2, respectively.

$$\begin{cases} ln\left(\frac{P_0}{P_1}\right) = \alpha_{p_1} h_p + \alpha_{a_1} h_a \\ ln\left(\frac{P_0}{P_2}\right) = \alpha_{p_2} h_p + \alpha_{a_2} h_a \end{cases} \tag{1.38}$$

Let's rearrange equations in the following way:

$$\begin{cases} ln\left(\frac{P_0}{P_1}\right) \cdot \alpha_{p_2} - ln\left(\frac{P_0}{P_2}\right) \cdot \alpha_{p_1} = \alpha_{p_1} \cdot \alpha_{p_2} \cdot h_a - \alpha_{a_2} \cdot \alpha_{p_1} \cdot h_a \\ ln\left(\frac{P_0}{P_1}\right) \cdot \alpha_{a_2} - ln\left(\frac{P_0}{P_2}\right) \cdot \alpha_{a_2} = \alpha_{a_2} \cdot \alpha_{p_1} \cdot h_p - \alpha_{a_1} \cdot \alpha_{p_2} \cdot h_p \end{cases} \tag{1.39}$$

Combining expressions with logarithms in Eq. (1.39) yields

$$\begin{cases} h_a \cdot \left(\alpha_{a_1} \cdot \alpha_{p_2} - \alpha_{a_2} \cdot \alpha_{p_1}\right) = ln\left(\frac{P_0}{P_1}\right)^{\alpha_{p_2}} - ln\left(\frac{P_0}{P_2}\right)^{\alpha_{p_1}} \\ -h_p \cdot \left(\alpha_{a_1} \cdot \alpha_{p_2} - \alpha_{a_2} \cdot \alpha_{p_1}\right) = ln\left(\frac{P_0}{P_1}\right)^{\alpha_{a_2}} - ln\left(\frac{P_0}{P_2}\right)^{\alpha_{a_1}} \end{cases} \tag{1.40}$$

$$\begin{cases} h_a \cdot \left(\alpha_{a_1} \cdot \alpha_{p_2} - \alpha_{a_2} \cdot \alpha_{p_1}\right) = ln\left[\frac{\left(\frac{P_0}{P_1}\right)^{\alpha_{p_2}}}{\left(\frac{P_0}{P_2}\right)^{\alpha_{p_1}}}\right] \\ h_p \cdot \left(\alpha_{a_1} \cdot \alpha_{p_2} - \alpha_{a_2} \cdot \alpha_{p_1}\right) = ln\left[\frac{\left(\frac{P_0}{P_1}\right)^{\alpha_{a_2}}}{\left(\frac{P_0}{P_2}\right)^{\alpha_{a_1}}}\right] \end{cases} \tag{1.41}$$

$$\begin{cases} h_a \cdot \left(\alpha_{a_1} \cdot \alpha_{p_2} - \alpha_{a_2} \cdot \alpha_{p_1}\right) = ln\left[\frac{P_0^{\left(\alpha_{p_2} - \alpha_{p_1}\right)}}{P_1^{\alpha_{p_2}} \cdot P_2^{-\alpha_{p_1}}}\right] \\ h_p \cdot \left(\alpha_{a_1} \cdot \alpha_{p_2} - \alpha_{a_2} \cdot \alpha_{p_1}\right) = ln\left[\frac{P_0^{\left(\alpha_{a_1} - \alpha_{a_2}\right)}}{P_2^{\alpha_{a_1}} \cdot P_1^{-\alpha_{a_2}}}\right] \end{cases} \tag{1.42}$$

Finally, we can find expressions for the thicknesses

$$\begin{cases} h_a \cdot \left(\alpha_{a_1} \cdot \alpha_{p_2} - \alpha_{a_2} \cdot \alpha_{p_1}\right) = \left(\alpha_{p_2} - \alpha_{p_1}\right) \cdot lnP_0 - ln\left(P_1^{\alpha_{p_2}} \cdot P_2^{-\alpha_{p_1}}\right) \\ h_p \cdot \left(\alpha_{a_1} \cdot \alpha_{p_2} - \alpha_{a_2} \cdot \alpha_{p_1}\right) = \left(\alpha_{a_1} - \alpha_{a_2}\right) \cdot lnP_0 - ln\left(P_2^{\alpha_{a_1}} \cdot P_1^{-\alpha_{a_2}}\right) \end{cases} \tag{1.43}$$

$$\begin{cases} h_a = \frac{(\alpha_{p_2} - \alpha_{p_1}) \cdot lnP_0 + \alpha_{p_1} \cdot lnP_2 - \alpha_{p_2} \cdot lnP_1}{\alpha_{a_1} \cdot \alpha_{p_2} - \alpha_{a_2} \cdot \alpha_{p_1}} \\ h_p = \frac{(\alpha_{a_1} - \alpha_{a_2}) \cdot lnP_0 + \alpha_{a_2} \cdot lnP_1 - \alpha_{a_1} \cdot lnP_2}{\alpha_{a_1} \cdot \alpha_{p_2} - \alpha_{a_2} \cdot \alpha_{p_1}} \end{cases} \tag{1.44}$$

Following all steps from Eq. (1.37) to Eq. (1.44), the thicknesses of the adhesive bond-line and adherends (h_a and h_p) can be obtained from two OT-scans acquired at λ_1 and λ_2, respectively. It should be noted that if composite structure consists of more than two materials, more OT-scans at different wavelengths need to be acquired.

1.4.3 State of polarization measurements

Adding polarization state generator (PSG) and polarization state analyzer (PSA) to the OTS system allows for measuring local changes of SOP at each scan step in order to better characterize defects. The schematics of PSG and PSA are shown in Fig. 1.40 and Fig. 1.41, respectively.

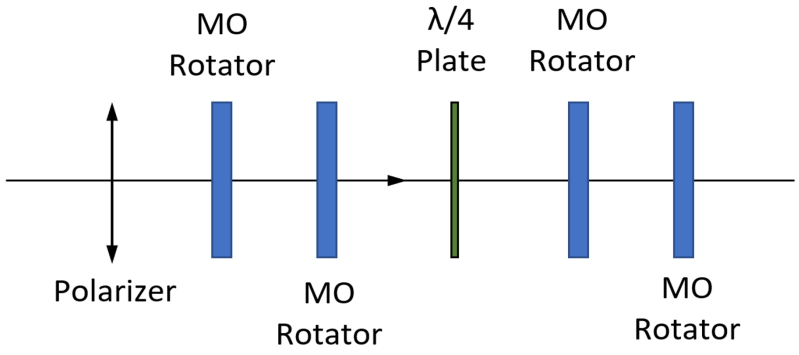

Figure 1.40: Polarization state generator based on 4 magneto-optic rotators.

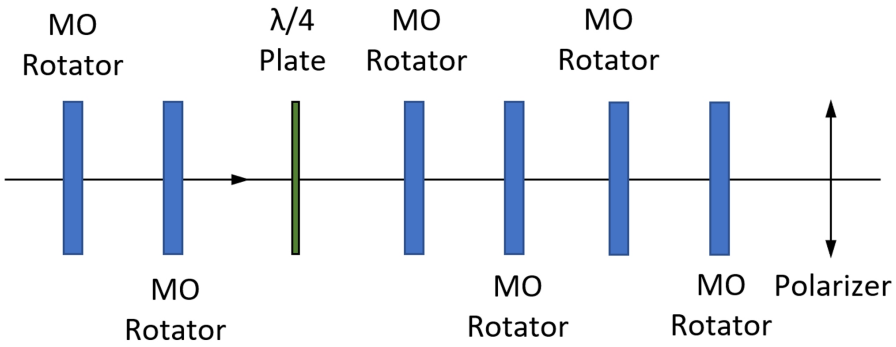

Figure 1.41: Polarization state analyzer based on 6 magneto-optic rotators.

Both PSG and PSA can be built on pairs of magneto-optic (MO) rotators. MO rotator has the following properties:

- when a positive magnetic field exceeding the strength of saturation field is applied, the rotator rotates the SOP by 22.5° .
- when a negative magnetic field is applied beyond the saturation point, the rotator rotates the SOP by -22.5° .

Hence, when both rotators in each pair rotate in the same direction, the net rotation of SOP is $+45^\circ$ or -45° . However, if two rotators rotate in opposite directions, their modifications of SOP cancel each other, and the net SOP rotation is zero. Assuming that the polarizer is aligned with the c-axis of the $\frac{\lambda}{4}$ plate, the following SOPs can be generated by PSG (referenced with respect to the polarizer's direction):

- A linear SOP at 0° when the rotators in both pairs rotate in opposite directions.
- A linear SOP at $+45^\circ$ when the rotators in the first pair rotate in opposite directions, but the rotators in the second pair both rotate $+22.5^\circ$.
- A linear SOP at 45°, when the rotators in the first pair rotate in opposite directions but the rotators in the second pair both rotate -22.5°.
- Right hand circular (RHC), when the rotators in the first pair both rotate 22.5°.
- Left hand circular (LHC), when the rotators in the first pair both rotate -22.5°.

Note that 4 distinct polarization angles produce 16 SOP combinations. However, only 5 SOP states are unique and the rest are degenerate. In principle, only 4 SOPs are required for calculation of the Mueller matrix. However, some applications may require 6 distinct SOPs for better accuracy. To generate 6 SOPs another MO rotator pair can be added to the PSG to produce additional $+45^\circ$ and -45° rotations, similarly to PSA shown in Fig. 1.41. Note that this 6-bit device (with 6 binary MO switches) can theoretically generate 64 states; however, only 6 states will be non-degenerate.

The Mueller matrix $\boldsymbol{M}$ of inspected composite sample can be obtained using a combination of PSG and PSA shown in Fig. 1.37. Let the Stokes vector of the i-th output of the PSG be:

$$S_i^{PSG} = \begin{pmatrix} S_{0i}^{PSG} \\ S_{1i}^{PSG} \\ S_{2i}^{PSG} \\ S_{3i}^{PSG} \end{pmatrix} \tag{1.45}$$

Corresponding Stokes vectors measured by the PSA after the radiation passes through the sample are related to Mueller matrix $\boldsymbol{M}$ by:

$$S_i^{PSA} = \begin{pmatrix} S_{0i}^{PSA} \\ S_{1i}^{PSA} \\ S_{2i}^{PSA} \\ S_{3i}^{PSA} \end{pmatrix} = \begin{pmatrix} m_{00} & m_{01} & m_{02} & m_{03} \\ m_{10} & m_{11} & m_{12} & m_{13} \\ m_{20} & m_{21} & m_{22} & m_{23} \\ m_{30} & m_{31} & m_{32} & m_{33} \end{pmatrix} \cdot \begin{pmatrix} S_{0i}^{PSG} \\ S_{1i}^{PSG} \\ S_{2i}^{PSG} \\ S_{3i}^{PSG} \end{pmatrix} \tag{1.46}$$

At least 4 non-degenerate SOPs must be generated by the PSG and analyzed by the PSA to completely determine the Mueller matrix $\boldsymbol{M}$ by solving Eq. (1.46). In such a case, $i = 0, 1, 2, 3$ in Eq. (1.45) and Eq. (1.46). However, for higher accuracy, we require that as many as 6 non-degenerate SOPs would be generated by the PSG and analyzed by the PSA, so that $i = 0, 1, 2 \ldots 5$. Let's define a new matrix $\boldsymbol{S}^{PSA}$ as:

$$\begin{aligned} \boldsymbol{S}^{PSA} &= \begin{pmatrix} S_{00}^{PSA} & S_{01}^{PSA} & S_{02}^{PSA} & S_{03}^{PSA} & S_{04}^{PSA} & S_{05}^{PSA} \\ S_{10}^{PSA} & S_{11}^{PSA} & S_{12}^{PSA} & S_{13}^{PSA} & S_{14}^{PSA} & S_{15}^{PSA} \\ S_{20}^{PSA} & S_{21}^{PSA} & S_{22}^{PSA} & S_{23}^{PSA} & S_{24}^{PSA} & S_{25}^{PSA} \\ S_{30}^{PSA} & S_{31}^{PSA} & S_{32}^{PSA} & S_{33}^{PSA} & S_{34}^{PSA} & S_{35}^{PSA} \end{pmatrix} \\ &= \begin{pmatrix} m_{00} & m_{01} & m_{02} & m_{03} \\ m_{10} & m_{11} & m_{12} & m_{13} \\ m_{20} & m_{21} & m_{22} & m_{23} \\ m_{30} & m_{31} & m_{32} & m_{33} \end{pmatrix} \cdot \begin{pmatrix} S_{00}^{PSA} & S_{01}^{PSA} & S_{02}^{PSA} & S_{03}^{PSA} & S_{04}^{PSA} & S_{05}^{PSA} \\ S_{10}^{PSG} & S_{11}^{PSG} & S_{12}^{PSG} & S_{13}^{PSG} & S_{14}^{PSG} & S_{15}^{PSG} \\ S_{20}^{PSG} & S_{21}^{PSG} & S_{22}^{PSG} & S_{23}^{PSG} & S_{24}^{PSG} & S_{25}^{PSG} \\ S_{30}^{PSG} & S_{31}^{PSG} & S_{32}^{PSG} & S_{33}^{PSG} & S_{34}^{PSG} & S_{35}^{PSG} \end{pmatrix} \\ &= \boldsymbol{M} \cdot \boldsymbol{S}^{PSG} \end{aligned} \tag{1.47}$$

Consequently, the Mueller matrix $\boldsymbol{M}$ of the inspected sample can be obtained from

$$\boldsymbol{M} = \boldsymbol{S}^{PSA} \cdot \left(\boldsymbol{S}^{PSG}\right)^T \cdot \left[\boldsymbol{S}^{PSG} \cdot \left(\boldsymbol{S}^{PSG}\right)^T\right]^{-1}, \tag{1.48}$$

where $\left(\boldsymbol{S}^{PSG}\right)^T$ is the transpose of matrix $\boldsymbol{S}^{PSG}$. More detailed Mueller matrix analysis is provided in [34, 35]. The changes in SOP parameters may be attributed to the superstructure, defects, or introduced stresses inside the tested sample.

1.4.4 Separation of ballistic and scattered photons

Separation of scattered photons from the ballistic photons is important in applications, where scattering properties of studied material are evaluated. Basic ways to accomplish this are based either on spatial or temporal separation. In the first case, ballistic photons can be split from scattered photons spatially by using a pinhole or 2D detector. Ballistic photons are registered in the center of the photodetector, and fraction of scattered photons is easily calculated by subtraction of radiation power of the ballistic photons from the total radiation power. Another way is to separate ballistic

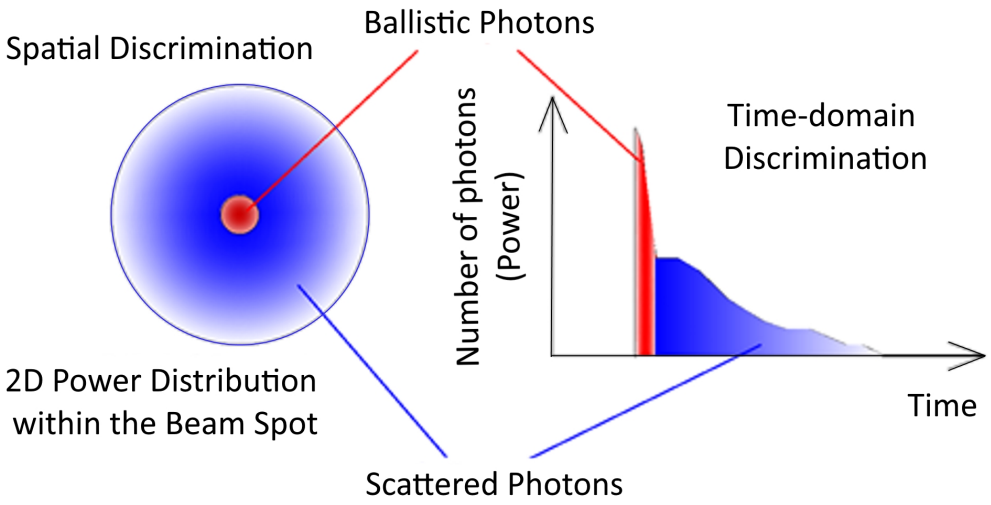

Figure 1.42: Spatial and temporal discrimination of ballistic and scattered photons.

and scattered photons in time domain by using a high-speed photodetector. In this case, ballistic photons will contribute to the registered signal with characteristic spike, while scattered radiation will have broad envelope following the peak from ballistic photons. Both spatial and time domain discrimination concepts are illustrated in Fig. 1.42.

In addition, if scattering of radiation inside the test sample is well described by mechanisms of Rayleigh scattering, which depends on the inspection wavelength, the light source array or tunable light source would also provide the ability to discriminate scattered photons from ballistic photons. If absorption spectrum of the studied material is known, and Rayleigh scattering proportional to

$\frac{\lambda}{4}$ is taken into account, transmitted radiation for two inspection wavelengths λ_1 and λ_2 can be approximated as:

$$\begin{cases} P_1 \approx (1 - A_1) \cdot \left(B + \frac{S}{\lambda_1^4} \right) \\ P_2 \approx (1 - A_2) \cdot \left(B + \frac{S}{\lambda_2^4} \right), \end{cases} \tag{1.49}$$

where A_1 and A_2 are known absorption constants, B is the fraction of ballistic photons, and S is proportional to the number of scattered photons. The solution to Eq. (1.49) yields:

$$B \approx \frac{1}{\left(\lambda_1^4 - \lambda_2^4 \right)} \cdot \left[\frac{P_1 \lambda_1^4}{1 - A_1} - \frac{P_2 \lambda_2^4}{1 - A_2} \right] \tag{1.50}$$

1.4.5 Feasibility of 3D imaging

3D scanning should be implemented in order to determine the exact location of the defect in the transect of the inspected sample. One way to perform such scanning is to analyze the dependence of the transmitted power on the position of the focal plane. In this case, the beam focus is shifted from the front to the rear surface of the sample manually or using a variable focus lens. Fig. 1.43

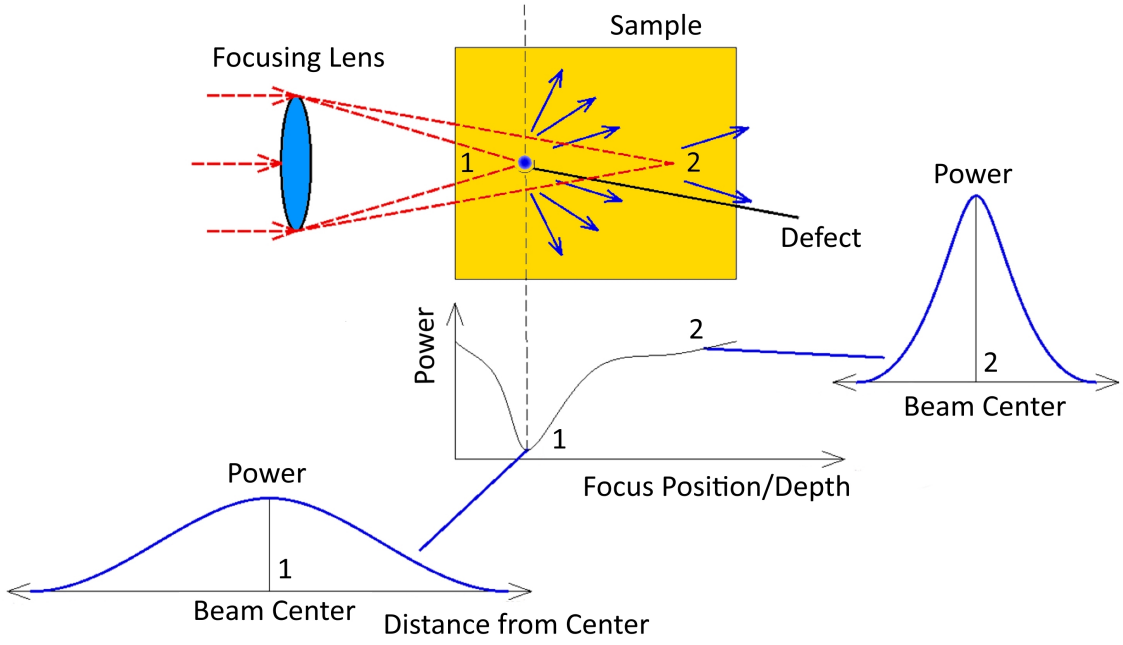

Figure 1.43: 3D scanning concept using variable focus lens.

illustrates an example of scattering from a defect inside the sample. When focal position is in the vicinity of defect (Position 1), most of the radiation will scattered away from the photodetecor, and minimal power will be registered. In contrast, when the beam is focused at Position 2, only a small portion of the incident radiation is scattered by the defect, and registered power is maximal.

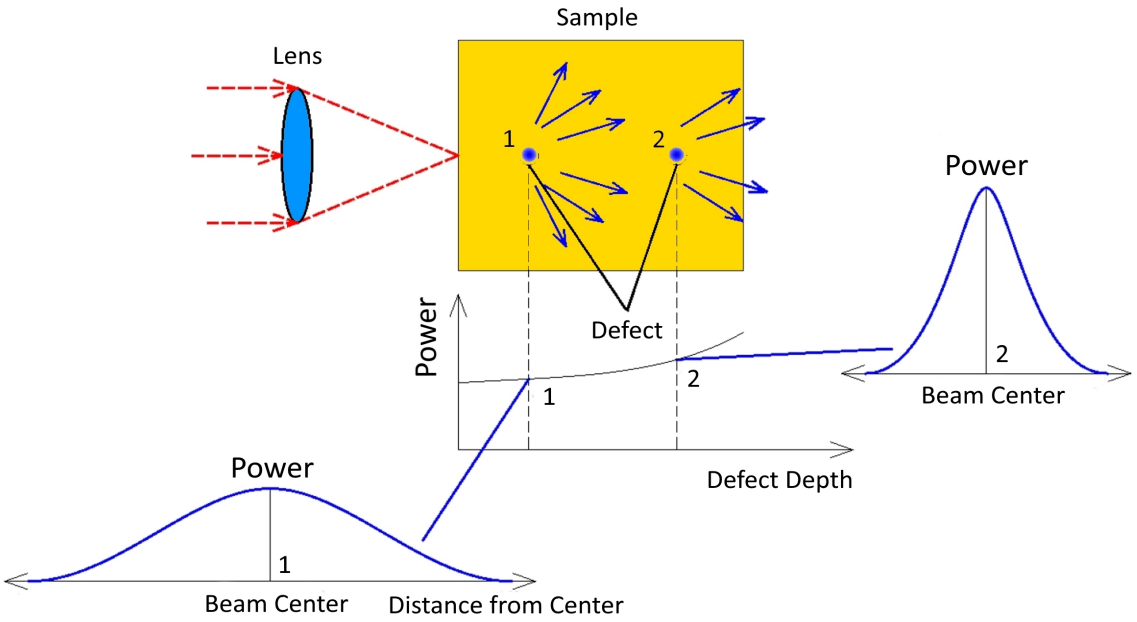

Figure 1.44: 3D scanning concept using scattering pattern correlation.

Another way to locate the position of defect in the transect of the sample is to correlate the 2D scattering pattern with defect depth while the focus of the optical lens is fixed at an optimal position. In this case, the distribution of transmitted power is measured using a 2D photodetector. In the example illustrated in Fig. 1.44, optical focus hits the defect at Position 1 prior to the defect at Position 2. Assuming scattering occurs at the same solid angle for both defects, the 2D power distribution corresponding to defect at Position 1 will be more spread out compared to that of at Position 2. This is explained by different distances from two defects to the same photodetector. Fig. 1.45 illustrates a simple experimental setup for validation of a 3D scanning concept. In this case, power of transmitted radiation was measured as a function of focal distance along the vertical scanning axis. Pig tailed light source was focused on the surface of the sample, and the focal point was changed by moving the source with the Z-axis motor of the OTS-1000. The sample was a

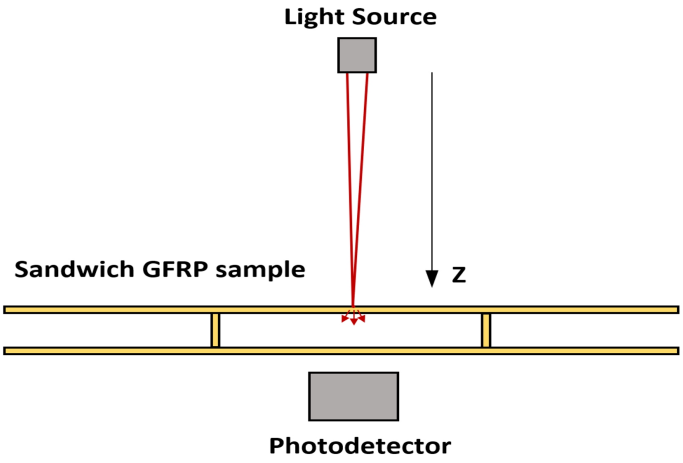

Figure 1.45: Schematic of the experimental setup for measuring the power of transmitted radiation as a function of focal distance along Z-axis.

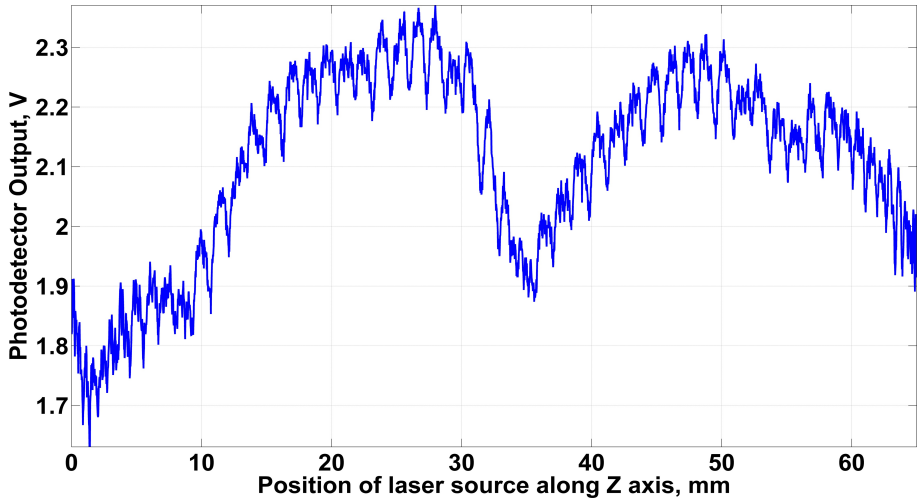

Figure 1.46: Measured signal as a function of focal distance along Z-axis.

GFRP sandwich panel with two 2-*mm* skins and empty core. The gap between top and bottom skins was 6 *mm*. Positions of the sample and the photodetector were fixed as they were mounted on a separate mechanical fixture. Obtained results are demonstrated in Fig. 1.46. Apparently, two lobes of measured signal correspond to top and bottom GFRP interfaces. High-frequency oscillations are probably caused by vibrations, as the light source wasn't perfectly mounted on the Z-axis fixture of the gantry. Hence, the results being largely qualitative in nature, still demonstrate the sensitivity of the technique to changes of internal structure of tested samples along their thickness, and show potential for further refinement of OTS by implementing scanning along depth.

1.4.6 Detection of fiber breakage, lack of infusion, air voids and fiber waviness

Performance of the OTS system was successfully validated on various GFRP samples with macro- and microscopic defects. For instance, Fig. 1.47 demonstrates the OT-scan of a GFRP sample with dry fibers owing to lack of infusion, and cracks. Other details such as black marks, left overs of tape and scratches are also visible. The scan resolution is 100 μm for both axes.

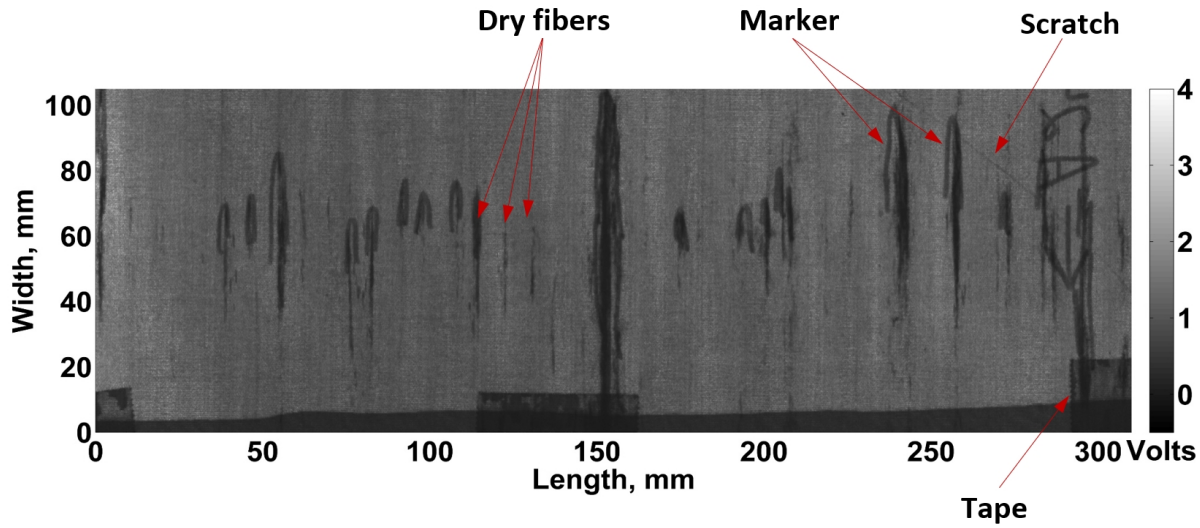

Figure 1.47: OT-scan of GFRP sample with lack of infusion (dry spots) and cracks.

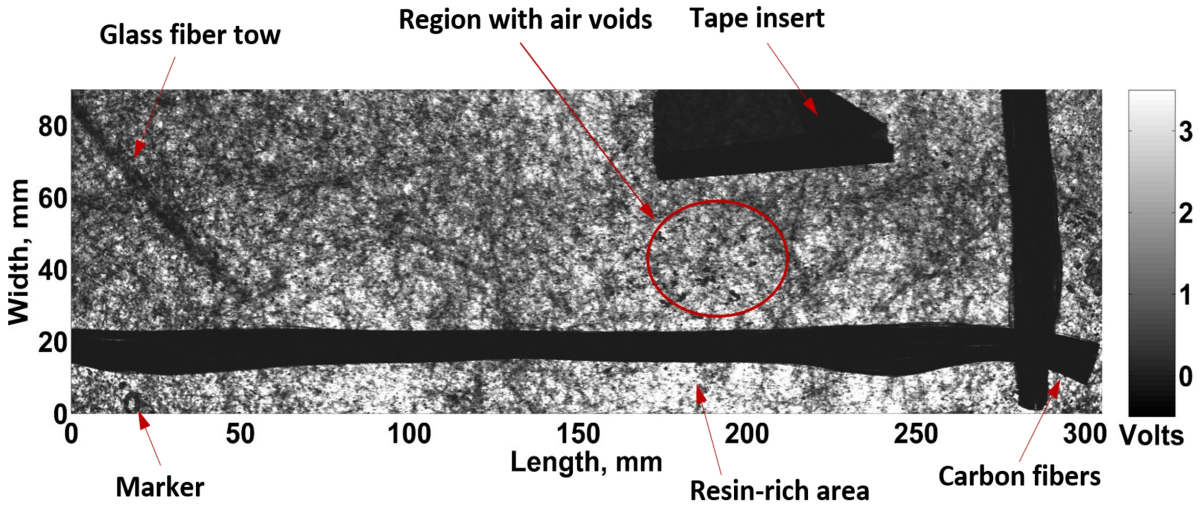

Figure 1.48: GFRP sample with irregular distribution of chopped glass fibers. Region with air bubbles is highlighted with red ellipse.

Fig. 1.48 shows a GFRP composite plate manufactured with chopped glass fibers. Major defects detected in this sample were:

- a bundle of long glass fibers on the left;
- insertion of carbon fibers in the bottom of the test sample and on its right side;
- film insert in the upper part of the sample;
- agglomerations of air voids.

Resin-rich areas corresponded to brighter regions of the OT-scan, while fiber-rich areas were darker on current gray scale colormap. Air bubbles present in the sample appeared as dark dots owing to scattering of incident radiation. The average size of these dots was approximately 0.5 *mm*.

Fig. 1.49 and Fig. 1.50 show detailed OT-scans of another GFRP composite with chopped fibers acquired at 640 *nm* and 1310 *nm* (visible versus infrared ranges). No apparent defects are present, but uneven distributions of fibers and matrix are well captured. Interestingly, the 1310 *nm* OT-scan is more sensitive to irregularities of matrix distribution, while fibers are seen much better on a 640 *nm* OT-scan. Apparently, this is explained by different transmission coefficients of fibers and matrix at selected inspection wavelengths. Zooming into different segments of the OT-scan shown in Fig. 1.47 allows for detailed visualization of individual glass fiber tows (see Fig. 1.51). In Fig. 1.51 fibers seem to be well aligned. However, when looking at Fig. 1.52, one may notice that fibers are wavy. Fiber waviness is highlighted with red dotted line.

1.4.7 Conclusions

In this Section, a new robust version of OTS system was presented. Advanced NDE features such as high-spatial scan resolution, high-speed scanning using array sources, multi-wavelength measurement capability, SOP measurements, separation of ballistic and scattered photons, and 3D imaging of defects by means of laser beam focusing were discussed. OTS was succesfully used for detection of fiber breakage, lack of infusion, air voids and fiber waviness in GFRP samples.

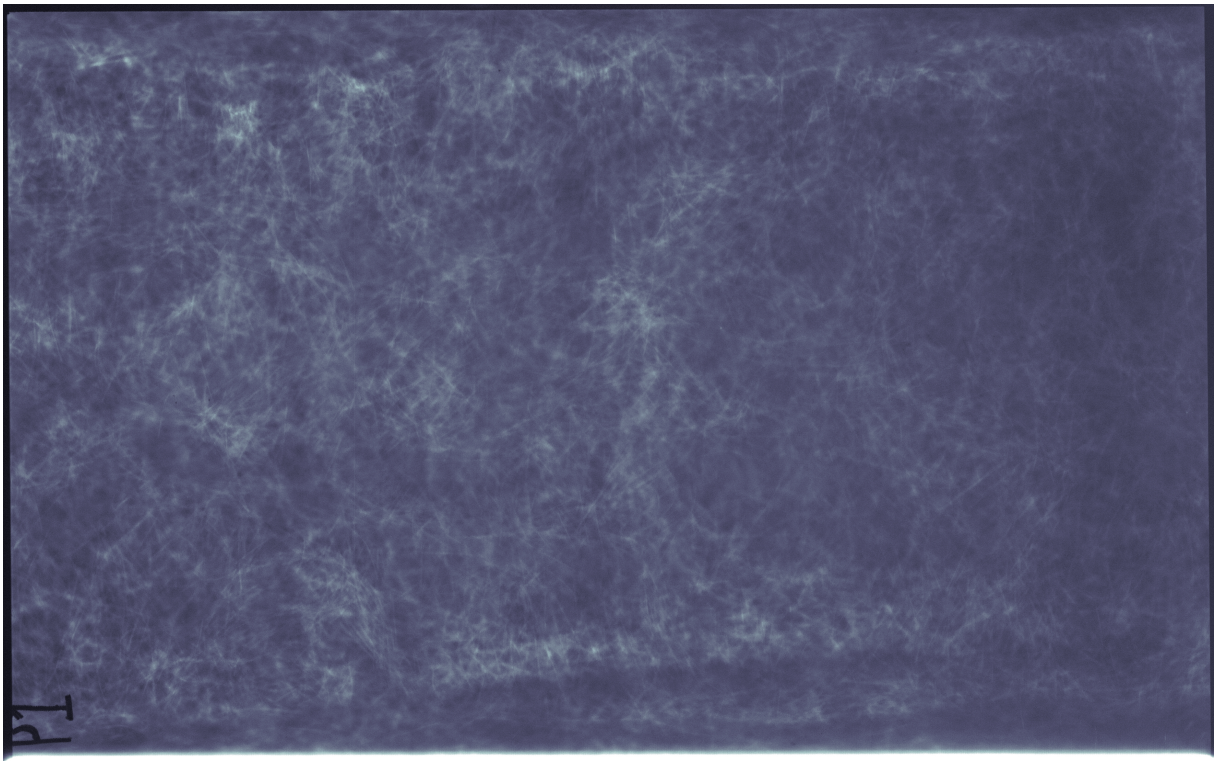

Figure 1.49: OT-scan of GFRP sample with chopped glass fibers (640 *nm* wavelength).

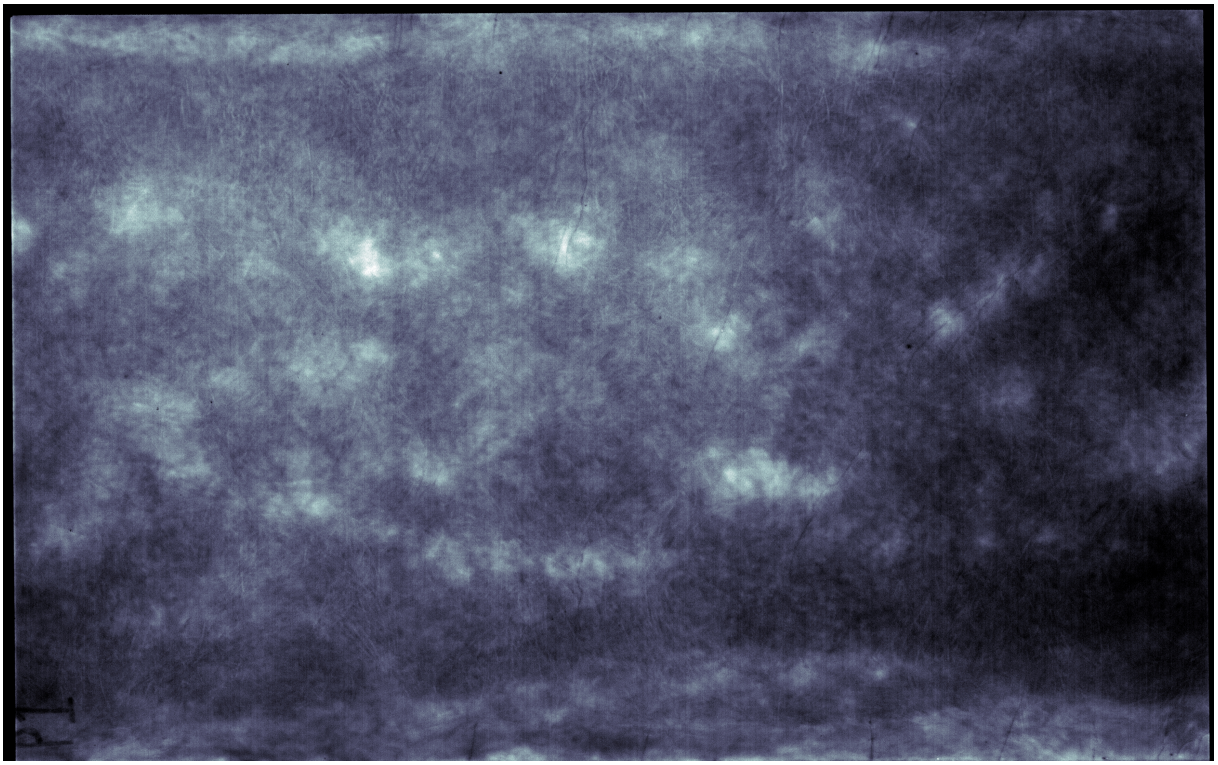

Figure 1.50: OT-scan of GFRP sample with chopped glass fibers (1310 *nm* wavelength).

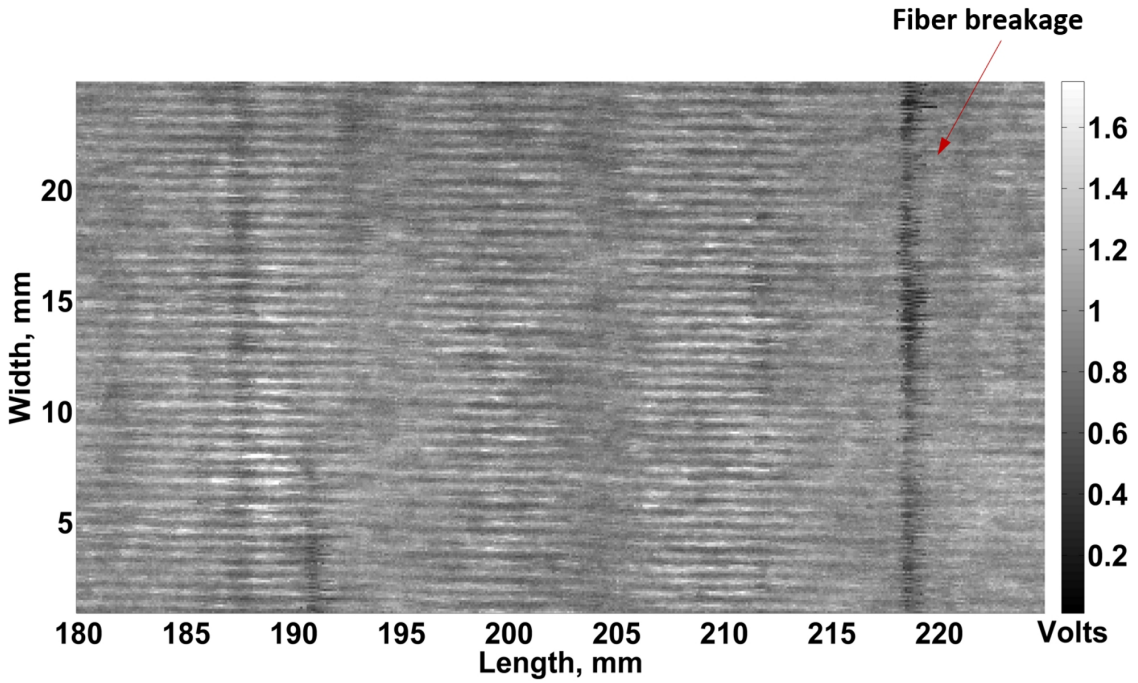

Figure 1.51: Zoomed region of the OT-scan shown in Fig. 1.47. Individual fiber tows are visible and fibers are well aligned.

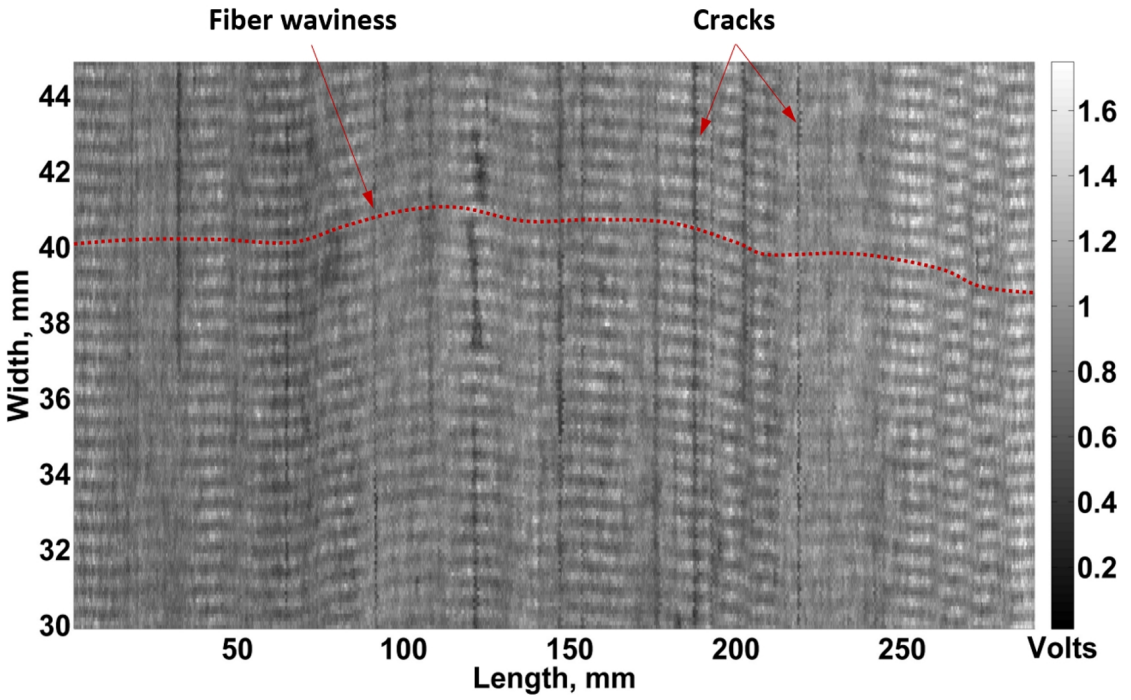

Figure 1.52: Zoomed region of the OT-scan shown in Fig. 1.47. Wavy fibers are detected.

CHAPTER 2

OPTICAL FREQUENCY DOMAIN REFLECTOMETRY FOR SHM OF STRUCTURAL COMPOSITES

2.1 Fiber-optic sensing

Data logging with fiber-optic sensors is one of the actively researched areas in SHM [46]. Optical fibers are made by drawing glass (silica) or plastic to a diameter slightly thicker than that of a human hair (on the order of μm), such that embedding them into a host specimen does not affect its intrinsic properties to any appreciable degree. Measuring the properties of light propagating through such fibers provides essential information about the state of the surrounding structure (Fig. 2.1). These key features along with immunity to electromagnetic interference and light weight make fiber-optic sensors very appealing for health monitoring of structural composites. Fiber-optic sensors can be divided into two major categories: point and distributed sensors. Point

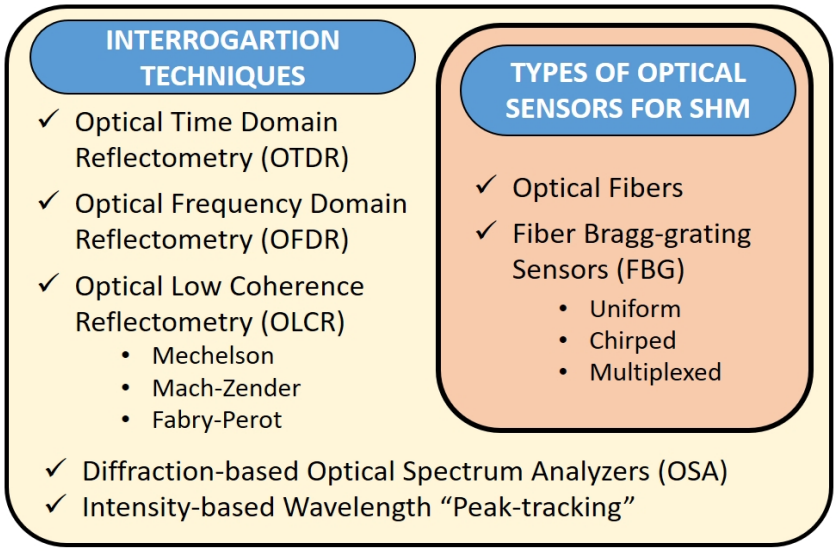

Figure 2.1: Categories of fiber-optic sensors and main interrogation techniques.

sensors provide signals from a single location, and can be broadly classified as Fiber Bragg-grating (FBG) sensors and interferometeric sensors [47]. FBG is a sensing element written in the fiber

by UV exposure, which reflects a resonant wavelength called Bragg wavelength. The Bragg wavelength is intrinsically sensitive to temperature, strain, or any other perturbations that modulate the refractive index, n of the fiber or change the grating period, Λ. By sending a broad-band radiation into an FBG and by monitoring the resonant wavelength shift, the local temperature or strain can be extracted. Interferometeric sensors are based on mode coupling theories where two or more modes of radiation propagating in the fiber undergo different optical paths and recombine at a certain point. Hence, variations of temperature or strain affect optical paths, which results in optical wavelength shifts or power variations. Recently, performance of FBG sensors and many interferometeric sensors (e.g. Sagnac, Fabry-Perot, Michelson, Mach-Zehnder and others) have been successfully demonstrated in different applications. However, the major drawback of sensing signals at a single point is that structural damage or other events occurring outside the sensing area will be missed. For instance, in the case of FBG, possible ways to alleviate this issue are:

- combine FBGs with different Bragg wavelengths into arrays through Wave-Division Multiplexing (WDM);
- use quasi-distributed sensors (e.g. continuously written fiber Bragg-gratings (CFBG));
- implement hybrid sensing techniques (as demonstrated in Chapter III).

Unlike point sensors, distributed fiber-optic sensors can be interrogated along their whole length. This key advantage makes them suitable for monitoring of complex structures (e.g. vehicles, bridges, pipelines, etc.), where knowledge of exact strain distribution is critical. In a simple case, an optical fiber itself may serve as a distributed sensor, if right interrogation technique is implemented [48]. When radiation propagates along the optical fiber, small amounts of it are reflected back through different physical mechanisms known as Raman, Brillouin and Rayleigh back scattering. Major techniques for distributed sensing are optical time domain reflectometry (OTDR) [49], optical frequency domain reflectometry (OFDR) [50] and optical low coherence reflectometry (OLCR) [51] .

2.2 Scattering of radiation in optical fibers

A spontaneous scattering spectrum of solid state medium is schematically shown in Fig. 2.2. Most photons are elastically scattered by atoms or molecules of the medium. However, a small portion of photons (approximately 1 in 10 million) is scattered inelastically. In this case, scattered photons have different frequencies and energies compared to incident photons.

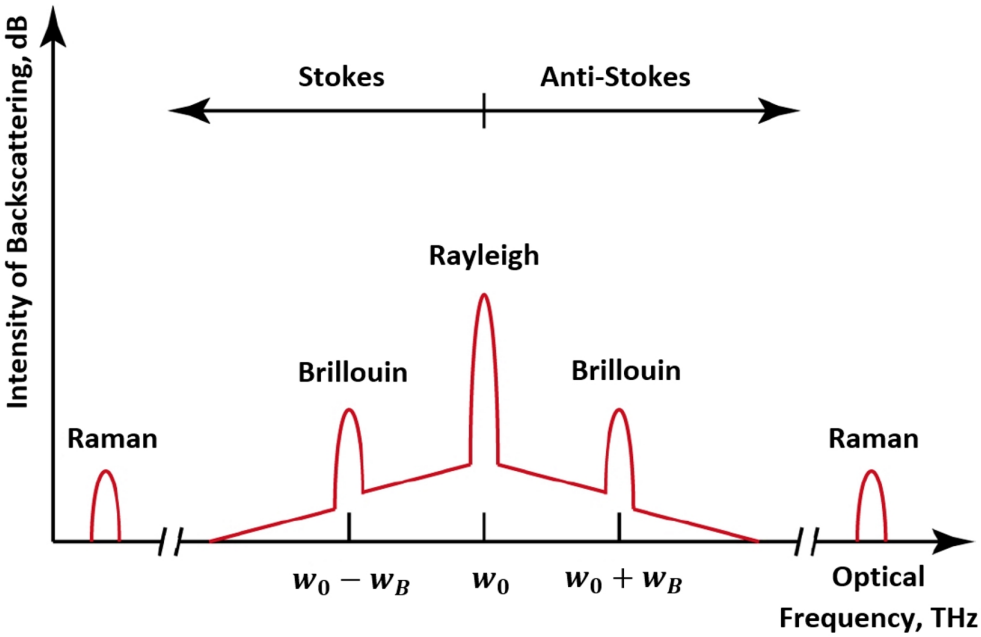

Figure 2.2: Typical spectrum of scattered radiation in solid state medium.

From the perspective of solid state physics, Brillouin scattering is an interaction between an electromagnetic wave and crystalline lattice waves in the medium (e.g. mass oscillation or acoustic modes). The scattering is inelastic meaning that the photon may lose energy (Stokes process) and in the process create a quasiparticle (phonon) or it may gain energy (anti-Stokes process) by absorbing a quasiparticle. Such a shift in photon energy, corresponding to a Brillouin shift in frequency, is equal to the energy of the released or absorbed quasiparticle. Thus, Brillouin scattering can be used to measure the energies, wavelengths and frequencies of various atomic chain oscillation types.

Raman scattering is another phenomenon that involves inelastic scattering of light caused by the vibrational properties of matter. The detected range of frequency shifts and other effects are very

different compared to Brillouin scattering. In Raman scattering, photons are scattered by the effect of vibrational and rotational transitions in the bonds between first-order neighboring atoms, while Brillouin scattering results from the scattering of photons caused by large scale, low-frequency phonons. The effects of the two phenomena provide very different information about the sample: Raman spectroscopy can be used to determine the transmitting medium's chemical composition and molecular structure, while Brillouin scattering can be used to measure the material's properties on a larger scale such as its elastic behavior.

Rayleigh scattering is known as the scattering of radiation due to non-propagating fluctuations of density, composition and orientation of molecules within the optical fiber, and hence of its refraction index. The difference between Brillouin scattering and Rayleigh scattering is that the former involves only the random and incoherent thermal fluctuations, in contrast with the correlated, periodic fluctuations (phonons).

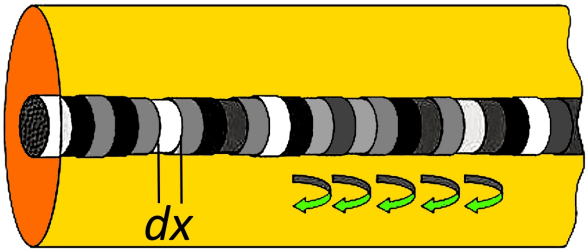

Figure 2.3: Weak FBG model describing Rayleigh scattering as superposition of point-like reflectors along the fiber.

Optical fiber can be treated as a series of infinitesimally short segments, where each segment acts as a random point-like scatterer. Hence, Rayleigh back-scattering profile along the optical fiber can be modeled as a sequence of weak Bragg-gratings with randomly varying periods. In the case of an FBG, the resonant wavelength is determined by grating period and effective refractive index. Any change in these parameters leads to resonant wavelength shift. The Rayleigh back-scattering responds in the same manner: changes in refractive index or physical length lead to a resonant wavelength shift. By measuring the wavelength shifts, one may achieve distributed sensing, which functions as thousands of FBGs multiplexed.

2.3 OFDR operating principle

Recently, OFDR has attracted increased interest in the areas of space resolved characterization of optical fibers and components thanks to its high spatial resolution and dynamic range. OFDR has been primarily used for applications that require high spatial resolution (e.g. millimeter and sub-millimeter) with a relative short measurement range up to a few hundreds of meters. OFDR has also been implemented in various SHM projects that require distributed strain and temperature sensing. Hence, OFDR has found its use in such industries as oil and gas, aerospace, automotive and civil engineering, geophysics, and many more.

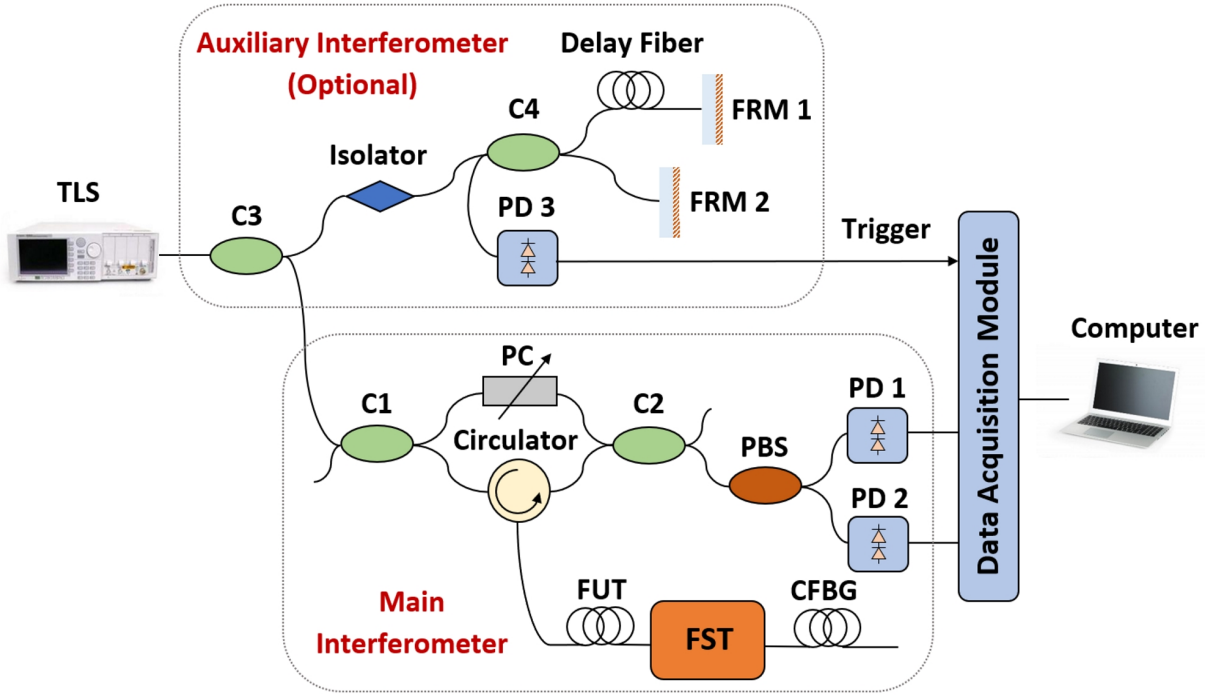

Figure 2.4: Schematics of the OFDR system for measuring Rayleigh back-scattered radiation in single-mode optical fibers.

Typical schematic of OFDR set-up is illsutrated in Fig. 2.4. OFDR system for detection of Rayleigh scattering and Fresnel reflections consists of a tunable laser source (TLS), a main interferometer with polarization diversity receiver, and auxiliary interferometer, which is optional. Radiation from TLS is split into two beams at the coupler C3. At this point, 99% of incident power goes into the main interferometer, while 1% power is sent into auxiliary interferometer.

At coupler C1, radiation power is split equally between the circulator's input and polarization controller (PC). Incident radiation propagates into the fiber under test (FUT) through the second port of the circulator, and back-reflected radiation is outputted at the third port. The back-scattered radiation from FUT interferes with radiation from TLS at the coupler C2, which produces fringe patterns. The output of C2 is split into two orthogonal polarization components ($\hat{p}$ and $\hat{s}$) by a polarization beam splitter (PBS). Intensities of beat patterns are measured by corresponding photodetectors (PD) connected to a data acquisition card (DAQ).

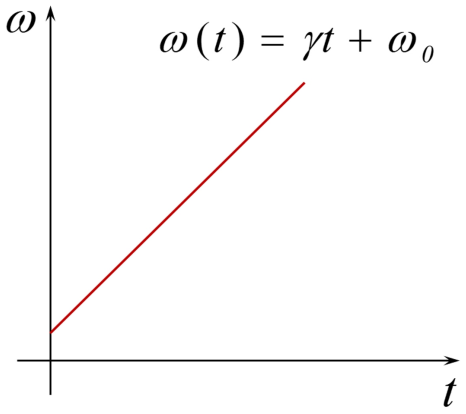

Figure 2.5: Perfect linear TLS tuning (ω is instantaneous optical frequency, ω_0 is initial optical frequency, and γ is tuning rate).

The auxiliary interferometer is used for real-time tracking of TLS optical frequency as it usually diverges from ideal curve (see Fig. 2.5). Electric circuitry generates clock signals at each "zero-crossing" position of the optical interference fringe signals, which is needed for proper data sampling by DAQ. The auxiliary interferometer is typically implemented as Michelson interferometer with Faraday rotation mirrors (FRM) and optical delay line. Such scheme mitigates tuning nonlinearity of TLS, which may severely deteriorate acquired reflectance measurements. However, perfect TLS tuning is assumed in this report, and the compensation of TLS nonlinearities is left as future work.

2.4 Theory of polarization diverse OFDR

This section presents theoretical formulation of OFDR operating principles. We shall first define the electric field at coupler C1 as a starting point for the analysis. Assuming the TLS

generates radiation with an optical frequency $\omega(t)$ and instantaneous phase of $\varphi(t)$ (as shown in Fig. 2.5), the electric field at coupler C1 can be expressed as

$$E(t) = E_0(t)e^{j\varphi(t)}, \tag{2.1}$$

where E_0 is the magnitude of the electric field, and $j = \sqrt{-1}$. Note that the instantaneous phase of the electric field is given by the following expression:

$$\varphi(t) = \int_0^t \omega(t)dt + \varphi_0, \tag{2.2}$$

where φ_0 is the initial phase of the radiation generated by the TLS. Generally, if radiation propagates in the optical fiber, the electric field at a distance l from the output of TLS is given by

$$E(\tau, t) = \frac{A}{\sqrt{2}}E_0(t-\tau)e^{j\varphi(t-\tau)}e^{-\alpha l}, \tag{2.3}$$

where τ is a propagation time delay, α is the attenuation constant, and A is a complex constant that defines phase shift of electric field introduced by couplers, circulators or other optical components along the fiber length. In Eq. (2.3), τ is defined as

$$\tau = \frac{l}{v} = \frac{l \cdot n_g}{c}, \tag{2.4}$$

where v is the group velocity, n_g is the group refractive index, and c is the speed of light in vacuum. Let's evaluate the electric field at the end of the top arm of the main interferometer. In our case, this is the optical fiber of length l_b between couplers C1 and C2. Using Eq. (2.3), electric field at the first input of C2 can be expressed as

$$E(\tau_b, t) = \frac{A_b}{\sqrt{2}}E_0(t-\tau_b)e^{j\varphi(t-\tau_b)}e^{-\alpha l_b}, \tag{2.5}$$

where τ_b is the corresponding propagation time delay. Now let's consider the propagation of radiation from the circulator to an arbitrary point z_0 along the length of the fiber under test (FUT). If the circulator is taken as origin, the electric field at location z_0 is given by

$$E\left(\tau_{z_0}, t\right) = \frac{A_{z_0}}{\sqrt{2}}E_0\left(t-\tau_{z_0}\right)e^{j\varphi\left(t-\tau_{z_0}\right)}e^{-\alpha l_{z_0}}. \tag{2.6}$$

Taking into account Rayleigh back-scattering at z_0, the radiation returned back to circulator is expressed as

$$E\left(2\tau z_0, t\right) = r(z_0)\frac{A_{2z_0}}{\sqrt{2}}E_0\left(t - 2\tau z_0\right)e^{j\varphi\left(t-2\tau z_0\right)}e^{-\alpha 2 l z_0}, \tag{2.7}$$

where $r(z_0)$ is a complex Rayleigh back-scattering coefficient that describes local variation of refractive index in the FUT. Now, similarly to Eq. (2.5), we need to obtain an expression for the electric field at the second input of coupler C2 referenced to coupler C1 as origin. For simplicity, let's assume that lengths of fiber sections between coupler C1 and circulator, and between circulator and coupler C2 are equal to $\frac{l_a}{2}$. Then the radiation from C1 will propagate through the circulator to the FUT, Raleigh-back scattering will take place at location z_0, and the resulting electric field registered at coupler C2 will be defined as

$$E\left(2\tau z_0 + \tau a, t\right) = \frac{A_{(2z_0+l_a)}}{\sqrt{2}}E_0\left(t - (2\tau z_0 + \tau a)\right)e^{j\varphi\left(t-(2\tau z_0+\tau a)\right)}e^{-\alpha\left(2 l z_0+l_a\right)}, \tag{2.8}$$

where τ_a is the combined time delay due to fiber optic paths C1-circulator and circulator-C2. Applying the weak FBG model, each point along the FUT will act as an independent reflector. Hence, Rayleigh back scattering from all points will contribute to the value of the electric field at the second input of coupler C2:

$$E_a(t) = \frac{A_a}{\sqrt{2}}\sum_z\left[r(z)E_0\left(t - (2\tau_z + \tau_a)\right)e^{j\varphi(t-(2\tau_z+\tau_a))}e^{-\alpha(2l_z+l_a)}\right]. \tag{2.9}$$

The electric field at the output of C2 is given by Jones matrix:

$$E(t) = E_a(t) + jE_b(t) = \frac{A_a}{\sqrt{2}}\sum_z\left[r(z)E_0\left(t - (2\tau_z + \tau_a)\right)e^{j\varphi(t-(2\tau_z+\tau_a))}e^{-\alpha(2l_z+l_a)}\right] + j\frac{A_b}{\sqrt{2}}E_0(t-\tau_b)e^{j\varphi(t-\tau_b)}e^{-\alpha l_b}. \tag{2.10}$$

The OFDR block diagram shown in Fig. 2.4 features polarization diverse measurement scheme to eliminate polarization dependent losses (PDL) in the fiber. This is done by splitting the radiation at the output of C2 in two orthogonal components $\hat{p}$ and $\hat{s}$, and by registering them independently using two optical photodetectors PD1 and PD2, respectively.

Hence, $\hat{p}$ and $\hat{s}$ components of the electric field are given by the following relations:

$$E_p(t) = \hat{p}\frac{T_p e^{j\varphi_p}}{2}\left(\sum_z A_a \left[r_p(z) E_0 \left(t - (2\tau_z + \tau_a)\right) e^{j\varphi(t-(2\tau_z+\tau_a))} e^{-\alpha(2l_z+l_a)} \right] + jA_b E_0(t-\tau_b) e^{j\varphi(t-\tau_b)} e^{-\alpha l_b} \right), \quad (2.11)$$

$$E_s(t) = \hat{s}\frac{T_s e^{j\varphi_s}}{2}\left(\sum_z A_a \left[r_s(z) E_0 \left(t - (2\tau_z + \tau_a)\right) e^{j\varphi(t-(2\tau_z+\tau_a))} e^{-\alpha(2l_z+l_a)} \right] + jA_b E_0(t-\tau_b) e^{j\varphi(t-\tau_b)} e^{-\alpha l_b} \right), \quad (2.12)$$

where $\hat{p}$ and $\hat{s}$ are orthogonal unit vectors; T_p and T_s are the split coefficients of PBS; φ_p and φ_s are the phase shift coefficients of PBS; and r_p and r_s are the Rayleigh back-scattering coefficients for $\hat{p}$ and $\hat{s}$ electric field components, respectively.

Let's consider the $\hat{p}$ component of the electric field's intensity registered by photodetector PD1:

$$I_p(t) = E_p(t) \cdot E_p(t)^* \quad (2.13)$$

As the DC part of $I_p(t)$ contains no useful information about the Rayleigh back-scattering profile of the FUT, only the AC part is taken into account [52]:

$$I_p^{AC}(t) = \frac{T_p^2 A_a A_b^*}{4} \sum_z \left(e^{-\alpha(2l_z+l_a+l_b)} r_p(z) E_0 \left(t - (2\tau_z + \tau_a)\right) E_0^*(t-\tau_b) \right) \times e^{j\left(\varphi(t-(2\tau_z+\tau_a)) - \varphi(t-\tau_b)\right)} + c.c., \quad (2.14)$$

where $c.c.$ denotes the complex conjugate of the first term in the equation. Assuming linear tuning of optical frequency by TLS (see Fig. 2.5), the instantaneous optical phase is given by:

$$\varphi(t) = \int_0^t \omega(t)dt = \int_0^t (\gamma t + \omega_0)dt = \frac{1}{2}\gamma t^2 + \omega_0 t + \varphi_0, \quad (2.15)$$

where φ_0 is the initial optical phase of TLS output. Using Eq. (2.15), the phase term of a complex exponential in Eq. (2.14) can be simplified into

$$\varphi\left(t - (2\tau_z + \tau_a)\right) - \varphi(t-\tau_b) = \frac{1}{2}\gamma\left(\tau_b - \tau_a - 2\tau_z\right)\left(2t - (2\tau_z + \tau_a + \tau_b)\right) + \omega_0\left(\tau_b - \tau_a - 2\tau_z\right) \quad (2.16)$$

Since τ_a and τ_b are time delays due to sections of optical fibers inside the OFDR instrument, they can be adjusted to have the same length $l_0 = l_a = l_b$, so that $\tau_0 = \tau_a = \tau_b$. In this case, we have:

$$\varphi(t - (2\tau_z + \tau_a)) - \varphi(t - \tau_b) = -2\gamma\tau_z(t - (2\tau_z + \tau_0)) - 2\omega_0\tau_z \tag{2.17}$$

Thus, Eq. (2.14) is now reduced to

$$I_p^{AC}(t) = \frac{T_p^2 A_a A_b^*}{4} \sum_z \left(e^{-\alpha(2l_z+2l_0)} r_p(z) E_0\left(t - (2\tau_z + \tau_0)\right) E_0^*\left(t - \tau_0\right) \right.$$
$$\left. \times e^{-j\left(2\gamma\tau_z(t-(\tau_z+\tau_0))+2\omega_0\tau_z\right)} \right) + c.c., \tag{2.18}$$

where $c.c.$ denotes the complex conjugate of the first term. If output of the TLS is stable over long period of time, then $E_0\left(t - (2\tau_z + \tau_0)\right) \approx E(t)$ and $E_0^*\left(t - \tau_0\right) \approx E_0^*(t)$. Eq. (2.18) becomes

$$I_p^{AC}(t) = \frac{T_p^2 A_a A_b^*}{4} \sum_z \left(e^{-\alpha(2l_z+2l_0)} r_p(z) E_0(t) E_0^*(t) e^{-j\left(2\gamma\tau_z(t-(\tau_z+\tau_0))+2\omega_0\tau_z\right)} \right) + c.c., \tag{2.19}$$

where $c.c.$ denotes the complex conjugate of the first term. Let's group all phase terms related OFDR optical frequency tuning and Rayleigh back-scattering:

$$\Theta_p(z) = 2\tau_z(\omega_0 - \gamma\tau_z(\tau_z + \tau_0)) - \theta_{r_p(z)}, \tag{2.20}$$

Factoring out complex amplitude constants, we have:

$$m_p(t) = |m_p(t)| \cdot e^{j\psi_p(t)} = \frac{T_p A_a A_b^*}{4} |E_0(t)|^2 \tag{2.21}$$

Eq. (2.19) can be now expressed as

$$I_p^{AC}(t) = \sum_z \left(|r_p(z)| \cdot |m_p(t)| e^{-j\left(2\gamma\tau_z t + 2\tau_z\left(\omega_0 - \gamma\tau_z(\tau_z+\tau_0)\right)\right) + \psi_p(t) - \theta_{r_p(z)}} \right) + c.c.$$
$$= 2\sum_z \left(|r_p(z)| \cdot |m_p(t)| e^{-2\alpha\left(l_z+l_0\right)} \cos\left(2\gamma\tau_z t + 2\tau_z\left(\omega_0 - \gamma\tau_z\left(\tau_z + \tau_0\right)\right) + \psi_p(t) - \theta_{r_p(z)}\right) \right)$$
$$= 2\sum_z \left(|r_p(z)| \cdot |m_p(t)| e^{-2\alpha\left(l_z+l_0\right)} \cos\left(2\gamma\tau_z t + \psi_p(t) + \Theta_p(z)\right) \right)$$
$$= \sum_z \left(m_p(t,z) \cos\left(2\gamma\tau_z t + \psi_p(t) + \Theta_p(z)\right) \right), \tag{2.22}$$

where $m_p(t,z) = |r_p(z)| \cdot |m_p(t)| e^{-2\alpha(l_z + l_0)}$ is the magnitude of measured field intensity, and $r_p(z) = |r_p(z)| \cdot e^{j\theta r_p(z)}$ is a complex reflection coefficient owing to Rayleigh back-scattering at coordinate z. Assuming that strain and temperature fields applied to the FUT are quasi-static (e.g. strain and temperature distributions along the fiber stay constant during a single OFDR measurement), $m_p(t,z) \approx m_p(z)$ and $\psi_p(t) = 0$. Finally, Eq. (2.22) turns into

$$I_p^{AC}(t) = \sum_z m_p(z) \cos\left(2\gamma\tau_z t + \Theta_p(z)\right). \tag{2.23}$$

Fourier transform of Eq. (2.23) yields

$$I_p^{AC}(\omega) = \frac{\sqrt{2}\pi}{2} \sum_z m_p(z) \left(e^{j\Theta p(z)} \delta\left(\omega - 2\gamma\tau_z\right) + e^{-j\Theta p(z)} \delta\left(\omega + 2\gamma\tau_z\right)\right) \tag{2.24}$$

Since generation of only positive frequencies is physically feasible, only the first summand in Eq. (2.24) is considered for reflectance measurement:

$$I_p^{AC}(\omega) = \frac{\sqrt{2}\pi}{2} \sum_z m_p(z) e^{j\Theta p(z)} \delta(\omega - 2\gamma\tau_z) = \sum_z \kappa(z) \delta(\omega - 2\gamma\tau_z) \tag{2.25}$$

where $\kappa(z)$ defines local reflection coefficient that accounts for reflections from optical components and for Rayleigh back-scattering, and $\delta(\omega - 2\gamma\tau_z)$ is an impulse function specifying the beat frequency $\omega_z = 2\gamma\tau_z$ directly related to a position z along the fiber. Thus, as explained in the previous section, optical fiber under test is indeed treated as superposition of point reflections along its length when OFDR technique is used. Similar results can be obtained for the $\hat{s}$ component of the electric field registered by the photodetector PD2. Then two measurements will be combined together to provide the total power of back reflected field at each point along the FUT.

2.5 Strain sensing approach based on detection of physical shifts of point-like reflectors

Flowchart of conventional algorithm for strain sensing using OFDR reflectance data [53] is presented in Fig. 2.6. Baseline measurement B of size L is taken prior to applying any displacements to the FUT. The second measurement M is acquired when the FUT or some of its sections are strained. Both B and M are then windowed by a moving rectangular window w, and are partitioned

into s cropped segments. Note that windows may or may not overlap depending on how many points for measuring strain the user wants to assign.

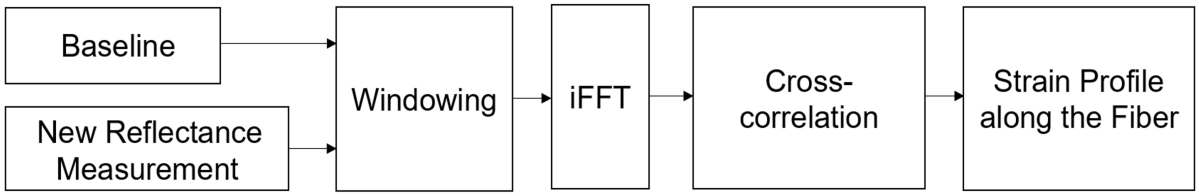

Figure 2.6: Conventional approach for strain measurement using OFDR.

Windowing operation is described by Eq. (2.26) and Eq. (2.27):

$$\hat{B}_s[k] = B[k]w[k - l \cdot s], \tag{2.26}$$

$$\hat{M}_s[k] = M[k]w[k - l \cdot s], \tag{2.27}$$

where B is the baseline, M is reflectance measurement in a strained state of FUT, l is window shift (in samples), and s is an index of windowed segment. Window w is defined as:

$$w[k] = Rect\left[\frac{k - X}{N}\right] = u\left[k - X + \frac{N}{2}\right] - u\left[k - X - \frac{N}{2}\right], \tag{2.28}$$

where X is window's center (usually $X = \frac{N}{2}$), N is window's length in points (even positive integer), $u[k]$ is the Heaviside step function. Note that depending on how much overlap between neighboring windows is required, $l \in [1, N + 1]$, hence the maximal number of partitioning segments ranges from $\left\lfloor \frac{L}{N} \right\rfloor$ to $L - N$.

Windowed segments are transferred back to the wavenumber domain by applying the inverse discrete Fourier transform (iDFT):

$$b_s[n] = \frac{1}{N} \sum_{k=0}^{N-1} \hat{B}_s[k] e^{j\frac{2\pi kn}{N}}, \tag{2.29}$$

$$m_s[n] = \frac{1}{N} \sum_{k=0}^{N-1} \hat{M}_s[k] e^{j\frac{2\pi kn}{N}}, \tag{2.30}$$

where $n = 0, 1 \ldots N-1$. Note that fast inverse Fourier transform (iFFT) is used in actual computations to speed-up the algorithm.

Wavenumber shift between the obtained signals is calculated using cross-correlation as

$$R_{bm}^{(s)}[h] = \sum_{n=-\infty}^{\infty} b_s[n] m_s[n-h], \tag{2.31}$$

$$P_s = \underset{h}{\operatorname{argmax}} \left(R_{bm}^{(s)}[h] \right), \tag{2.32}$$

where $R_{bm}^{(s)}$ is the cross-correlation coefficient in wavenumber space, and P_s is the shift that is experimentally calibrated to strain ε_s in the FUT.

In this dissertation, an alternative approach for strain measurement is proposed. The corresponding flowchart is demonstrated in Fig. 2.7. The main difference between Fig. 2.6 and Fig. 2.7 is the absence of the iFFT. Instead, the cross-correlation is directly applied to windowed reflectance data. Hence, the algorithm detects mechanical shifts of local scatterers rather than modulations of wavenumber.

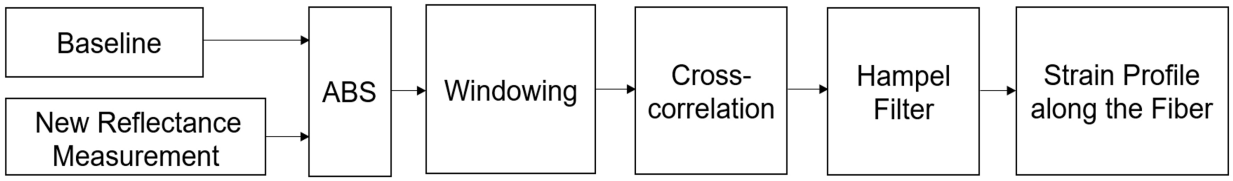

Figure 2.7: Alternative approach for strain measurement using OFDR.

Signal processing approach shown in Fig. 2.7 does not require phase information, and provides displacement measurement directly, if $x-$axis of reflectance measurement is mapped accurately to spatial coordinates along the FUT:

$$R_{BM}^{(s)}[h] = \sum_{k=-\infty}^{\infty} \left| \hat{B}_s[k] \right| \cdot \left| \hat{M}_s[k-h] \right|, \tag{2.33}$$

where $R_{BM}^{(s)}$ is the cross-correlation coefficient in spatial domain. Local displacement D_s is given by the following expression

$$D_s = \underset{h}{\operatorname{argmax}} \left(R_{BM}^{(s)}[h] \right) \tag{2.34}$$

Finally, strain in each fiber segment can be easily calculated as

$$\varepsilon_s = \frac{D_s}{N} \tag{2.35}$$

If OFDR reflectance measurements are corrupted with noise, computed displacement vector is passed through the Hampel filter as shown in Fig. 2.7. The filter uses the three-sigma rule of statistics to remove outliers from the signal. For a given sequence $x_1, x_2, ...x_n$ and a sliding window of length k, the following condition is evaluated:

$$\left|x_i - m_i\right| > n_\sigma \sigma_i, \tag{2.36}$$

where m_i is the local median, σ_i is the standard deviation, and n_σ is the threshold specified by user. the local median and standard deviation are defined as

$$m_i = median\left(x_{i-k}, x_{i-k+1}, ...x_i, ..., x_{i+k-1}, x_{i+k}\right), \tag{2.37}$$

$$\sigma_i = \kappa \cdot median\left(\left|x_{i-k} - m_i\right|, ..., \left|x_{i+k} - m_i\right|\right), \tag{2.38}$$

where coefficient $\kappa = \frac{1}{\sqrt{2} \cdot Efrc^{-1} \cdot \frac{1}{2}} \approx 1.4826$. If condition in Eq. (2.36) is met, the Hampel filter declares x_i an outlier and replaces it with m_i.

2.6 Validation of signal processing technique for strain sensing using OFDR

Measurements of Rayleigh back-scattered radiation in single mode (SM) optical fibers were performed at General Photonics Corporation (Chino, CA) using the polarization analyzing OFDR system PA-OFDR-1000. This section presents data acquisition approach and signal processing technique for calculating displacements and strains induced in the fiber. Experimental setup for validating the OFDR system is shown in Fig. 2.8. PA-OFDR-1000 unit was connected to Agilent 81607A tunable light source, and the whole setup was controlled from a lap-top with LabView drivers. Agilent TLS were driven at a scanning rate of 20 nm/s, and the wavelength tuning range spanned from 1500 nm to 1580 nm that provided spatial resolution of approximately 20 μm, when interrogating SM optical fibers. Output power of the TLS was approximately 3 mW. Optical fiber under test consisted of three sections: an SM fiber (1 m long), a piezoelectric fiber stretcher FST-005 (with 35 m long fiber inside), and an SM fiber with 500 continuously written Bragg-gratings (8 m long). Fiber stretcher was used to introduce nearly uniform strains in the corresponding section of the FUT. FST-005 was controlled by a DC voltage source and piezo-amplifier that supplied up to

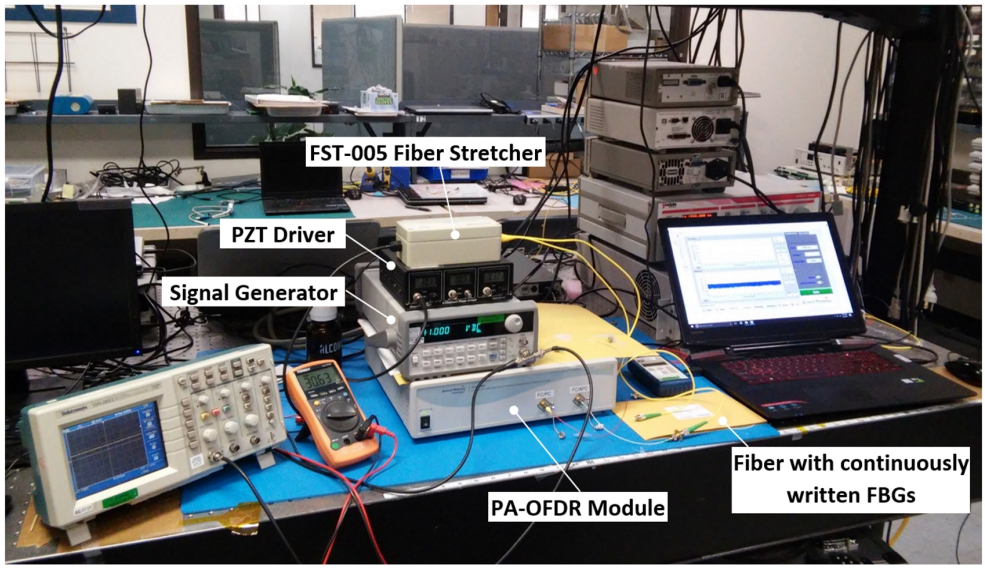

Figure 2.8: OFDR experimental setup at General Photonics Corporation.

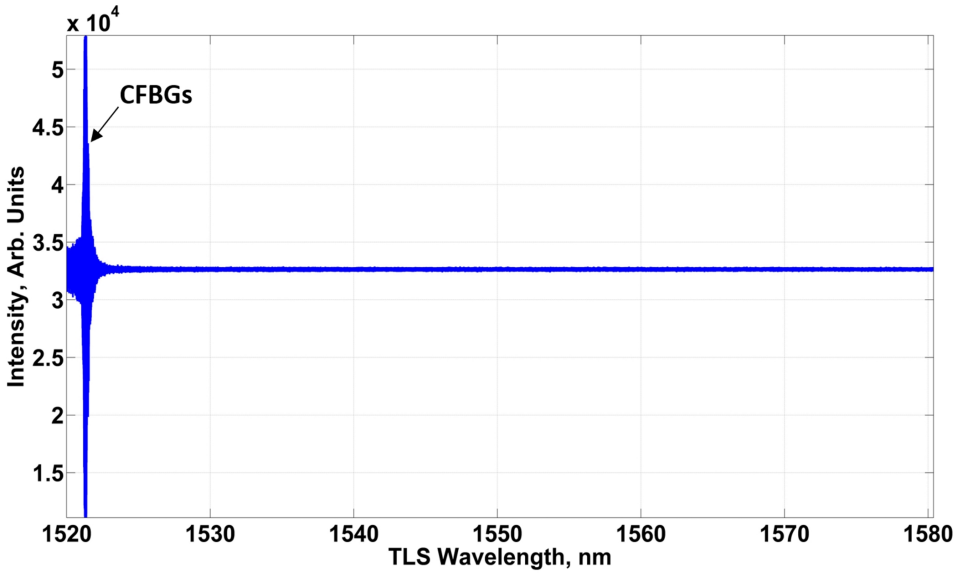

Figure 2.9: Radiation intensity sensed by photodetector PD1 ($\hat{s}$-polarized component).

300 V to the PZT crystal around which the fiber was wounded inside the instrument. All sections of FUT were connected with angle physical contact (APC) connectors. Fig. 2.9 demonstrates typical intensities of fringe patterns registered by the photodetectors and sampled by embedded high-speed DAQ inside the PA-OFDR-1000 module. The signal was averaged 8 times. As seen from Fig. 2.9, strong beating is observed around 1522 *nm*, which corresponds to Bragg wavelengths of continuously written FBGs at the end of the FUT. Note that signal presented in Fig. 2.9 contains

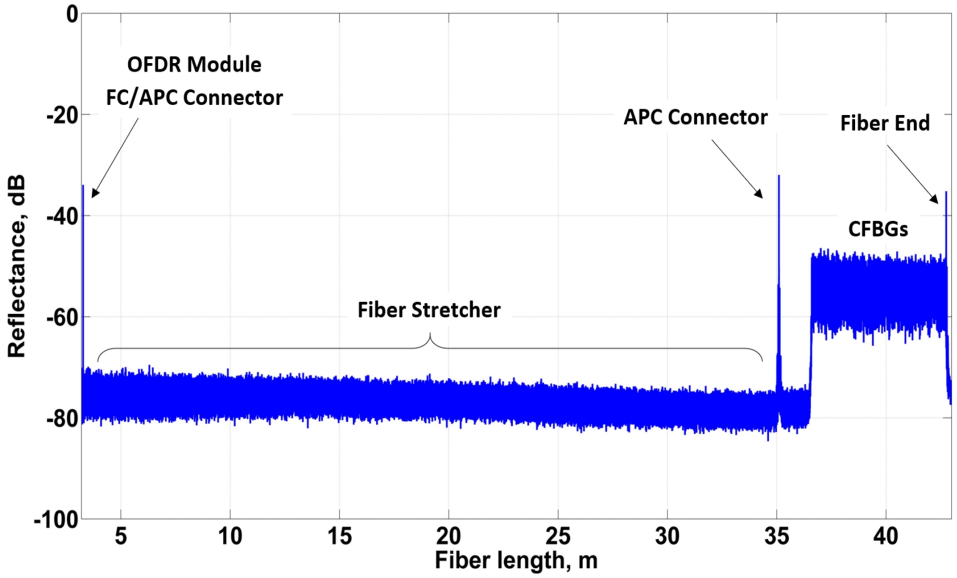

Figure 2.10: Typical OFDR measurement showing reflectance of FUT: single mode fiber, PZT fiber stretcher and optical fiber with CBFGs.

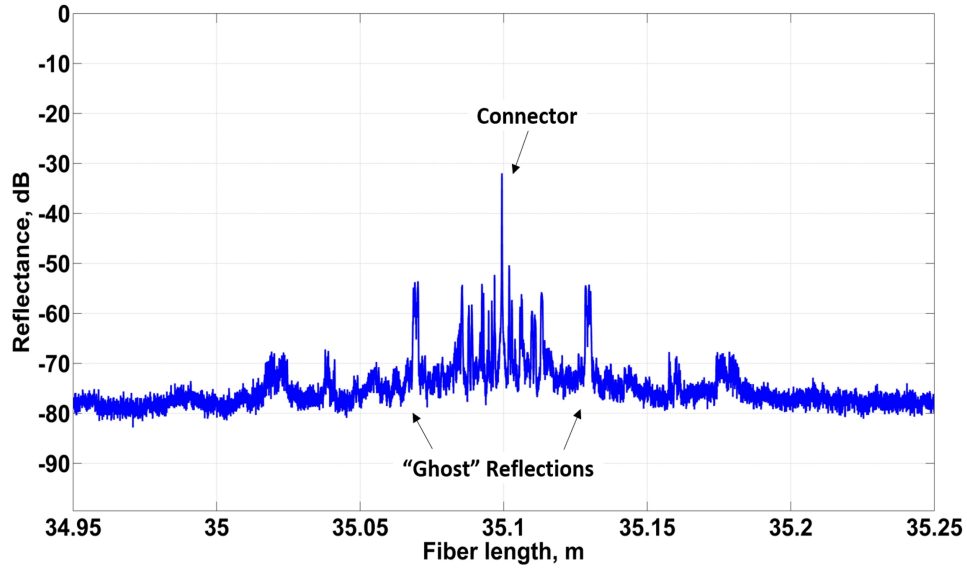

Figure 2.11: Fresnel reflection at APC connector.

approximately $8 \cdot 10^6$ data points. Fast Fourier transform of the beat signal shown in Fig. 2.9 provides reflectance along the FUT length. Fig. 2.10 demonstrates Rayleigh back-scattering from the optical fiber inside the FST-005 stretcher, reflections from CFBGs and APC connectors. Also, the x-axis of Fig. 2.10 starts at approximately 3.3 m in order not to show reflections from fibers inside the OFDR unit itself.

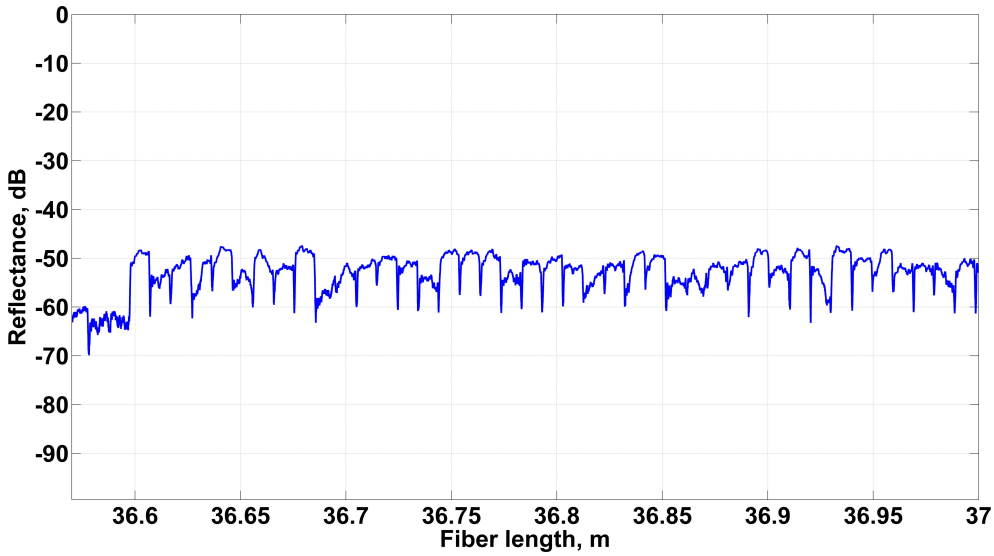

Figure 2.12: Reflections from continuously written Bragg-gratings.

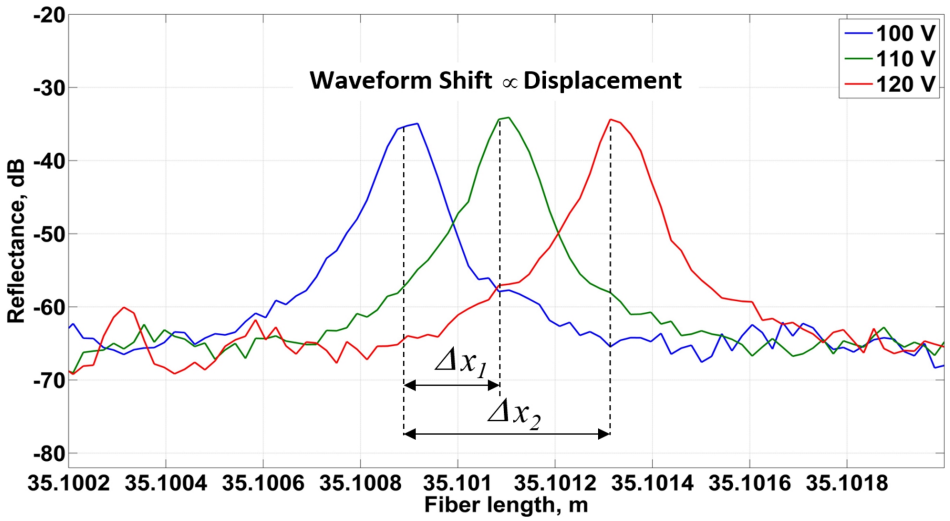

Figure 2.13: Shift of reflection from APC connector at different strain states.

Fig. 2.12 illustrates typical reflections from Bragg-gratings in the last 8-m section of the FUT. As results demonstrate, reflectivity of different Bragg-gratings varies up to 5 dB, but their period remains constant. Fig. 2.11 is a another version of Fig. 2.10 zoomed into the region around the APC connector. Fig. 2.11 reveals that some side lobes or "ghost" reflections are present near the true peak. This issue is caused by non-constant TLS tuning rate γ, and can be compensated for by applying the deskew filter, non-uniform Fourier transform or other advanced signal processing techniques.

Fig. 2.13 shows the effect of uniform displacement field applied to the FUT section by the FST-005 piezoelectric fiber stretcher. Fig. 2.13 is centered around the reflection from the APC connector on the output of FST-005. Two increased voltages (w.r.t. initial voltage of 110 V) on the inputs of FST-005 generated higher strains in the fiber, which resulted in physical shifts of point-like Rayleigh reflectors, Δx_1 and Δx_2, respectively.

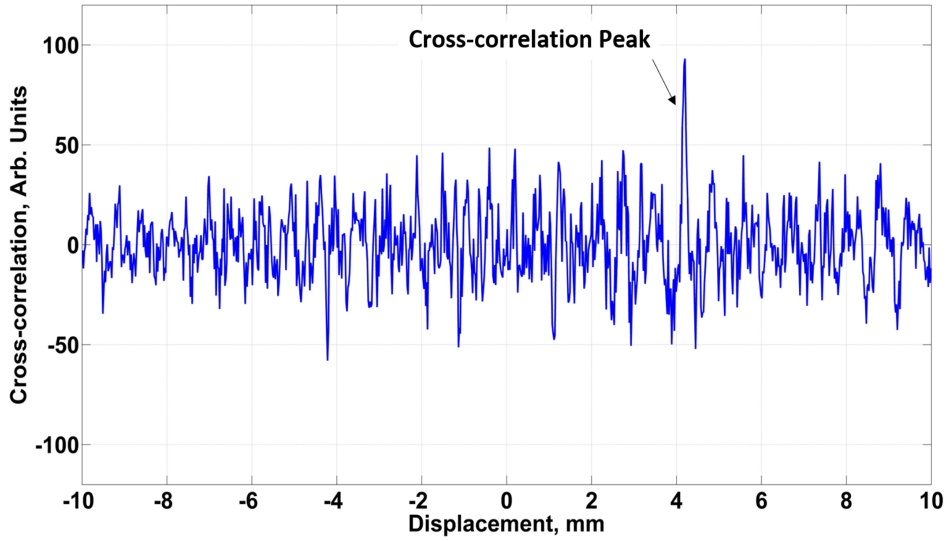

Figure 2.14: Cross-correlation of segments of back-scattering profile at the end of the fiber stretcher. Baseline reflectance measurement is compared to a measurement after applying 190 V to the input of FST-005.

Hence, it was concluded that identifying shifts of local Rayleigh back-scattered radiation patterns should help recover displacement along the whole FUT length. This was easily implemented by partitioning the reflectance measurement in small segments (windows) and by calculating local cross-correlations with respect to baseline measurement in undisturbed state of the FUT as per Eq. (2.33). This simple approach was notably different from commonly used technique where the same segmentation is applied, but the cross-correlation is performed in the K-space by taking the inverse FFT first.

OFDR measurements were acquired for 23 different strain states in subsequent experiments. Reflectance profiles (see Fig. 2.10) were segmented into 12-mm long windows. Then the cross-correlations were computed for all windows with respect to a baseline measurement in a strain-free

state, when the fiber stretcher was turned off. Windows were also allowed to have 50% overlap for smoother output. Typical cross-correlation between windowed section of the FUT at the end of the fiber stretcher in the strained state and strain-free state is presented in Fig. 2.14. In this case, nearly 4-*mm* reflector displacement was detected, when 190 *V* were applied to the FST-005.

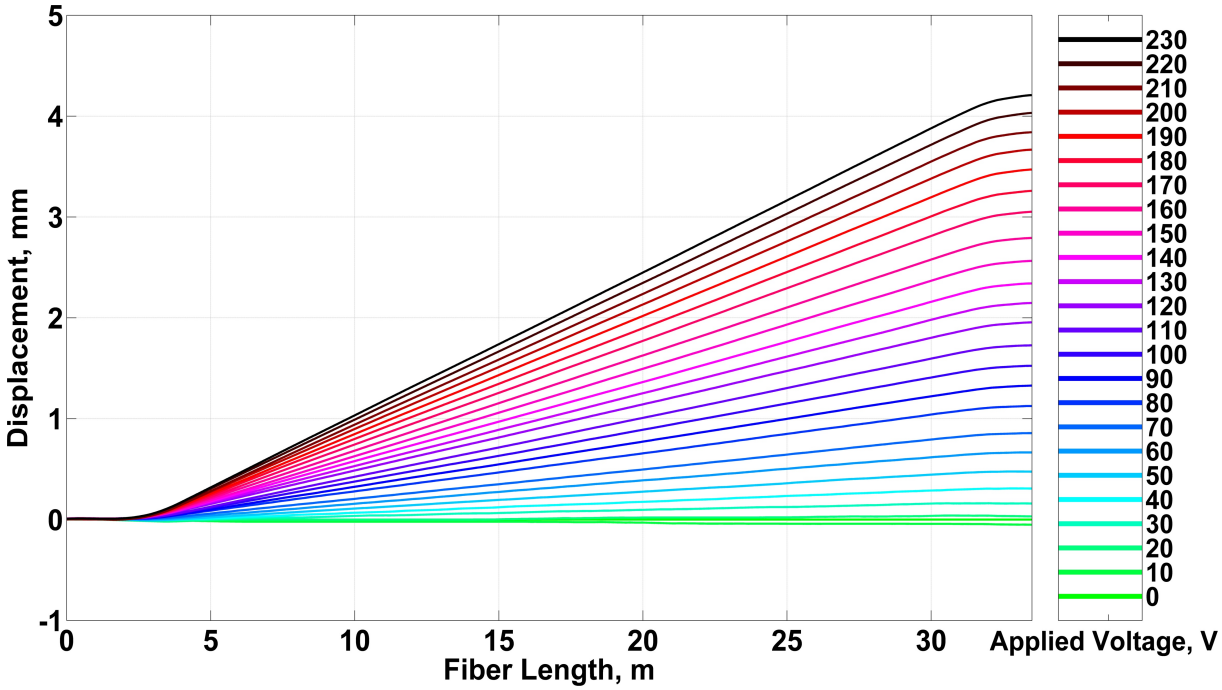

Figure 2.15: Displacement profiles along the 35-*m* long optical fiber section inside the FST-005 fiber stretcher.

Applying the same signal processing procedure to a complete set of 23 OFDR measurements allowed for recovering of respective displacement profiles along the FUT length as shown in Fig. 2.15. Obtained results agreed perfectly with factory specifications of FST-005. It should be noted that calculated displacements had some spurious single-point spikes, apparently caused by measurement noise that shifted cross-correlation peaks to wrong locations. These spikes were successfully removed with a Hampel filter. Based on displacement profiles shown in Fig. 2.15, corresponding strain profiles were calculated (see Fig. 2.16).

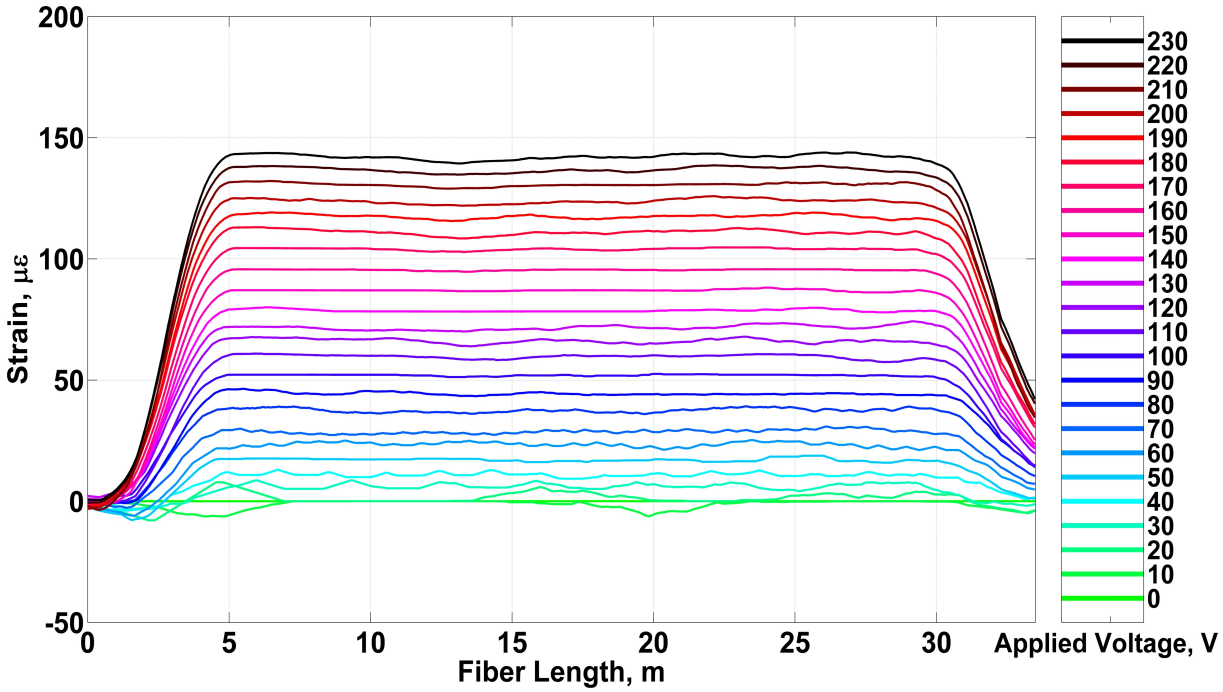

Figure 2.16: Strain profiles along the 35-*m* long optical fiber section inside the FST-005 fiber stretcher.

2.7 Conclusions

Chapter II described the development of advanced signal processing techniques for distributed displacement and strain sensing in SM fibers using the OFDR. An approach for measuring strain using Rayleigh back-scattering was proposed. In contrast to conventional techniques that detect applied axial strain as a modulation of wavenumber, reflectance measurements were analyzed in spatial domain, and local displacements along FUT were identified as shifts of point-like scatterers. The new signal processing technique was successfully validated using the PA-OFDR-1000 system at General Photonics Corporation. In the experimental setup, one section of the FUT had the piezoelectric fiber stretcher that introduced nearly uniform axial strain, which was accurately measured by the algorithm with a 4-mm spatial resolution. In addition, the acquired measurements were denoised that allowed to use reflectance data with less averaging. Overall, the obatined results demonstrated that the OFDR technique along with advanced signal processing is a promising tool for NDE and SHM of composite structures.

CHAPTER 3

HYBRID ACOUSTO-OPTIC HEALTH MONITORING OF STRUCTURAL COMPOSITES USING GUIDED WAVES AND CFBG-FPI SENSORS

3.1 Proposed approach for hybrid acousto-optic SHM

Rapid and cost-effective damage detection using multiple sensing techniques is one of the emerging paradigms in SHM. This chapter is focused on developing a novel hybrid approach for SHM of structural composites that combines benefits of ultrasonic and optical sensing. The proposed work uses use current successes in aforementioned techniques as launch-pad to propel the development of a new system that will utilize reusable surface-bonded or embedded arrays of optical fibers with strategic ability to sense ultrasonic guided waves. The synergy of this hybrid approach aims at eliminating the limitations of each of the approach while making it cost-effective and reusable.

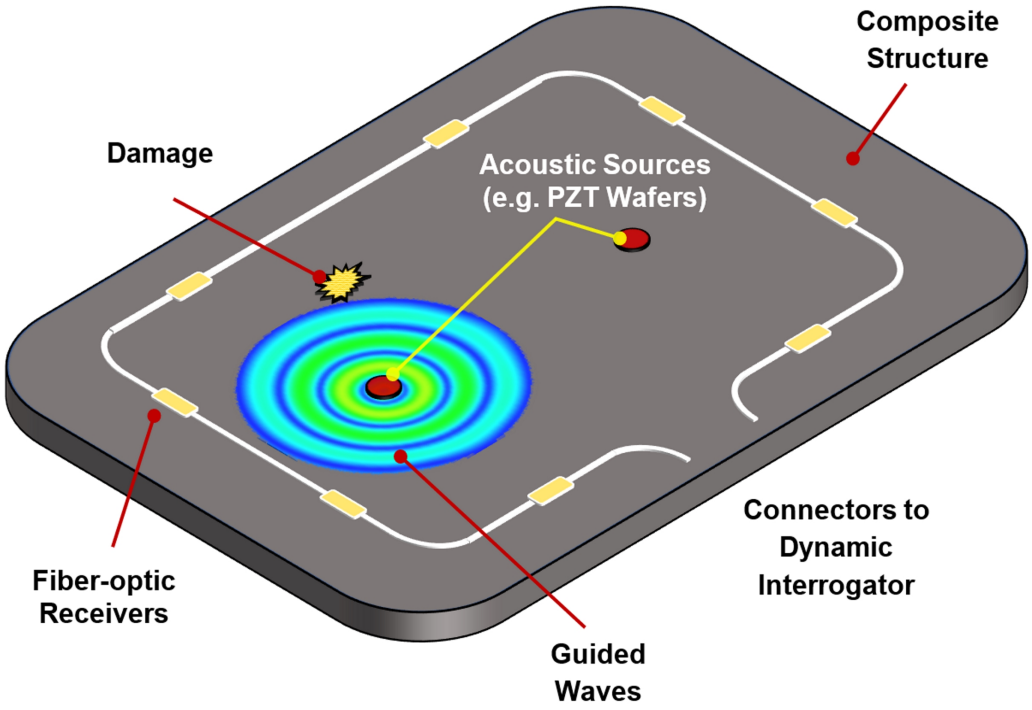

Figure 3.1: Overall approach for hybrid acousto-optic SHM of structural composites.

The overall approach proposed in this work is schematically shown in Fig. 3.1. Arrays of Fabry-Perot interferometric sensors formed by pairs of chirped fiber Bragg-gratings (CFBG-FPI) are surface-mounted or embedded in safety critical areas of composite structure [54]. Guided waves (GW) are excited by active sources, such as thin surface-bonded PZT wafers or external devices for non-contact generation of ultrasound (e.g. air-coupled transducers or a laser) and are sensed by CFBG-FPI receivers. In a passive mode, CFBG-FPI sensors are used for in-situ monitoring of slowly varying strains, loads or temperature changes in the host structure. In contrast, when the active mode is triggered for event-based or schedule-based inspection, guided waves are excited and CFBG-FPI interrogator is switched to the high-sampling rate regime. The system is controlled through the onboard PC, and pre-programmed signal processing algorithms are used on the acquired data for identifying damage signatures. Potential advantages of the proposed hybrid acousto-optic SHM approach are summarized in Fig. 3.2. The detailed descriptions of GW theory and GW sensing with CFBG-FPIs are given in the following sections, since the SHM approach is experimentally validated for cases of defect detection in aluminum plates.

3.2 Guided wave theory

This section introduces the fundamental equations describing guided waves in isotropic plate-like structures. Since the topic is well documented in the literature, only the key results are presented. The constitutive relations describing guided waves in plates can be thought of as a special case of elastic wave propagation in unbounded media. The differential equation of motion in three-dimensional solids is known as Navier's equation [55]:

$$\begin{aligned}
\mu(\frac{\partial}{\partial x^2}+\frac{\partial}{\partial y^2}+\frac{\partial}{\partial z^2})u_x+(\lambda+\mu)\frac{\partial}{\partial x}(\frac{\partial}{\partial x}+\frac{\partial}{\partial y}+\frac{\partial}{\partial z})u_x &= \rho\frac{\partial u_x}{\partial t^2}\\
\mu(\frac{\partial}{\partial x^2}+\frac{\partial}{\partial y^2}+\frac{\partial}{\partial z^2})u_y+(\lambda+\mu)\frac{\partial}{\partial x}(\frac{\partial}{\partial x}+\frac{\partial}{\partial y}+\frac{\partial}{\partial z})u_y &= \rho\frac{\partial u_y}{\partial t^2}\\
\mu(\frac{\partial}{\partial x^2}+\frac{\partial}{\partial y^2}+\frac{\partial}{\partial z^2})u_z+(\lambda+\mu)\frac{\partial}{\partial x}(\frac{\partial}{\partial x}+\frac{\partial}{\partial y}+\frac{\partial}{\partial z})u_z &= \rho\frac{\partial u_z}{\partial t^2}
\end{aligned} \tag{3.1}$$

Unique Features of the Proposed Hybrid Acousto-Optic SHM

✓ Remote damage detection by FBGs

- Limitations of FBG (detecting strains in the vicinity of the grating) is overcome by synergy with GW

✓ Multiplexed FBG sensors & reduced number of wires

- Multiple FBG sensors can be inscribed in the same fiber and selectively interrogated using Wavelength Division Multiplexing (WDM). This helps reduce the number of wires compared to other distributed SHM arrays.

✓ Flexibility in sensor deployment

⊕ **Strategically embedded FBG arrays**

- Measurement within "thin" bond-lines & inter-laminar areas without affecting their intrinsic properties or creating flaws and associated stress concentrations is 'only' possible with FBGs.
- Critical components that govern the structural integrity of the entire structure, namely 'joints' can be monitored efficiently with this technique.

⊕ **Multi-use and cost-effective surface mounted FBGs**

- Bonding FBGs on external surfaces/substrates using reversible adhesives allows for re-using FBGs. Reversible adhesive technology developed at MSU allows for targeted heating/melting of thermoplastic adhesive that holds the FBGs.
- Enables easy sensor placement, repair and replacement upon damage (if any)

✓ Directionally sensitive FBG arrays

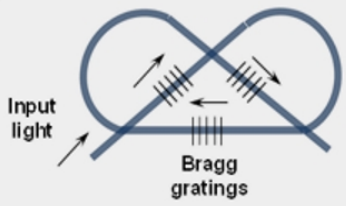

⊕ FBG sensors are highly directive and local. Obtaining a 'stress-state' at interfaces and bond-lines is possible using rosette configuration.

- Wave propagation vector can be reconstructed.
- Discriminates measured strains from temperature variations using self-calibrating properties.

✓ Data Fusion using Passive & Active measurements

- Enables elimination of disturbance factors (e.g. load & temperature) on GW signals, generated with acoustic sources coupled with structure (e.g. PZT).
- Increases robustness of the system.

Figure 3.2: Unique features of the proposed hybrid acousto-optic SHM.

Eq. (3.1) can be concisely expressed in vector form:

$$\mu\nabla^2\mathbf{u} + (\lambda + \mu)\nabla(\nabla \cdot \mathbf{u}) = \rho\frac{\partial \mathbf{u}}{\partial t^2} \tag{3.2}$$

where $\mathbf{u} = \mathbf{i}u_x + \mathbf{j}u_y + \mathbf{k}u_z$ is the particle displacement vector, ρ is the material density, μ and λ are the Lame constants, the ∇ is a *del* differential operator and ∇^2 is a vector Laplacian.

It should be noted that Navier's differential equations governing wave propagation are based upon three fundamental relationships from linear elasticity theory. These include strain-displacement relations (Eq. (3.3)), equation of motion also known as Newton's generalized second law (Eq. (3.4)) and constitutive stress-strain relations or Hooke's law (Eq. (3.5)). Their expressions in tensor notation are:

$$\epsilon_{ij} = \frac{1}{2}(u_{j,i} + u_{i,j}) \tag{3.3}$$

$$\frac{\partial \sigma_{ij}}{\partial x_i} = \rho\frac{\partial u_i}{\partial t^2} \tag{3.4}$$

$$\sigma_{ij} = c_{ijkl}\epsilon_{kl} \tag{3.5}$$

where $i, j = 1, 2, 3$; ϵ_{ij} – the strain tensor and c_{ijkl} – the stiffness tensor; repeated indexes imply summations and commas imply partial derivatives.

Therefore, Navier's equation combines three equilibrium equations, six strain-displacement equations, and six constitutive equations from Eq. (3.3)–Eq. (3.5). Navier's equation can be solved with the help of Helmholtz vector and scalar potentials $\mathbf{H}$ and Φ :

$$\mathbf{u} = \nabla\Phi + \nabla \times \mathbf{H} \tag{3.6}$$

$$\nabla \cdot \mathbf{H} = 0 \tag{3.7}$$

Upon the substitution of Eq. (3.5) and Eq. (3.6) into Eq. (3.1) we get

$$(\lambda + 2\mu)\nabla^2\Phi - \rho\nabla\ddot{\Phi} = 0 \tag{3.8}$$

$$\mu\nabla^2\mathbf{H} - \rho\ddot{\mathbf{H}} = 0 \tag{3.9}$$

The rearrangement of Eq. (3.8) and Eq. (3.9) yields the equation of wave propagation in 3D homogeneous solids in terms of scalar and vector potentials

$$\begin{aligned} c_l{}^2\nabla^2\Phi &= \ddot{\Phi} \\ c_s{}^2\nabla^2\mathbf{H} &= \ddot{\mathbf{H}} \end{aligned} \tag{3.10}$$

where $c_l = (2\mu + \lambda)/\rho$ and $c_s = \mu/\rho$. Double dot operator represents the second order time derivative. It can be shown that the total solution for displacement vector $\mathbf{u}$ has three components [55]:

$$\mathbf{u} = \mathbf{u_L} + \mathbf{u_{SH}} + \mathbf{u_{SV}} \tag{3.11}$$

where $\mathbf{u_L}$ corresponds to *longitudinal* or *pressure* wave whose particle displacement is parallel to the direction of propagation, $\mathbf{u_{SH}}$ and $\mathbf{u_{SV}}$ define the *shear horizontal* and *shear vertical* waves. Motion of particles for these solutions is perpendicular to the direction of wave propagation. The snapshots of S-wave and P-wave are shown in Fig. 3.3.

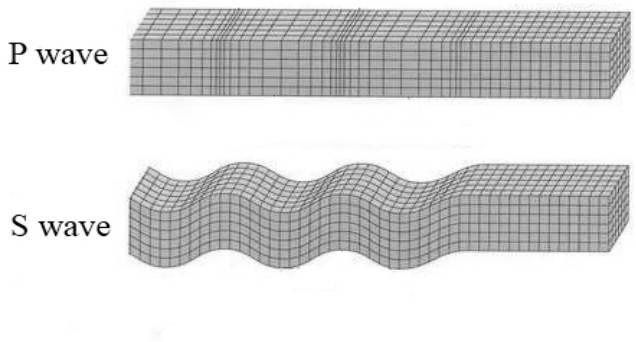

Figure 3.3: Shear vertical and pressure waves in solids.

Shear vertical and pressure wave solutions are of particular importance if Navier's equations are solved for practical cases when the structure has some geometric bounds. In particular, the interaction of shear vertical and pressure waves in thin plates and shells gives rise to guided waves. In this section we consider the derivation of Lamb wave equations for two-dimensional plates of infinite length. For simplicity of analysis it is possible to assume that the wave potentials are invariant to the z-direction along the wave front [55].

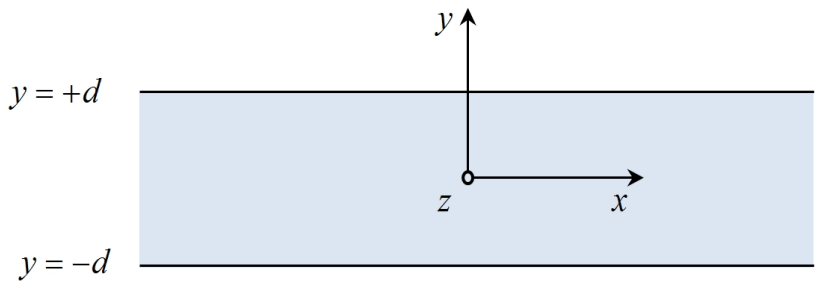

Figure 3.4: Isotropic plate of infinite length and thickness $2d$. Wave propagates in x-direction.

In this case $\partial/\partial z = 0$ and $\mathbf{u_{SH}}$ accepts only shear displacement u_z. In contrast, $\mathbf{u_L}$ with $\mathbf{u_{SV}}$ accept u_x and u_y displacements, which depend only on scalar potential Φ and a z-component of a vector potential H_z. Therefore, Navier's equation in terms of scalar and vector potentials for $\mathbf{u_L}$, $\mathbf{u_{SV}}$ possible solutions and the geometry in Fig. 3.4 takes the form:

$$\begin{cases} {c_l}^2 \nabla^2 \Phi = \ddot{\Phi} \\ {c_s}^2 \nabla^2 H_z = \ddot{H}_z \end{cases} \tag{3.12}$$

where c_l and c_s are longitudinal and shear wave speeds. Introducing the simpler notation $\Phi = \phi$ and $H_z = \psi$ we get a classical formulation for guided wave equations in the potential form:

$$\begin{aligned} \frac{\partial^2 \phi}{\partial x^2} + \frac{\partial^2 \phi}{\partial y^2} + \frac{\omega^2}{{c_p}^2}\phi = 0 \\ \frac{\partial^2 \psi}{\partial x^2} + \frac{\partial^2 \psi}{\partial y^2} + \frac{\omega^2}{{c_s}^2}\psi = 0 \end{aligned} \tag{3.13}$$

Assuming harmonic solution $e^{-i(\omega t - \xi x)}$, the system of equations Eq. (3.13) becomes:

$$\begin{aligned} \frac{\partial^2 \phi}{\partial y^2} + (\frac{\omega^2}{{c_p}^2} - \xi^2)\phi = 0 \\ \frac{\partial^2 \psi}{\partial y^2} + (\frac{\omega^2}{{c_s}^2} - \xi^2)\psi = 0 \end{aligned} \tag{3.14}$$

In Eq. (3.14), $\xi = \omega/c$ defines a wavenumber. At this point we can introduce the more compact notation for convenience:

$$\begin{aligned} p^2 = \frac{\omega^2}{{c_p}^2} - \xi^2 \\ q^2 = \frac{\omega^2}{{c_s}^2} - \xi^2 \end{aligned} \tag{3.15}$$

Hence,

$$\begin{aligned} \frac{\partial^2 \phi}{\partial y^2} + p^2 \phi = 0 \\ \frac{\partial^2 \psi}{\partial y^2} + q^2 \psi = 0 \end{aligned} \tag{3.16}$$

The general solution for the above system takes the form:

$$\begin{aligned} \phi = A_1 \sin py + A_2 \cos py \\ \psi = B_1 \sin qy + B_2 \cos qy \end{aligned} \tag{3.17}$$

where A_1, A_2, B_1 and B_2 are constants to be determined from the boundary conditions.

3.2.1 Symmetric solution

Symmetric solution implies that u_x component of the displacement vector and shear stresses are symmetric about the midplane across the thickness of the plate, namely

$$\begin{aligned} u_x(x,-d) &= u_x(x,d) & \tau_{yx}(x,-d) &= -\tau_{yx}(x,d) \\ u_y(x,-d) &= -u_y(x,d) & \tau_{yy}(x,-d) &= \tau_{yy}(x,d) \end{aligned} \tag{3.18}$$

Symmetric boundary conditions also include traction free surfaces

$$\begin{aligned} \tau_{yx}(x,-d) = -\tau_{yx}(x,d) = 0 \\ \tau_{yy}(x,-d) = \tau_{yy}(x,d) = 0 \end{aligned} \tag{3.19}$$

Using the general solution for potentials in Eq. (3.17) and formulas for displacements and stresses from the Appendix A, Eq. (3.19) can be expressed as

$$\begin{cases} -2i\xi A_2 \sin pd + B_1(\xi^2 - q^2) \sin qd = 0 \\ A_2(\xi^2 - q^2) \cos pd - 2i\xi B_1 \cos qd = 0 \end{cases} \tag{3.20}$$

A non-trivial solution for the above linear system of equations exists if the determinant in Eq. (3.20) vanishes:

$$\triangle_S = (\xi^2 - q^2)^2 \sin qd \cos pd + 4\xi^2 pq \cos qd = 0 \tag{3.21}$$

Rearranging Eq. (3.21) yields the dispersion relation for symmetric modes:

$$\frac{\tan pd}{\tan qd} = -\frac{(\xi^2 - q^2)^2}{4\xi^2 pq} \tag{3.22}$$

where p and q are given in Eq. (3.15).

3.2.2 Antisymmetric solution

Antisymmetric solution requires that displacements and stresses are antisymmetric with respect to the midplane

$$\begin{aligned} u_x(x,-d) &= -u_x(x,d) & \tau_{yx}(x,-h) &= \tau_{yx}(x,h) \\ u_y(x,-d) &= u_y(x,d) & \tau_{yy}(x,-h) &= -\tau_{yy}(x,h) \end{aligned} \tag{3.23}$$

The antisymmetric boundary conditions are the following

$$\begin{aligned} \tau_{yx}(x,-d) &= \tau_{yx}(x,d) = 0 \\ \tau_{yy}(x,-d) &= -\tau_{yy}(x,d) = 0 \end{aligned} \tag{3.24}$$

Using the general solution for the potentials in Eq. (3.17) and formulas for the displacements and stresses from the Appendix A, Eq. (3.24) can be expressed as

$$\begin{cases} 2i\xi A_1 \cos pd + B_2(\xi^2 - q^2)\cos qd = 0 \\ A_1(\xi^2 - q^2)\sin pd + 2i\xi B_2 \cos qd = 0 \end{cases} \tag{3.25}$$

A non-trivial solution exists if determinant in Eq. (3.25) vanishes:

$$\triangle_A = (\xi^2 - q^2)^2 \sin pd \cos qd + 4\xi^2 pq \cos qd \sin qd = 0 \tag{3.26}$$

Finally, we obtain Lamb wave equation for antisymmetric modes:

$$\frac{\tan pd}{\tan qd} = -\frac{4\xi^2 pq}{(\xi^2 - q^2)^2} \tag{3.27}$$

It can be noticed that the right-hand side of Eq. (3.22) is reciprocal to that of Eq. (3.27).

3.2.3 Phase velocity and group velocity dispersion curves

It can be noticed that solutions of Rayleigh-Lamb equations in Eq. (3.22) and Eq. (3.27) define the dispersion curves or the relationship between the phase velocity, c_{ph} and the actuation frequency, ω. Since p and q also depend on ω, the phase velocity should be evaluated numerically at each frequency step for a fixed value of a plate thickness $2h$.

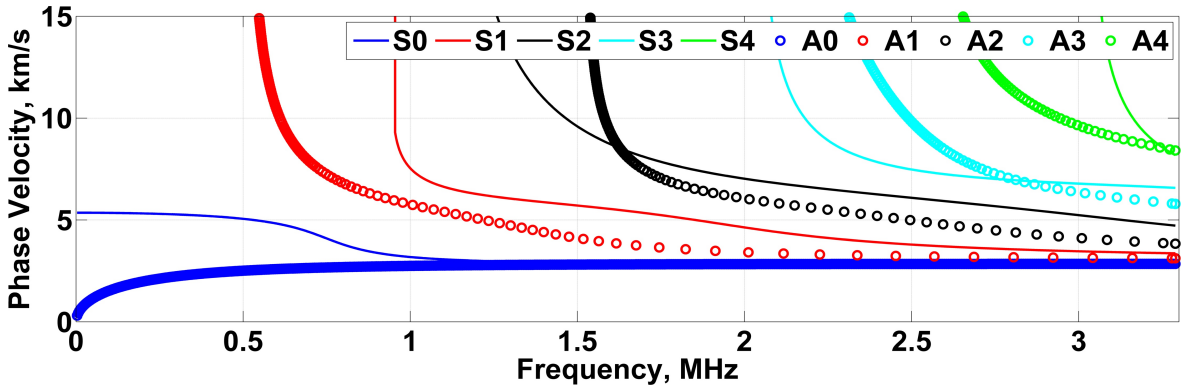

Figure 3.5: Phase velocity dispersion curves of 3-mm thick aluminum plate.

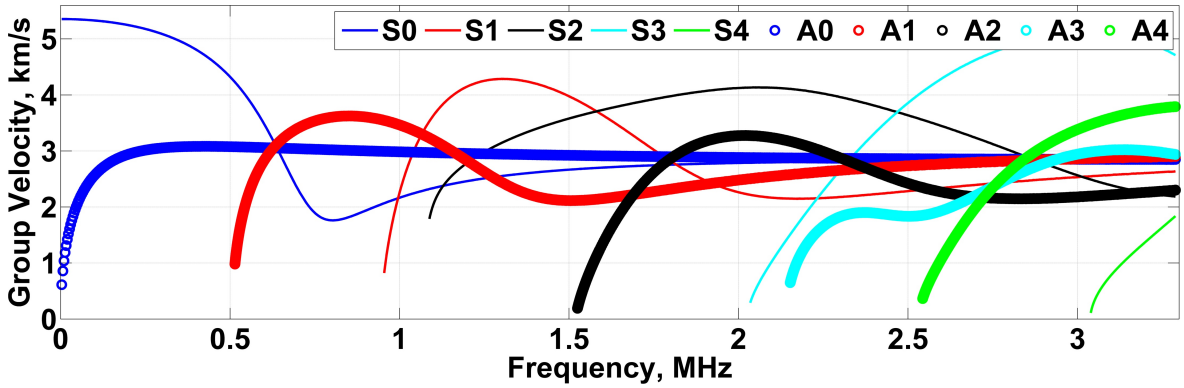

Figure 3.6: Group velocity dispersion curves of 3-mm thick aluminum plate.

$$c_{gr} = \frac{c^2}{c - fd\frac{\partial c}{\partial(fd)}} \tag{3.28}$$

The example of phase velocity dispersion curves is presented in Fig. 3.5. It follows that the solution is not unique, and at high frequency-thickness products multiple symmetric and antisymmetric modes exist in the plate. However, the knowledge of group velocity dispersion curves (Fig. 3.6) can be considered even more important, since the group velocity, c_{gr} determines how fast the wavefront of each mode propagates. This enables one to calculate the Time-of-Flight (ToF) and distance traveled by wave packets in the structure, which is essential for locating damage sites. Group velocity dispersion curves can be obtained from the phase velocity data using Eq. (3.28).

3.3 Detection of guided waves with FBG and CFBG-FPI sensors

Fiber Bragg-grating (FBG) sensors are manufactured by inscribing a systematic variation of refractive index into the core of the conventional optical fiber (see Fig. 3.7). Hence, an FBG is a sandwich-like distributed reflector, which acts as an optical filter that transmits the entire spectrum of the light source and reflects back the resonant Bragg wavelength, given by the following equation:

$$\lambda_B = 2n\Lambda \tag{3.29}$$

where n is the effective refractive index of the fiber core; and Λ is the period of Bragg-grating.

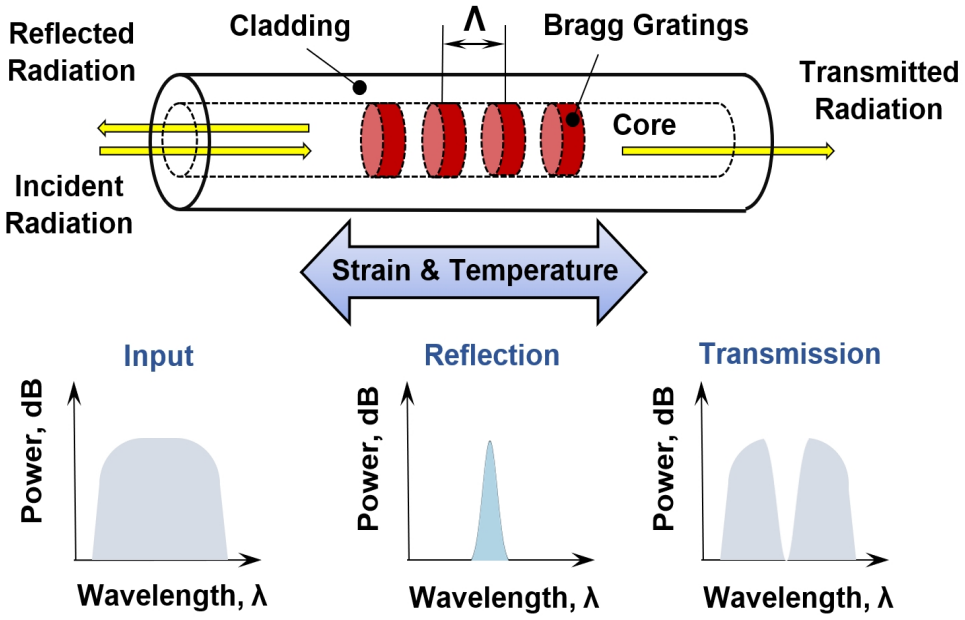

Figure 3.7: Operation principle of the fiber Bragg-grating sensor.

The sensor resolution is determined by the spectral bandwidth of the back-reflected radiation that depends on the effective refractive index of the fiber core and Bragg-grating period. As the strain inside the structure varies so does the spacing between the gratings, which results in a shift of the Bragg wavelength. Hence, the strain response of the FBG arises from both the physical elongation of the sensor and the change in effective fiber refractive index due to photoelastic effects. Similarly, a thermal response is driven by the inherent thermal expansion of the fiber material and the temperature dependence of the refractive index. The wavelength-encoded nature of the FBG

output provides a built-in self-referencing capability for the sensor. Since the wavelength is the fundamental parameter, the output does not depend directly on the total light levels, losses in the connecting fibers and couplers, or source power.

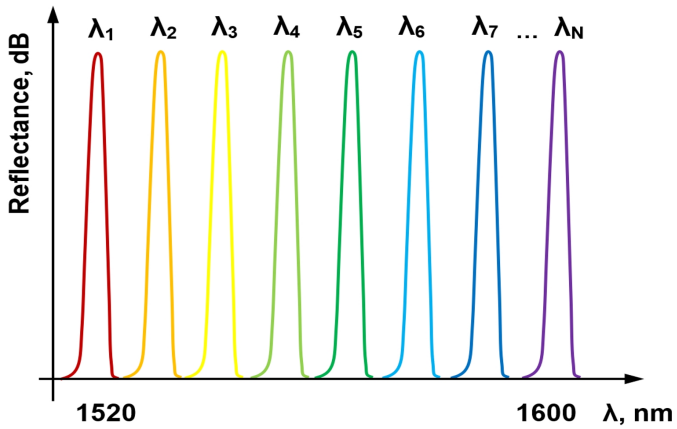

Figure 3.8: Principle of FBG wave division multiplexing.

Many FBG sensors in the same fiber can be interrogated using wave division multiplexing (WDM). In this case, all FBGs have unique Bragg wavelengths, and their corresponding reflectance spectra don't overlap as shown in Fig. 3.8. The dynamic interrogator is tuned on each Bragg wavelength in a round robin fashion to acquire all data.

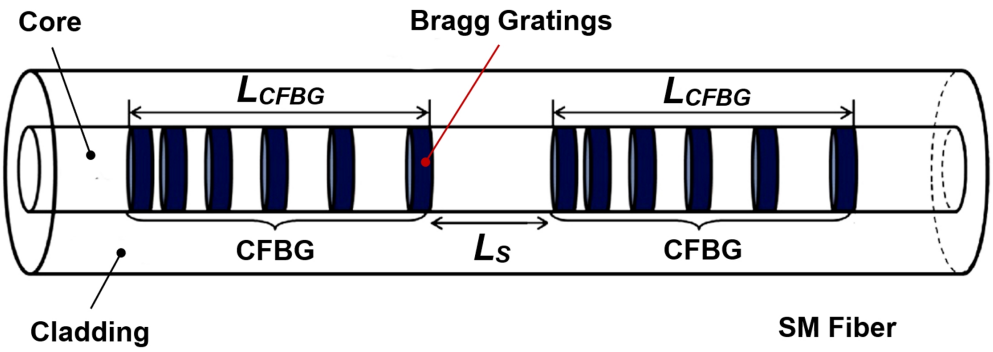

Figure 3.9: Design of the Fabry-Perot interferometer based on a pair of chirped fiber Bragg-grating sensors (CFBG-FPI).

Fabry-Perot (FP) cavities, which are realized by inscribing multiple FBGs in a single fiber, have wide applications in optical fiber communication systems, optical fiber sensing systems and photonic generation. The structure of Fabry-Perot interferometer based on chirped FBGs (CFBG-

FPI) is shown in Fig. 3.9. Two identical chirped FBGs of lengths L_{CFBG} are cascaded with a short offset L_S between them [54]. Typically, CFBG sensors feature wider reflectance spectrum than regular FBGs. Writing a pair of CFBGs in a sequence introduces approximately equally spaced fringes to the resulting reflectance spectrum as shown in Fig. 3.10(a). Free spectral range (FSR) of the fringes can be set by selecting the appropriate length, chirp rate and offset between the CFBGs. Similar to regular FBGs, the spectrum of radiation reflected by the CFBG-FPI will undergo wavelength shifts proportional to applied strain and/or temperature fields along the fiber.

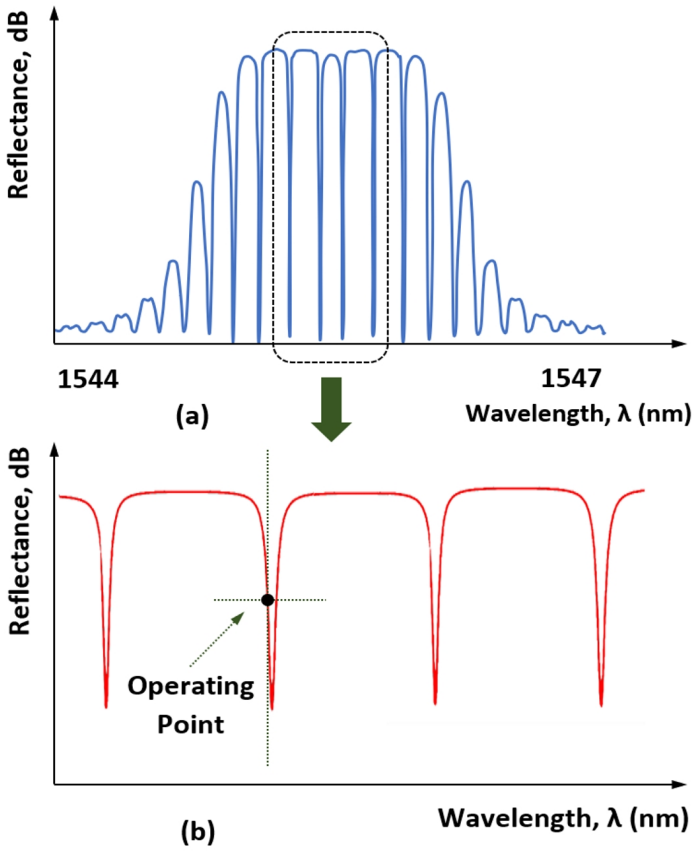

Figure 3.10: (a) Spectrum of radiation reflected from a CFBG-FPI sensor; (b) approach for high-resolution strain sensing by modulating the intensity of radiation back-reflected from CFBG-FPI.

Hence, a CFBG-FPI structure in the optical system can act as a filter that modulates the intensity of radiation reflected from it as a function of external thermo-mechanical input [54]. This concept is used in present work for dynamic detection of ultrasonic vibrations in aluminum plates. The approach for strain sensing using the CFBG-FPI is illustrated in Fig. 3.10(b). Once the CFBG-FPI

sensor has been strategically deployed on the structure, its reflectance spectrum is measured with Optical Spectrum Analyzer (OSA) to identify all notches. Then the tunable light source (TLS) is set to output monochromatic radiation with center wavelength at the midpoint of one of the edges of the sharpest notch. Applying strain to the CFBG-FPI will shift the position of the notch, thus modulating the intensity of reflected radiation. Sharpness of the notch and its magnitude will determine the sensitivity and linear range for GW detection.

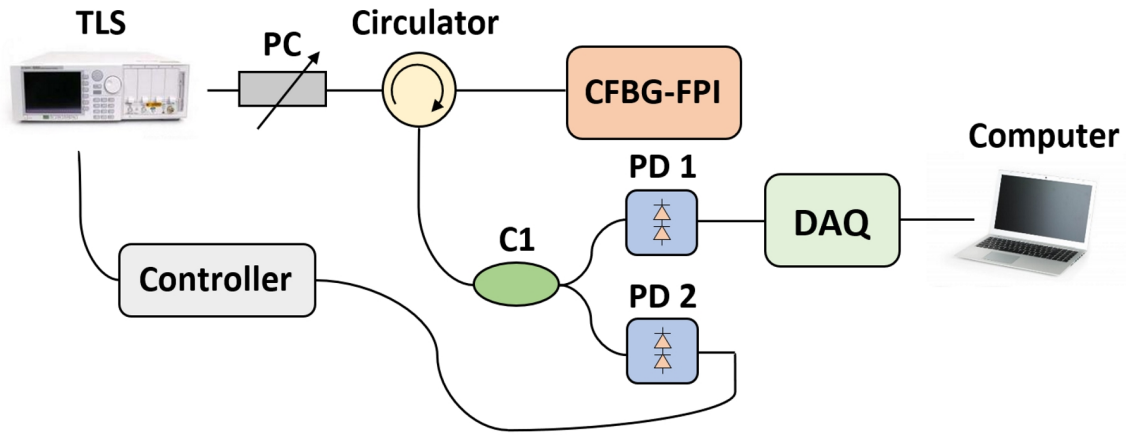

Figure 3.11: Block diagram of the setup for GW detection using surface-mounted CFBG-FPI sensors.

Fig. 3.11 shows a block diagram of the experimental setup based on a CFBG-FPI and laser-intensity demodulation with smart feedback control for detection of ultrasonic signals under large low-frequency background strains [54]. The TLS can be a low-cost semiconductor laser, such as a distributed feedback laser diode or a discrete mode laser diode, whose wavelength is tuned with high speed through current injection in a wavelength range slightly larger than the FSR of the CFBG-FPI. The laser is locked to one of the spectral notches within its tuning range for GW detection. Radiation from TLS propagates to CFBG-FPI through the single-mode fiber, polarization controller (PC) and circulator. PC is required to manually adjust the state of polarization (SOP) of incident radiation for getting the sharpest notches in the reflection spectrum of the CFBG-FPI sensor. This adjustment is particularly useful in cases when CFBG-FPI is bonded to the structure directly using tapes or adhesives, since adhesive bonding introduces deformation of the sensor prior to GW detection. Radiation reflected from CFBF-FPI is channeled to the coupler C1, which splits

it in two parts. Most of the radiation power (≈ 95%) goes to the photodetector 1 (PD1), and a small portion of it (≈ 5%) is sent to the photodetector 2 (PD2). Radiation registered by PD1 is converted to voltage that is sampled by the data acquisition device (DAQ). Output of the PD2 is fed to a feedback control module of the TLS. The external TLS controller is designed to account

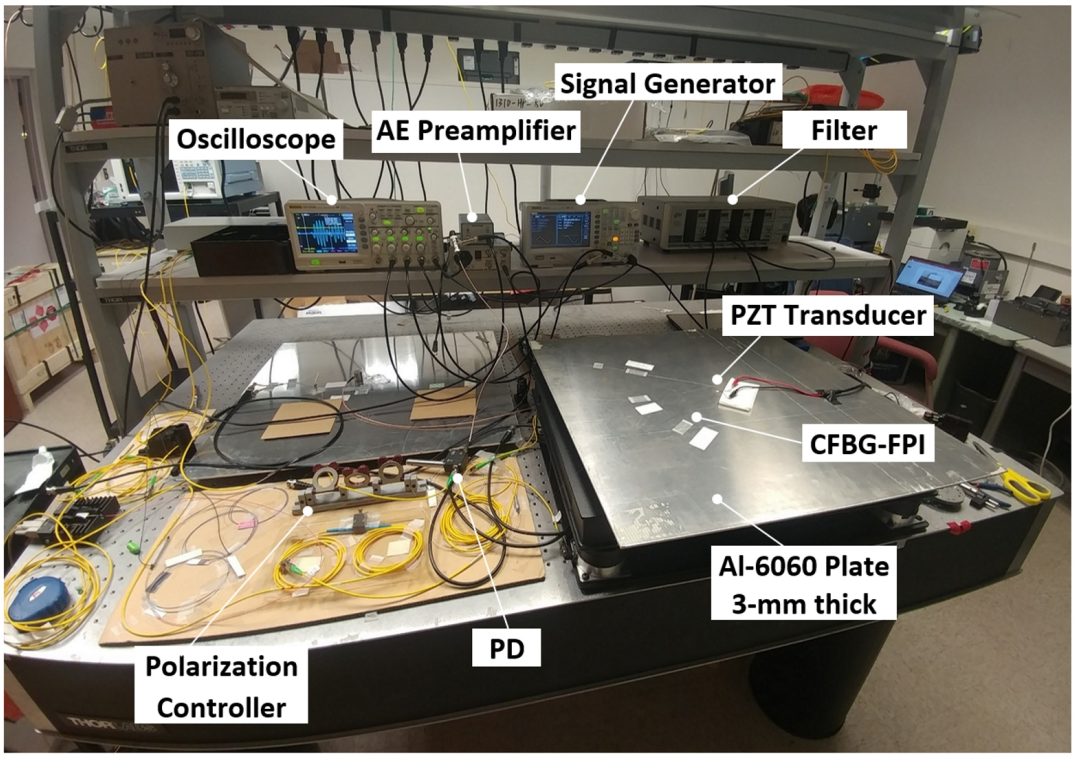

Figure 3.12: Experimental setup for GW detection using the CFBG-FPI sensors.

for quasi-static background strains caused by structural loads or ambient temperature drifts causing significant shifts of notches in the CFBG-FPI reflectance spectrum. Large background strains may push out the operating point well beyond the limits of TLS tuning range. However, if the bandwidth of TLS around the operating wavelength is wider than the FSR between the spectral fringes, other spectral notches will enter this window, and the controller will re-lock the TLS on the new notch. In this case, the sensitivity of the system to propagating GWs may change depending on the slope and amplitude of the new notch.

Experimental setup for GW detection in a 3-*mm* thick aluminum plate using the CFBG-FPIs is demonstrated in Fig. 3.12. Guided waves are excited in the plate with a 7-*mm* wide and 0.2-*mm*

thick round piezoelectric transducer made of PZT-5A material. The PZT crystal resonates at 300 kHz, and it is driven with a 5-cycle tone burst from DDS function generator. The amplitude of the excitation signal is 20 V_{pp}. Three 1545 nm CFBG-FPI sensors were fabricated in three separate

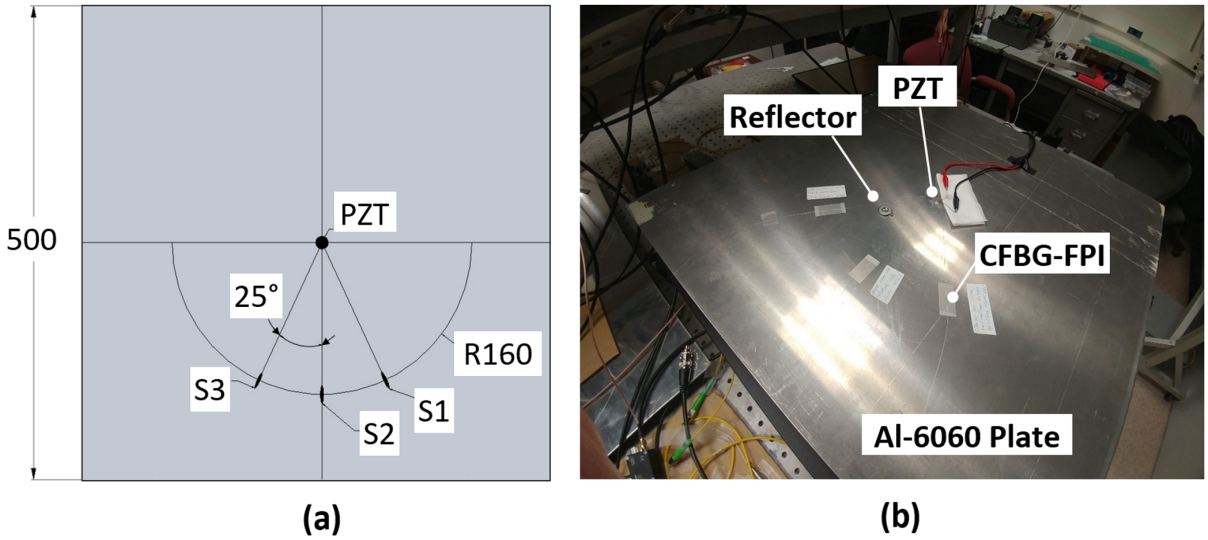

Figure 3.13: Aluminum plate with CFBG-FPI sensors, piezoelectric transducer and surface-bonded reflector: (a) drawing with exact dimensions; (b) photo of the test setup.

single-mode fibers using a 193 nm excimer laser and a linearly chirped phase mask with a chirp rate of 2 nm/cm. Each CFBG-FPI sensor was 1.1 cm long as it consisted of two 5-mm CFBGs separated by 1-mm gap. CFBG-FPIs were bonded to the surface of the plate directly using the Scotch tape in the locations shown in Fig. 3.13. Since the system was not wave division multiplexed (WDM), CFBG-FPI sensors were connected to the circulator via the APC connectors one-by-one to measure propagating GWs. Ultrasonic signals registered by the PD1 were amplified with a broadband 20-dB pre-amplifier from Physical Acoustics. Initially, three baseline GW signals were acquired by CFBG-FPI sensors, and after that an external reflector was bonded to the plate using the Krautkrammer acoustic gel as illustrated in Fig. 3.13(b). The measurement process was repeated in the presence of simulated damage. GW signals from CFBG-FPI sensor 3 are shown in Fig. 3.14. The signals represent two single measurements that were not averaged in time, but were only passed through a zero-phase band-pass filter with cut-off frequencies of 100 kHz and 500kHz. Actuation waveform shown in Fig. 3.14 is not filtered.

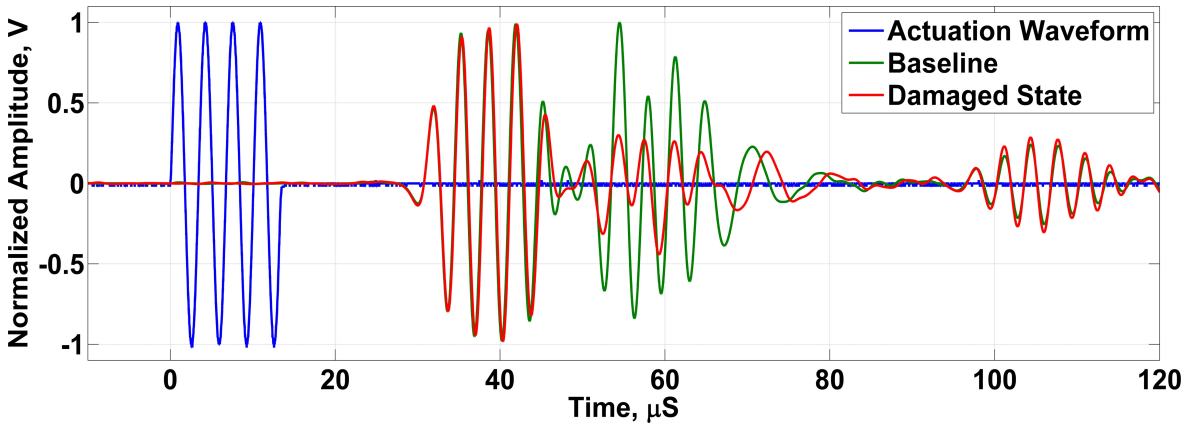

Figure 3.14: Guided waves registered with the CFBG-FPI sensor 3.

Obtained results demonstrate that two wave packets are clearly visible. The first wave packet with ToF around 38 μs corresponds to the fundamental S_0 mode, and the second wave packet with ToF of approximately 58 μs corresponds to the A_0 mode in the 3-mm thick plate. The group velocities of S_0 and A_0 modes agree well with the dispersion curves from Fig. 3.6. The S_0 wave packet resembles the excitation signal better than the A_0 wave packet, since the S_0 mode is less dispersive around 300 kHz. At the same time, the A_0 mode is more sensitive to a glued reflector.

3.4 Delay-and-Sum diagnostic imaging

In this chapter, the delay-and-sum (DAS) algorithm was used for data fusion from multiple guided wave paths [56]. The first step of the DAS imaging is computation of the wave scatter from damage. This task is accomplished by subtracting the baseline measurement from the measurement obtained after introduction of structural damage:

$$\hat{r}_{ij} = s_{ij}(t) - b_{ij}(t) \tag{3.30}$$

In Eq. (3.30), it is assumed that in a general case, the sensor system may have multiple GW transmitters and receivers. Hence, i denotes the index of the transmitting PZT; and j denotes the index of the receiving CFBG-FPI sensor; b_{ij} are the baseline signals, and s_{ij} are the GW signals in the damaged state of the structure.

The envelope of the residual signal due to damage is defined as

$$r_{ij} = |\hat{r}^a_{ij}| = |\hat{r}_{ij} + jH(\hat{r}_{ij})|, \tag{3.31}$$

where $\hat{r}^a_{ij}$ is the analytic signal, and $H(\hat{r}_{ij})$ is the Hilbert transform. In the next step, the energies of the computed residual signals are mapped onto each point on the image. The arrival time of the single mode wave packet traveling from the transmitting PZT at $(x_i; y_i)$ to the image pixel $(x; y)$ and on to the receiver at $(x_j; y_j)$ can be calculated as

$$t_{ij}(x, y) = \frac{\sqrt{(x_i - x)^2 + (y_i - y)^2} + \sqrt{(x_j - x)^2 + (y_j - y)^2}}{c_{gr}}, \tag{3.32}$$

where c_{gr} is the group velocity of the selected GW mode. Assuming there are P sensors in the array, and $M = \binom{P}{2} = \frac{P!}{2!(P-2)!}$ unique actuator-sensor pairs, envelopes of residuals computed in Eq. (3.31) are windowed using the corresponding time-delays $t_m(x; y)$ and are averaged over all pairs:

$$R(t; x, y) = \frac{1}{M} \sum_{m=1}^{M} r_m w\Big(t - t_m(x, y)\Big), \tag{3.33}$$

where $w(t)$ is a Gaussian window function, whose time support T is equal to the time support of the actuation signal. Finally, the intensity of the diagnostic DAS image at a pixel (x, y) is given by the energy of $R(t; x, y)$:

$$I(x, y) = \int_0^T \Big(R(t; x, y)\Big)^2 dt \tag{3.34}$$

Note that Eq. (3.34) defines a family of concentric ellipses around the actuator-sensor pair. Such approach is best suited for diagnostic imaging of structures with circular PZT elements that have uniform sensitivity to all directions of GW propagation. However, the algorithm will need to be modified in the future work to account for unidirectional sensitivity of CFBG-FPI along their length only.

Fig. 3.15 illustrates the DAS image of the plate with surface bonded reflector (see Fig. 3.13). The presence of reflector is better captured by the the CFBG-FPI-3 rather then CFBG-FPI-1 and CFBG-FPI-2. This happens because the scatter from damage propagates at angles to the sensors

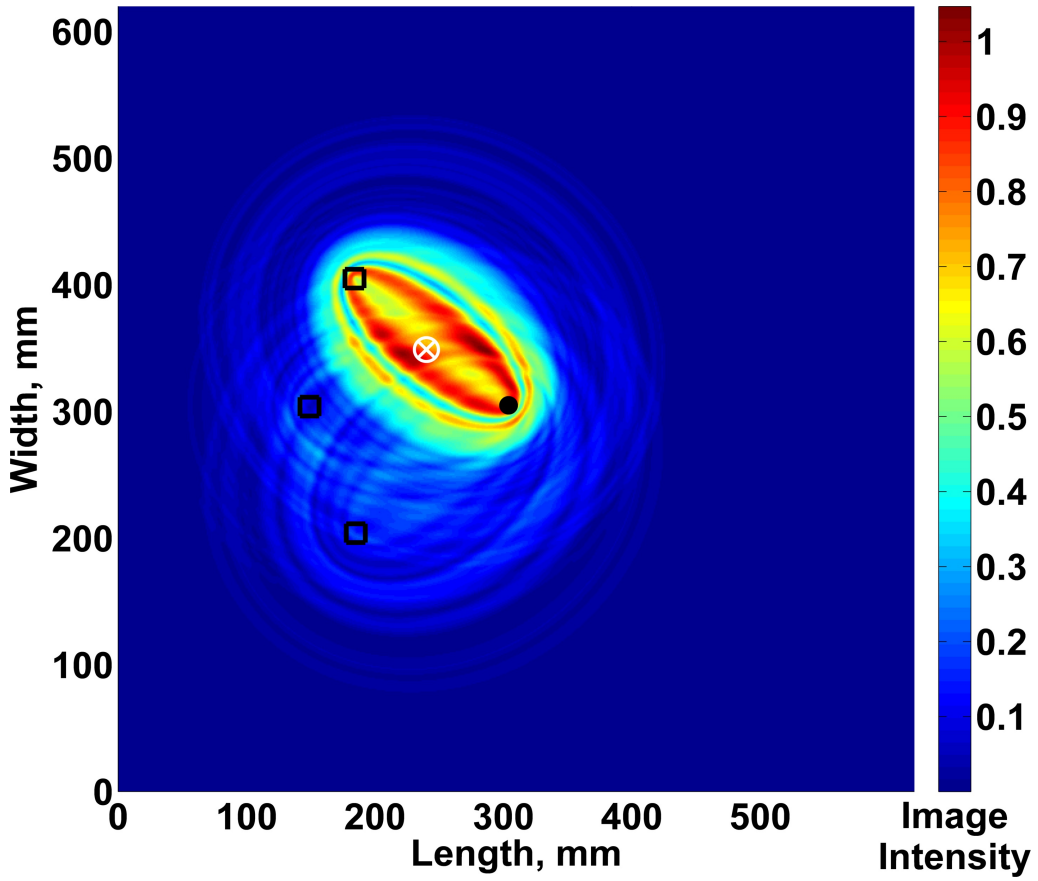

Figure 3.15: DAS image of aluminum plate with the surface-bonded reflector. Location of PZT actuator is marked as a black dot, CFBG-FPI sensors are marked as black squares, and location of damage is marked by a white circle with a cross.

1 and 2, and FBG-based fiber optic receivers provide the highest sensitivity to GWs along their length. Directional sensitivity of CFBG-FPIs should be incorporated into the DAS algorithm for more accurate damage localization. Another way to improve damage detection is to increase the number of pick-up sensors. It should be also noted that multiple CFBG-FPI sensors can be multiplexed in a single fiber using the WDM technique, and CFBG-FPI sensors may not be directly bonded to the structure. In general, it suffices to bond any open section of the optical fiber to the structure, and GWs will leak into it propagating to CFBG-FPI receivers through the fiber core and cladding.

3.5 Conclusions

Chapter III presented a hybrid approach for acousto-optic SHM of materials and structures. Online monitoring of structural health is accomplished by using surface-bonded or embedded arrays of optical fibers with strategic ability to sense ultrasonic guided waves. In this case, chirped Bragg-gratings inscribed in fiber core serve as receivers of ultrasonic signals. Pairs of CFBGs form Fabry-Perot cavities, whose spectra of back-reflected radiation have sharp transitions. Laser source is tuned to output radiation with a wavelength centered around these transitions. Hence, propagating UT waves shift the spectra of CFBG-FPI, which in turn results in modulation of radiation reflected by such optical sensor. In contrast to OFDR or local strain sensing using regular FBGs, hybrid GW/CFBG-FPI approach allows for detecting structural imperfections away from the fiber as guided wave reflections carry all necessary information instead. Proposed acousto-optic SHM technique was successfully validated on aluminum plates with damage simulated as surface-bonded reflector. Three CFBG-FPI sensors were used for receiving S_0 and A_0 GW modes generated by the piezoelectric transducer. Measurement in defect-free and damaged states were acquired by all CFBG-FPIs to generate a diagnostic image of the plate using the DAS algorithm. Since the damaged area was correctly highlighted, obtained results demonstrated the feasibility of the proposed hybrid GW/CFBG-FPI approach for SHM of metal and composite structures.

BIBLIOGRAPHY

BIBLIOGRAPHY

[1] E. Witten, T. Kraus, and K. M., "Composites market report," Tech. Rep., 2015. [Online]. Available: http://www.eucia.eu/userfiles/files/Composites-Market-20Report-2015.pdf

[2] M. Kreutzbruck, D. Brackrock, G. Brekow, H. Montag, R. Boehm, and B. Illerhaus, "Matrix phased arrays for the inspection of cfrp-components," in *Proceedings of 40th annual review of progress in quantitative nondestructive evaluation*, Baltimore, Maryland, USA, 2013, pp. 108–15.

[3] I. Amenabar, A. Mendikute, A. Lopez-Arraiza, M. Lizaranzu, and A. J., "Comparison and analysis of non-destructive testing techniques suitable for delamination inspection in wind turbine blades," *Composites Part B*, vol. 42, no. 5, pp. 1298–305, 2011.

[4] C. Scarponi and G. Briotti, "Ultrasonic technique for the evaluation of delaminations on cfrp, gfrp, kfrp composite materials," *Composites Part B*, vol. 31, no. 3, pp. 237–43, 2000.

[5] K. Berketis, D. Tzetzis, and H. Pj., "Impact damage detection and degradation monitoring of wet gfrp composites using noncontact ultrasonics," *Polymer Composites*, vol. 30, no. 8, pp. 1043–9, 2009.

[6] J. Dong, B. Kim, A. Locquet, P. McKeon, N. Declercq, and C. Ds., "Nondestructive evaluation of forced delamination in glass fiber-reinforced composites by terahertz and ultrasonic waves," *Composites Part B*, vol. 79, pp. 667–75, 2015.

[7] W. Harizi, S. Chaki, G. Bourse, and M. Ourak, "Mechanical damage characterization of glass fiber-reinforced polymer laminates by ultrasonic maps," *Composites Part B*, vol. 70, pp. 131–7, 2015.

[8] A. Hassen, H. Taheri, and V. U., "Non-destructive investigation of thermoplastic reinforced composites," *Composites Part B*, vol. 97, pp. 244–54, 2016.

[9] S. Kobayashi and T. N., "Experimental and analytical characterization of transverse cracking behavior in carbon/bismaleimide cross-ply laminates under mechanical fatigue loading," *Compoites Part B*, vol. 33, no. 6, pp. 471–8, 2002.

[10] C. Goidescu, H. Welemane, C. Garnier, M. Fazzini, R. Brault, and E. Peronnet, "Damage investigation in cfrp composites using full-field measurement techniques: combination of digital image stereo-correlation, infrared thermography and x-ray tomography," *Composites Part B*, vol. 48, pp. 95–105, 2013.

[11] M. F. Arif, F. Meraghni, Y. Chemisky, N. Despringre, and G. Robert, "In situ damage mechanisms investigation of pa66/gf30 composite: Effect of relative humidity," *Composites Part B*, vol. 58, pp. 487–95, 2014.

[12] J. P. Dunkers, D. P. Sanders, D. L. Hunston, M. J. Everett, and G. Wh., "Comparison of optical coherence tomography x-ray computed tomography, and confocal microscopy results from an impact damaged epoxy/e-glass composite," *Adhesives*, vol. 78, no. 2, pp. 129–54, 2002.

[13] C. Meola and C. Gm., "Recent advances in the use of infrared thermography," *Measurement Science and Technology*, vol. 15, no. 9, pp. 27–58, 2004.

[14] F. Libonati and L. Vergani, "Damage assessment of composite materials by means of thermographic analyses," *Composites Part B*, vol. 50, pp. 82–90, 2013.

[15] W. Harizi, S. Chaki, G. Bourse, and M. Ourak, "Mechanical damage assessment of glass fiber-reinforced polymer composites using passive infrared thermography," *Composites Part B*, vol. 59, pp. 74–9, 2014.

[16] S. K. Gayen and A. R., "Emerging optical biomedical imaging techniques," *Optics and Photonics News*, vol. 7, no. 3, pp. 16–22, 1996.

[17] I. Grulkowski, J. J. Liu, B. Potsaid, V. Jayaraman, J. Jiang, and J. G. Fujimoto, "High-precision, high-accuracy ultralong-range swept-source optical coherence tomography using vertical cavity surface emitting laser light source," *Optics Letters*, vol. 38, no. 5, pp. 673–5, 2013.

[18] S. V. Lomov, D. S. Ivanov, I. Verpoest, M. Zako, T. Kurashiki, and H. Nakai, "Full-field strain measurements for validation of meso-fe analysis of textile composites," *Composites Part A*, vol. 39, no. 8, pp. 1218–31, 2008.

[19] J. P. Dunkers, R. S. Parnas, C. G. Zimba, R. C. Peterson, K. M. Flynn, J. G. Fujimoto *et al.*, "Optical coherence tomography of glass reinforced polymer composites," *Composites Part A*, vol. 30, no. 2, pp. 139–45, 1999.

[20] J. P. Dunkers, F. R. Phelan, D. P. Sanders, M. J. Everett, W. H. Green, D. L. Hunston *et al.*, "The application of optical coherence tomography to problems in polymer matrix composites," *Optical Laser Engineering*, vol. 35, no. 3, pp. 145–7, 2001.

[21] K. Wiesauer, M. Pircher, E. Gotzinger, C. K. Hitzenberger, R. Oster, and D. Stifter, "Investigation of glassefibre reinforced polymers by polarisation-sensitive, ultra-high resolution optical coherence tomography: Internal structures, defects and stress," *Composites Science and Technology*, vol. 67, no. 15, pp. 3051–8, 2007.

[22] P. Liu, R. Groves, and R. Benedictus, "Non-destructive evaluation of delamination growth in glass fiber composites using optical coherence tomography," in *Procedings of SPIE*, vol. 9803. 9 pages: Article number 90631M, 2014.

[23] M. Choma, M. Sarunic, C. Yang, and I. J., "Sensitivity advantage of swept source and fourier domain optical coherence tomography," *Optics Express*, vol. 11, no. 18, pp. 2183–9, 2003.

[24] Z. Yaqoob, J. Wu, and C. Yang, "Spectral domain optical coherence tomography: a better oct imaging strategy," *Biotechniques*, vol. 39, no. 6, pp. S6–13, 2005.

[25] S. Farsiu, J. Christofferson, B. Eriksson, P. Milanfar, B. Friedlander, A. Shakouri *et al.*, "Statistical detection and imaging of objects hidden in turbid media using ballistic photons," *Applied Optics*, vol. 46, no. 23, pp. 5805–22, 2007.

[26] O. Karpenko, A. Khomenko, E. Koricho, M. Haq, and L. Udpa, "Monitoring of fatigue damage in composite lap-joints using guided waves and fbg sensors," in *Proc QNDE*, 2016.

[27] [Online]. Available: https://www.b2bcomposites.com/msds/appliedpoleramic/576520.pdf

[28] [Online]. Available: http://www.chemicalbook.com/ChemicalProductProperty_EN_CB3749115.htm

[29] [Online]. Available: http://www.ezentrumbilder.de/rg/pdf/td_en_GL1_GL2.pdf

[30] F. T. Wallenberger, J. C. Watson, and L. H. G. Fibers, *ASM handbook*, D. Miracle and S. Donaldson, Eds. Park, OH: ASM International, 2001, vol. 21, p.29-34. Composites. Materials.

[31] E. Koricho, A. Khomenko, and M. Haq, *Influence of nano-/microfillers on impact response of glass fiber-reinforced polymer composite*, Y. Dong, R. Umer, and A. Lau, Eds. New York: Woodhead Publishing, 2015, p.477-492. Fillers and reinforcements for advanced nanocomposites.

[32] J. D. Ingle Jr and S. R. Crouch, *Spectrochemical analysis*. New Jersey: Prentice Hall, 1988.

[33] M. Born and W. E., *Principles of optics*, 4th ed. New York: Pergamon Press Ltd, 1970.

[34] M. Polyanskiy, "Refractive index database." [Online]. Available: http://refractiveindex.info/

[35] K. E. Torrance and S. Em., "Theory for off-specular reflection from roughened surfaces," *Optical Society of America*, vol. 57, no. 9, pp. 1105–14, 1967.

[36] W. L., "Diffuse-reflectance model for smooth dielectric surfaces," *Optical Society of America*, vol. 11, no. 11, pp. 2956–68, 1994.

[37] A. Khomenko, O. Karpenko, E. Koricho, M. Haq, G. Cloud, and L. Udpa, "Optical transmission scanning for damage quantification in impacted gfrp composites," in *Proceedings of SPIE*, vol. 9804, 2016.

[38] "Matlab 2016a image processing toolbox user's guide." [Online]. Available: http://www.mathworks.com/help/pdf_doc/images/images_tb.pdf

[39] A. Khomenko, G. L. Cloud, and M. Haq, "Application of low-coherence interferometry for in situ nondestructive evaluation of thin and thick multilayered transparent composites," *Optical Engineering*, vol. 54, no. 12, 2015.

[40] P. Laugier, *Introduction to the physics of ultrasound*, P. Laugier and G. Haat, Eds. Netherlands: Springer, 2011, p. 29-45. Bone quantitative ultrasound.

[41] O. Karpenko, A. Khomenko, E. Koricho, M. Haq, G. L. Cloud, and L. Udpa, "Monitoring of impact damage accumulation in gfrp composites using guided waves and optical transmission scanning," P. of CAMX: The Composites and A. M. Expo, Eds., Anaheim, CA, USA, 2016.

[42] G. Dib, O. Karpenko, E. Koricho, A. Khomenko, M. Haq, and L. Udpa, "Ensembles of novelty detection classifiers for structural health monitoring using guided waves," *Smart Materials and Structures*, 2017.

[43] S. Yao, "Highly repeatable all-solid-state polarization-state generator," *Optics Letters*, vol. 30, no. 11, pp. 1324–1326, 2005.

[44] S. Yao, X. Chen, and L. Yan, "Self-calibrating binary polarization analyzer," *Optics Letters*, vol. 31, no. 13, pp. 1948–1950, 2006.

[45] S. Yao, X. Chen, and T. Liu, "High accuracy polarization measurements using binary polarization rotators," *Optics Letters*, vol. 18, no. 7, pp. 6667–6685, 2010.

[46] J. Lopez-Higuera, L. Cobo, A. Incera, and A. Cobo, "Fiber optic sensors in structural health monitoring," *Lightwave Technology*, vol. 29, no. 4, pp. 587–608, 2011.

[47] B. Lee, "Review of the present status of optical fiber sensors," *Optical Fiber Technology*, vol. 9, no. 2, 2003.

[48] A. Masoudi and T. Newson, "Distributed optical fibre dynamic strain sensing," *Review of Scientific Instruments*, vol. 87, no. 1, 2016.

[49] Y. Koyamada, M. Imahama, K. Kubota, and K. Hogari, "Fiber-optic distributed strain and temperature sensing with very high measurand resolution over long range using coherent otdr," *Lightwave Technology*, vol. 27, no. 9, 2009.

[50] S. Kreger, N. Rahim, N. Garg, S. Klute, D. Metrey, J. Jeans, and R. Gamber, "Optical frequency domain reflectometry: principles and applications in fiber optic sensing," in *SPIE Fiber Optic Sensors and Applications XIII*, vol. 9852, 2016.

[51] D. Coric, M. Lai, J. Botsis, A. Luo, and H. Limberger, "Distributed strain measurements using fiber bragg gratings in small-diameter optical fiber and low-coherence reflectometry," *Optical Society of America*, vol. 18, no. 25, 2010.

[52] J. Song, "Optical frequency domain reflectometry: sensing range extension and enhanced temperature sensitivity," Ph.D. dissertation, University of Ottawa, 2012.

[53] M. Froggatt and P. Moore, "Apparatus and method for measuring strain in optical fibers using rayleigh scatter," Patent, 2003, uS Patent 6,545,760 B1.

[54] Q. Zhang, Y. Zhu, X. Luo, G. Liu, and M. Han, "Acoustic emission sensor system using a chirped fiber bragg grating fabry perot interferometer and smart feedback control," *Optics Letters*, vol. 42, p. 3, 2017.

[55] V. Giurgiutiu, *Structural Health Monitoring with Piezoelectric Wafer Active Sensors*. Academic Press, 2008.

[56] J. Hall and J. Michiaels, “Minimum variance ultrasonic imaging applied to an in situ sparse guided wave array,” *IEEE Transactions on Ultrasonics Ferroelectrics and Frequency Control*, vol. 57, no. 10, 2010.